REINFORCEMENT OF NATURAL RUBBER USING NANOSTRUCTURED CARBON MATERIALS

Yang Shi

A thesis submitted for the degree of Master of Philosophy

School of Chemical Engineering

Faculty of Engineering, Computer and Mathematic Sciences

The University of Adelaide

May 2018

Contents

Abstract

As the earliest applied elastomer material, natural rubber has undergone development for nearly 100 years, and its performance has become a bottleneck. With the development of technology, industry increasingly needs higher performance natural rubber as a new generation of shock absorbing materials to improve the ride comfort of various vehicles, such as automobiles, trains, and aircraft.

The performance of natural rubber is mainly related to the fillers and filling amounts used. Even though traditional fillers such as carbon black and silica have been well studied, improving the performance of natural rubber composites is difficult.

This study used carbon nanomaterials as a new generation of fillers to prepare high-performance natural rubber composites. Since nanoparticles have strong van der Waals forces, carbon nanomaterials such as graphene and carbon nanotubes need to be modified before preparing the composite material so that they can be uniformly dispersed into the natural rubber matrix. This study used various modification methods, such as acidification, acyl chlorination, and ammoniation to modify the surface property of these carbon nanomaterials. After a variety of different polymers were grafted onto the nanomaterial surface, the modified carbon nanomaterials achieved good compatibility with the natural rubber matrix.

Subsequently, different fillers (carbon nanotubes, graphene, and carbon nanotubes & graphene) were mixed with natural rubber, and composites with different filling amounts were prepared by mechanical blending. The process, mechanical, fatigue and crack propagation properties of the natural rubber composites were investigated under dynamic and static conditions.

The results show that only a small filling amount is required and that carbon nanomaterials have better reinforcing effects than conventional fillers, revealing that as a new rubber filler, carbon nanomaterials have superior enhancement efficiency. As the filling amount increases, the mechanical strength of the natural rubber composite material is significantly improved. However, due to factors such as hysteresis loss and tearing energy, overfilling may cause a decrease in the fatigue resistance of natural rubber composites. The experimental results show that when the loading mass ratio of carbon nanotubes to rubber is 1:3, the overall performance of the natural rubber composites is optimized. For graphene, when the loading mass ratio is 1:1, the overall

performance of the natural rubber composite material is optimal. This study also shows that carbon nanotubes and graphene have synergistic effects when they are simultaneously used as fillers to prepare natural rubber composites.

Declaration

I certify that this work contains no material which has been accepted for the award of any other degree or diploma in my name in any university or other tertiary institution and, to the best of my knowledge and belief, contains no material previously published or written by another person, except where due reference has been made in the text. In addition, I certify that no part of this work will, in the future, be used in a submission in my name for any other degree or diploma in any university or other tertiary institution without the prior approval of the University of Adelaide and where applicable, any partner institution responsible for the joint award of this degree.

I give permission for the digital version of my thesis to be made available on the web, via the University's digital research repository, the Library Search and also through web search engines, unless permission has been granted by the University to restrict access for a period of time.

Name of Candidate: Yang Shi

Signature:

Date:

Acknowledgments

First and foremost, I would like to express my sincere gratitude to my principal supervisor group, Prof. Shi-Zhang Qiao and Prof. Zhengtao Su. for their invaluable guidance, strong support, and continuous encouragement during my study. their suggestions not only motivate me in scientific research but also enlighten me in life. Also, I am grateful to my co-supervisor Dr. Yao Zheng who instructs me in research.

I also want to extend my appreciation to all the group members from Prof. Qiao's group in the University of Adelaide for their technical assistance and helpful discussion. They are Dr. Yao Zheng, Dr. Bo You, Dr. Lei Zhang, Dr. Yan Jiao, Mr. Dongdong Zhu.

I would also like to acknowledge the AECC Beijing Institute of Aeronautical Materials and the University of Adelaide, which offered me the scholarship to pursue my master degree and live in Adelaide. Also, many thanks to the Australian Research Council Linkage project, which has financially supported my research.

Special thanks to my best friend in Adelaide, they are Mr. Fangxi Xie, Mr. Huanyu Jin and Mr. Yong-Qiang Zhao, who give me great help for my thesis.

Finally, I want to express my great gratitude to my parents, my wife and my sons for their endless love and encouragement in my life.

Index of Figures

Index of Tables

List of Abbreviations

NR	Nature rubber
CNTs	Carbon Nanotubes
MWCNTs	Multi-walled carbon nanotubes
SWCNTs	Single-walled carbon nanotubes
GO	Graphene oxide
rGO	Reduced graphene oxide
GE	Graphene
CB	Carbon black
EPDM	Ethylene Propylene Diene Monomer
PS	Polystyrene
PP	Polypropylene
HNBR	Hydrogenated nitrile butadiene rubber
SDS	Sodium dodecyl sulfate
SDBS	Sodium dodecyl benzene sulphonate
XPS	X-ray photoelectron spectroscopy
DMF	Dimethylformamide
THF	Tetrahydrofuran
DCM	Dichloromethane
TEA	Triethylamine
PMDETA	Pentamethyldiethylenetriamine
SEBS	Styrene ethylene butylene styrene
TMSCL	Trimethylchlorosilane
ZDC	Zinc dimethyldithiocarbamate
MWCNTs-0	Pristine MWCNTs

Modified-MWCNTs-1	Acidified MWCNTs
Modified-MWCNTs-2	Acid chloride MWCNTs
Modified-MWCNTs-3	Aminated MWCNTs
Modified-GO-1	Alkyne-containing GO
SEBS-GO	SEBS modified GO
N-PS	Azido modified monodisperse polystyrene
N-SEBS	Azido modified SEBS
PS-GO	PS modified GO
NH_2-GO	Tail-end chlorine-containing GO
HED	Hysteresis energy density
PP-GO	PP modified GO
SNTS	Single-notched tensile specimens
TGA	Thermogravimetric analysis
SEM	Scanning electronic microscopy
DSC	Differential scanning calorimetry
XRD	X-ray power diffraction
GPC	Gel permeation chromatography
RPA	Rubber Processing Analysis
DMTA	Dynamic mechanical thermal analyzer
PSS	Pure shear specimen
CTOD	Crack tip open displacement
ATRP	Atom-transfer radical-polymerization
DTG	Derivative thermogravimetric analysis
SED	Strain energy density
ODA	Octadecylamine
MAPP	Maleic anhydride grafted polypropylene

Chapter 1. Introduction

1.1. Background

1.1.1. Developments of the rubber industry

Natural rubber (NR) is a polymer consisting of isoprene units linked together at the 1-4 positions and arranged in a cis configuration [1]. Among the many types of engineered polymers, NR is one of the most fascinating and important industrial polymers. NR is widely used in modern society because of its high elasticity, low conductivity, plasticity and other superior characteristics under dynamic conditions (Figure 1-1). It contributes a large variety of antivibration products to the automotive, aerospace, and constructing fields, which clearly have a wide range of products and downstream industries. However, NR materials hardly show any value without reinforcement because of their inferior mechanical strength and elasticity as well as their short lifetime. Therefore, rubber for commercial uses requires different reinforcing fillers, antioxidants and related additives to achieve a high value after processing [2].

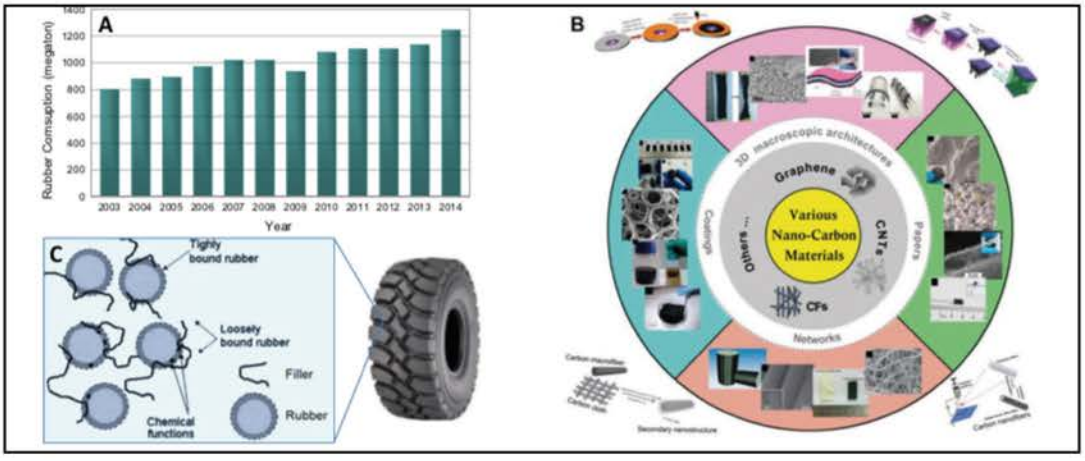

Figure 1-1 (A) Consumption of natural rubber (NR). (B) Carbon nanomaterials in different fields. (C) Fillers in rubber products.

1.1.2. Filling materials for rubber reinforcement

Filler distribution affects the properties of the rubber, as the distribution controls the molecular weight and dispersion of the NR in each phase and the chemical interaction between the rubber matrix and fillers [3]. Fillers can be differentiated from each other based on several parameters, such as color, source, and activity. Fillers, therefore, can be natural or synthetic and reinforcing or inert. Currently, many types of fillers are used

in rubber formulation mainly to achieve the desired physical properties and processing performance [4]. For instance, titanium dioxide (TiO_2) is widely used as a rubber filler because of its self-cleaning surface, which can decompose organic contaminants and/or kill bacteria adhering to the surface, and its high surface-to-volume ratio and consequent high surface activity, which makes it suitable as a reinforcing filler for rubber after surface activation [5]. Clay is the most widely used nonblack filler for rubber. Its use is based on its comparatively low cost, versatility and stiffening properties. Typical uses of treated clays include as an inner liner for tires, where they reduce air permeability, and white sidewalls. However, local overheating usually happens in TiO_2- and clay-reinforced NR composites, considerably impairing their safety during usage. Silicone-filled rubber is one of the most widely used elastomers in rehabilitation devices and biomedical implants because it has excellent mechanical properties and relatively good biocompatibility. However, it is prone to biofouling, which is a major cause of patient discomfort and even clinical failure in many applications [6]. Numerous antibacterial treatments of silicone-reinforced rubber have been utilized, but none have been proven to be completely effective [7]. Therefore, new types of effective fillers are urgently required to enhance the performance of rubber materials.

1.1.3. Nanostructured carbon

The remarkable structure-dependent carbon nanomaterials have attracted much attention over the last decade due to their potential applications in different fields, such as molecular electronics, catalysts, supports, and sensors [1]. Because of the advantages of carbon nanomaterials, especially their large specific surface area, high aspect ratio, high thermal conductivity and strong mechanical durability, the crosslinking between the carbon filler and rubber can be significantly enhanced [8]. This combination of properties results not only in substantially enhanced mechanical properties but also in a greatly improved loss angle, which consequently enhances the damping properties of the rubber composites [9-11]. In the traditional blending system, an increase in the damping properties can lead to overheating in the interior of the raw materials, which damages the rubber products. In contrast, as a new type of rubber filler with excellent thermal conductivity, carbon nanomaterials keep rubber products cool throughout the entire processing procedure, which creates a great opportunity for fabricating rubber products with long lifetimes [11]. Nanostructured carbon-reinforced rubber composites

with longer lifetimes and better performance than those obtained from the conventional NR blending system can be achieved by adjusting their physicochemical structures [12]. Using carbon nanomaterials as the reinforcing fillers to prepare rubber-based composites is an important strategy to improve the lifetime, mechanical properties, wear resistance, damping properties, heat insulation, etc., of NR [12-14]. However, carbon nanomaterials have strong π-π bonding interactions and a high specific surface area, which may lead to their easy agglomeration when used as the rubber fillers during actual production [3, 4].

1.2. Aim and objectives

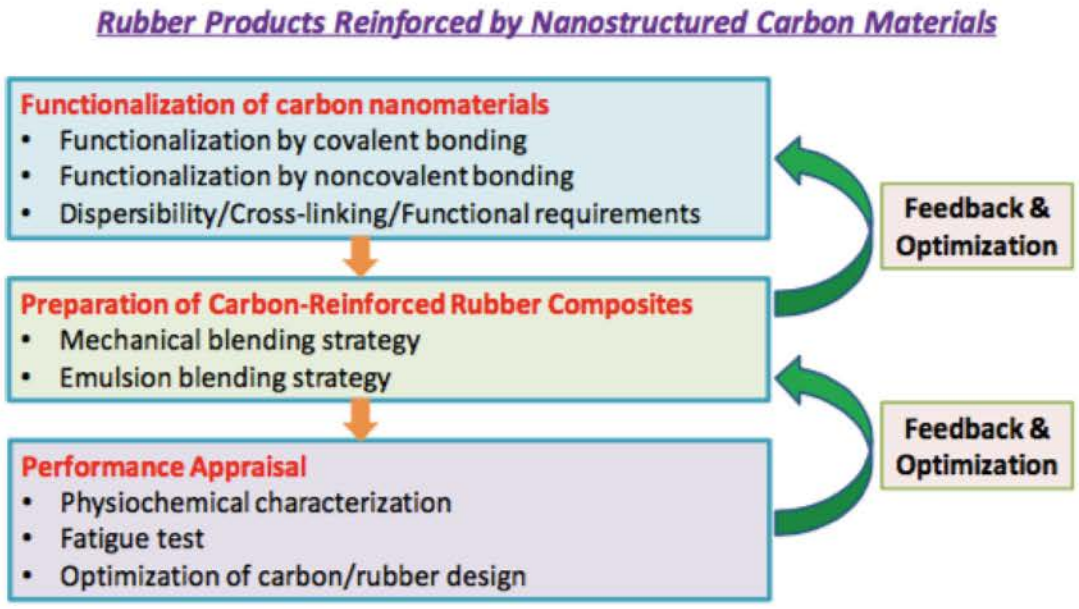

Figure 1-2 Framework of the project

The overall aim of this thesis is to develop long-lifetime carbon-reinforced rubber composite materials by evenly dispersing nanostructured carbons into a rubber matrix, followed by strong crosslinking between the two components (Figure 1-2). The interaction between NR and carbon nanomaterials as well as its impact on the physicochemical properties of rubber composite materials will be investigated in depth to enhance the performance of new rubber products. More specifically, the aims of this thesis are as follows:

① Developing innovative synthetic strategies that can provide functionalized carbon nanomaterials with controllable morphologies and functional groups;

② Combining carbon nanomaterials and NR by mechanical and emulsion blending

techniques to fabricate highly crosslinked composites;

③ Characterizing the physicochemical properties and evaluating the performance of the synthesized rubber composites, including their flexibility, thermal conductivity, loss angle, oil resistance, and lifetime;

④ Investigating the impact of carbon/rubber interactions and blending technologies on rubber performance to propose a discovery scheme for high-performance rubber products.

1.3. Thesis outline

1.3.1. Significance

This research aims at developing innovative synthetic and blending strategies for carbon nanomaterials to reinforce rubber composites. The proposed research directly addresses an important problem in the rubber industry, i.e., meeting the urgent need for high-performance reinforced rubber products with a long lifetime, high thermal conductivity, high loss angle, high oil resistance and high dynamic performance. As the application of nanostructured carbons as fillers in reinforced rubber has been scarcely investigated, the successful completion of this research will generate various innovative techniques for the functionalization of NR.

Moreover, the nanostructured carbon-reinforced rubber composites developed through this research can help downstream of the rubber products industry by finding new profit growth points. For example, new materials can be used in the transportation industry, which needs long-lifetime truck tires; in the aerospace industry, which urgently needs strongly antivibration rubber; and in aircraft sealant systems, which require rubber with high obstructing performance over a wide range of temperature (e.g., 60°C~350°C).

1.3.2. Innovation

When combined with the new filler materials, modified NR has obvious advantages over traditional rubber-related products because of the large specific surface area, high aspect ratio, high thermal conductivity and high mechanical durability of nanostructured carbon. The specific innovations are as follows:

① Innovative functionalization strategies for preparing carbon nanomaterials with controlled shape, size, and surface organic functionalities;

② Innovative mechanical/emulsion blending methods that can homogeneously and closely blend carbon nanomaterials with NR materials;

③ The high flexibility, surface area, and aspect ratio of carbon nanomaterials can considerably increase the number of physiochemical crosslinking points and entanglement points, consequently improving the crosslink density and enhancing the mechanical stability of the resident rubber;

④ Nanostructured carbon materials can facilitate the strain-induced crystallization process of rubber composites, which is the most important factor in enhancing the mechanical properties of NR composites;

⑤ Carbon nanomaterials have excellent thermal conductivity, and evenly dispersed carbon nanomaterials spread heat quickly in a rubber matrix without causing local overheating, which is the main reason for rubber damage. Therefore, nanostructured carbon fillers can significantly improve the lifetime of rubber materials.

1.3.3. Outline

The use of modified carbon nanomaterials to reinforce natural rubber matrix is highly feasible and can afford high-performance reinforced NR composite materials. The new carbon-reinforced rubber products will substantially outperform existing rubber materials in terms of their lifetime, mechanical strength, damping properties, thermal conductivity and many other aspects. The following is the thesis outline:

① Preparation of carbon nanomaterials with controllable morphology

② Preparation of surface-functionalized carbon nanomaterials

③ Preparation of nanocarbon-reinforced rubber composite materials

④ Performance evaluation of carbon-reinforced rubber composites

Chapter 2. Literature Review

2.1. Introduction

Carbon is the framework of all organic matter and life in nature, and it plays a decisive role in the development and formulation of life. With the advancement of science and technology, a series of new carbon materials are emerging, such as carbon quantum dots (Carbon Quantum), zero-dimensional fullerene (C60), one-dimensional carbon nanotubes (CNTs) and and two-dimensional graphene, the discovery of which has led to the development of the materials field, thereby initiating a continuing research boom [15, 16].

The many combinations of carbon, the sixth element in the periodic table, form the basis of all of organic chemistry and thus sustain the multiplication of life. In nature, there is a very large amount of naturally formed carbon such as graphite or coal, as well as a small amount of diamond [17]. In the second half of the 20th century, various new allotropes of carbon were discovered and applied in the forefront of technological development. In the field of nanocomposites, these carbon nanostructured materials, especially CNTs, have been widely used in reinforcing fillers of polymer-based composites for several decades, and some good results have been obtained [4, 18-20]. However, due to their high cost (for example, single-walled carbon nanotubes), high viscosity and anisotropy caused by the "nesting" structure, CNTs have not been a great filler for polymer reinforcement. Graphene is a nanostructured carbon allotrope with a two-dimensional honeycomb lattice structure formed by sp^2-hybridized carbon atoms. In fact, Wallace et al. first used graphene for theoretical calculations in solid-state physics in 1947 and the results have been widely used to characterize other carbon-based materials. However, it is difficult for graphene to exist independently due to the thermodynamic instability of its quasi-two-dimensional structure. Nevertheless, in 2004, Geim and Novoselov successfully prepared monatomic-thickness graphene by directly stripping graphite, a discovery for which they won the 2010 Nobel Prize in Physics [21]. Due to its unique electrical, optical, mechanical and thermal properties, graphene has drawn much attention from researchers around the world. Among the applications of graphene, its use as a nanofiller to prepare functional and structural nanocomposites is an important part of composite materials research [22].

Rubber is a material that has unique physical and mechanical properties at room

temperature and has large elastic strain, low elastic modulus, and excellent strain recoverability. As an important and irreplaceable strategic resource, rubber has been widely used in various fields, such as tires, conveyor belts, seals, and shock absorbers. In recent years, the increasing demand for advanced technology in these fields has made the fabrication of functional, refined and diversified rubber the future research direction.

Natural rubber has no practical value before appropriate filler reinforcement. Carbon black (CB) is the earliest and most commonly used carbon-based filler in the rubber industry [23, 24]. However, as this field has developed, CB has failed to meet the multifunctional needs of rubber products. The advent of new carbon materials has thus opened up a whole new field of rubber material functionalization and diversification. Compared with CB, CNTs and graphene can endow rubber materials with excellent physical and mechanical properties, electrical and thermal conductivity, and gas/liquid barrier properties [25-27]. Therefore, the use of new carbon-based fillers is one of the development trends in the rubber industry.

Since the 1990s, the nanotechnology boom has opened the door to a new chapter in materials science, offering superior mechanical, thermal, optical and electrical properties compared to those of conventional single-polymer materials. Nanomaterials are classified into zero-dimensional, one-dimensional and two-dimensional materials according to the different constraints on their spatial dimensions [28]. Nanomaterials of different dimensions have anisotropy in the direction of load transmission. Polymer nanocomposites can be divided into structured nanocomposites and functional nanocomposites according to their purpose [29]. For structured nanocomposites, the addition of inorganic nanofiller can effectively improve their composite durability, flammability, barrier properties and processing properties [30-32]. To achieve a good dispersion effect of a nanofiller in a polymer matrix, it is necessary to modify the nanoparticles and improve the preparation process of the material. For functional nanocomposites, their electrical, magnetic, optical and other properties depend mainly on the nature of the added nanoparticles [33-35].

Rubber products, such as tires, generally fail under dynamic conditions, while shock absorbers, such as those in automobiles and high-speed railways, generally fail under static conditions. Rubber products such as automobile tires strongly affect the safety of human lives and property. Cracks, which generate rubber damage, are mainly caused by the conversion of the kinetic energy in the rubber products into heat that

cannot flow out effectively. Therefore, utilizing the excellent thermal conductivity of carbon nanomaterials to improve the thermal conductivity of rubber composites is very important. Therefore, research on the crack propagation resistance and thermal conductivity of rubber materials has very important practical significance. In basic research on carbon-based filler/rubber composites, we also focused on the influence of different carbon nanomaterials on the fatigue properties of rubber composites.

2.2. History of graphene

Recently, graphene, as a well-known material in the field of condensed matter physics and materials science, has been an area of great interest to researchers in the fields of physics, chemistry and materials [15, 21, 36]. However, graphene is not a new concept in the field of theoretical research; in fact, graphene had been the subject of theoretical research for 60 years before it was successfully isolated. Its existence has broken the previously universal rule that any two-dimensional crystal will not exist stably at a certain temperature, and has stimulated many new theoretical and experimental studies. Its unique structure and properties have also brought about an era of monatomic-thickness materials to not only discover new phenomena in low-dimensional physics but also realize practical applications [37-39]. Scientists believe that graphene is a rare and radical change in the field of materials science and will be widely used in supercomputers, flexible touch screens, environmental and medical equipment, photon sensors and organic solar cells, among many other fields [3, 18, 40].

2.2.1. Structure of graphene

Graphene is a single layer of carbon atoms in a two-dimensional honeycomb lattice structure [21]. Structurally, graphene is an essential part of other graphite-type carbon materials. It can form zero-dimensional fullerenes, two-dimensional CNTs, and three-dimensional graphite. The performance of various carbonaceous materials, including graphite, has been studied for approximately 60 years. It had long been thought that graphene can exist only in theory because such a curved structure is generally considered thermodynamically unstable. However, in 2004, Nozerov et al. discovered monolayer graphene materials in their experiments. Since then, researchers have realized the amazing physical properties of graphene, such as its high rigidity, high strength, high electrical conductivity and high thermal conductivity [41, 42]. Therefore, the scope of research on graphene as a material has been greatly expanded. In particular,

due to the high charge mobility of graphene, current graphene-related research is mainly concentrated in the field of electronic equipment [43, 44].

Due to the high electron conductivity of graphene, graphene has a very high intrinsic mobility and zero effective mass and can propagate micron distances without scattering at room temperature. Therefore, most of the original research on graphene has focused on its electronic properties and applications in electronic devices.

However, the application of graphene in nanocomposites is also an important research direction. For decades, the academic community has conducted many fruitful and in-depth studies on composites. Recently, due to the attractive properties of graphene, many researchers working on other nanocomposites have shifted their focus to graphene [45-48]. For example, nano-montmorillonite composites, graphite composites, and other common composite materials have encountered a performance bottleneck. There have been no breakthroughs in related research for many years. Under these circumstances, new composites using graphene as a reinforcing filler have better application prospects and are considered the next generation of high-performance composite materials.

The family of carbonaceous materials used as polymer fillers, such as CB, has a history of more than 100 years and has been widely studied and applied in recent decades. In recent years, fillers such as thin layers of graphite treated by microwave, spheroidization or sonication have greatly improved the mechanical and electrical properties of polymers [49-51]. Since thin graphite is defined as a 100 nm-thick carbon material comprising single-layer graphene, the appearance of single-layer graphene has attracted much academic attention with regard to the next generation of nanocomposites [29, 52, 53].

2.2.2. Properties and applications of graphene

Due to its unexpected mechanical properties, graphene has attracted widespread attention in industry. The Young's modulus of nanoscale graphene sheets is 1 TPa, and the intrinsic strength reaches 130 GPa. The related test results have drawn extensive attention [15, 36]. These excellent properties make graphene one of the hardest, most robust materials found so far by humans. Its excellent mechanical properties make graphene a great reinforcing filler for creating new composite materials for the rubber industry and rubber applications [39, 42].

One of the reasons for the rapid progress made in graphene research is that obtaining high-quality graphene materials in the laboratory is relatively easy and cheap. In addition, many features of graphene were found in experimental measurements to reach the limits of theoretical predictions, such as its extremely high room-temperature electron mobility, Young's modulus of 1 TPa, intrinsic strength of 130GPa, very high thermal conductivity [41], great light absorption properties, complete impermeability to any gas, and ability to withstand extremely high current (one million times higher than copper) [54]. The surface structure of graphene makes it very easy to functionalize, which has led to the expectation that graphene materials will find various uses in further applications [48, 55]. We expect that a wide variety of functional groups can be introduce to the graphene surface to achieve the desired properties [56-59].

Additionally, many of the superior properties of graphene justify its nickname of the "miracle material." However, some of these properties are found only in the highest quality samples, including graphene samples prepared by mechanical lift-off or those deposited on a special substrate such as hexagonal boron nitride. The relevant performance measures can only be reproduced with graphene prepared by the above methods. In addition, although the preparation methods of graphene are rapidly improving, the extreme properties mentioned above cannot been observed in samples prepared by other techniques. Therefore, graphene will be more interesting for industrial applications if these techniques can be realized on an industrial scale. This objective is also one of the future directions in this field.

2.3. History of carbon nanotubes

The discovery of CNTs was a milestone in the development of nanomaterials. In 1991, Professor Iijima, an electron microscopy specialist, discovered multiwalled carbon nanotubes (MWCNTs) in the arc-evaporated graphite cathodes; today, the boom in the area of research boom continues [60, 61]. CNTs, with their unique structure and excellent mechanical, electrical and thermal properties, have been comprehensively studied by researchers [62-64]. In many years of research on CNTs, there have been countless achievements, which bring us confidence in their application prospects. Regarding the current and future commercial applications of CNTs, their synthesis, assembly and main applications have already been carefully described [32]. In commercial applications in, for example, the energy storage, environmental and biotechnology fields, CNTs have already shown their unique advantages over other

nanomaterials.

2.3.1. Structure of carbon nanotubes

CNTs have a seamless tubular structure formed by curling a single or multiple layers of graphite in a certain vector direction. This closed framework gives carbon nanotubes many excellent properties. First, the C-C bond is one of the strongest chemical bonds in nature, which endows CNTs with very high axial strength, toughness, and elastic modulus, as well as a tensile strength of up to 200 GPa, 100 times greater than that of steel. Compared with conventional carbon fibers, CNTs with an aspect ratio of 1000:1 are the ideal fiber materials and thus are known as "super fibers" [65, 66].

CNTs are a graphite tubular crystal with carbon atoms connected by covalent bonds and have one-dimensional structural characteristics. CNTs can be divided into single-walled carbon nanotubes (SWCNTs) and MWCNTs, which are usually composed of several to several tens of SWCNTs. The radial size of CNTs is on the nanometer scale, the length is on the order of microns, and the aspect ratio is 100-1000 [64].

CNTs can be divided into three types according to the helical vector and the helix angle: armchair, zigzag and chiral. The diameter, helix angle, and chirality of a CNT determine its electrical conductivity [67]. In addition, structural defects in CNTs can change their electrical properties. Due to the large aspect ratio and good flexibility of CNTs, prepared CNTs are easily bent and damaged. Moreover, many CNTs have film-like, filamentous or woody-like macroscopic structures, which lead to their divergent respective performances but also make them more convenient for direct manipulation, cropping or compounding [68, 69]. As an important one-dimensional nanomaterial, CNTs have many excellent properties, endowing them with good application prospects and status in many fields. For example, CNTs have been used in fuel cells, lithium batteries, composite materials, chemical and biological separation, purification, catalysis [70], probes, sensors, brakes, transistors, and field emission devices [71, 72]. CNTs with strong C-C bonds between carbon atoms are presumed to have very high axial strength and elastic modulus and have high uniformity.

2.3.2. Properties and applications of carbon nanotubes

The C-C covalent bonds in CNTs are very stable in nature. Studies have shown that the Young's modulus of CNTs is 14.2 GPa and that their tensile strength is approximately

200 GPa (100 times higher than that of steel). However, their density is much lower than that of steel (only 1/6~1/7). Furthermore, the axial elongation of CNTs reaches 20%. As a result, CNTs can be used as an ideal reinforcing filler to improve the mechanical properties of polymer composites [16, 71]. CNTs have excellent electrical properties: Metallic SWCNTs can withstand current densities up to 1 GA/cm^2, and CNTs are ballistic conductors [73]. They do not generate heat when a large current is passed through them and are excellent materials for electronic devices [70]. The thermal stability of CNTs is very high. Near the temperature of 700°C, there are almost no structural changes in air, the thermal expansion coefficient is very small, and the axial thermal conductivity is as high as 6600 W/(m*K). At room temperature, CNTs are also capable of absorbing light of narrower wavelength and then emitting light with a new wavelength. Additionally, since CNTs have nanosized inner diameters, they can be used in nanowires, molecular-level catalysts, fuel cells, etc., by filling them with other substances. Great breakthroughs have also been made in the fields of emission and hydrogen storage applications.

CNTs also have unique optical properties [74]. Both theoretical calculations and experimental results show that CNTs have a photoluminescence effect, that is, a luminescence phenomenon, which is a nonlinear optical property, that occurs under laser irradiation [75, 76]. Because of this feature, CNTs have potential applications in light emitters, optoelectronic devices, and polarized infrared light detectors. The electroluminescence effect of CNTs gives them extensive applications in other vacuum nanoelectronic devices, such as flat-panel displays.

The electrical properties of CNTs are extremely variable. The conductivity of the intrinsic perfect structure of SWCNTs is between that of a conductor and that of a semiconductor. Specifically, approximately 1/3 of SWCNTs are conductive, whereas 2/3 are semiconducting. The carrying capacity of SWCNTs is 1000 times higher than that of copper wire. The average specific resistance of SWCNT filament bundles at room temperature is 0.6 mΩ/cm, which is about six times higher than that of a single filament [77]. CNTs prepared in the laboratory have different conductivities due to their various structural changes and defects. MWCNTs and their arrays or films have good electrical conductivity. However, due to their structural complexity, there is no uniform behavior between that of a metal and that of a semiconductor. The good electrical conductivity of CNTs have led to their widespread use in the field of batteries,

capacitors, and solar cells [78].

According to statistics, the global output of CNTs is approximately 2,500 tons, and the turnover reaches billions of dollars. Most of this value arises from MWCNT-based products. Thus, the applications of CNTs have been transformed into direct economic benefits. In total, 69% of CNTs are used in plastics and composites; the rest are used in the electronics and energy industries (areas in which their usage is expected to rapidly increase further as new energy materials are developed) [79]. From the above data, it is clear that the current applications of CNTs no longer depend on only one property but a combination of their multiple excellent properties, allowing the complete utilization of their performance in many fields. For example, in electrochemical capacitors (supercapacitors), the large surface area, good conductivity, and good mechanical properties of CNTs are considered to help maintain their stable structure, chemical stability and high power density. Another example is the use of CNTs in fuel cell applications, where their stable and orderly structure, stable chemical properties and good conductivity provide an excellent platform for catalyst supports. Another trend is to take full advantage of the structural properties of CNTs in combination with other materials to compensate for or complement each other [80]. Currently, carbon nanotubes and their composites are widely used in flexible transistors, memory devices, the environment (for example, sewage purification and exhaust gas adsorption) and new energy sources such as lithium batteries, fuel cells, solar cells and supercapacitors [9, 16, 25, 70].

2.4. Rubber composites

2.4.1. Graphene/rubber composites

Graphene is a carbonaceous material in which carbon atoms are closely packed into a single-layer two-dimensional honeycomb lattice structure, and it can be regarded as the building block for other dimensional carbonaceous materials (such as zero-dimensional fullerene, one-dimensional carbon nanotube, and three-dimensional graphite) [27]. Recently, graphene has shown great scientific significance and application value both theoretically and experimentally and has shown unique application advantages in biology, electrode materials, sensors, etc. [3, 15, 36]. With increasing research on graphene, some of its intrinsic properties, such as fluorescence properties and template properties, have also been found. Graphene-reinforced composites have better physical

properties than traditional composites due to their large specific surface area, aspect ratio, thermal conductivity and electrical conductivity [81]. Graphene oxide (GO) has a large specific surface area and abundant surface functional groups, endowing it with excellent composite properties. After modification and reduction, a nanoscale dispersion of graphene is formed in a polymer matrix. Graphene can change the mechanical properties, barrier properties and thermal stability of the polymer matrix. [8, 82, 83]. In recent years, many graphene/polymer composite patents in applications such as fuel cells, the synthetic chemical industry, microporous catalyst carriers, conductive plastic, conductive coatings and fire-resistant materials for the construction industry have been reported [84-87]. The applications of graphene for the preparation of lightweight, low-cost and high-performance multifunctional nanofiller/polymer composite materials provide new methods and opportunities for the development of high-performance rubber.

Because of its excellent electrical conductivity, thermal conductivity, and mechanical properties, graphene can function as a great reinforcing filler for the preparation of composite materials. Furthermore, when graphene is dispersed in solution, it can also polymerize with a monomer to form a composite material. The addition of graphene can endow composites with different functionalities, providing them with not only excellent mechanical and electrical properties but also excellent processability, and thus expanding the application scope for nanocarbon composite materials [88-91].

Compared with those of the pure polymer, the mechanical, thermal, electrical and flame-retardant properties of graphene/polymer composites are significantly improved [92-95]; these properties are even superior to those of clay-based or other carbon-reinforced polymer-based composites [96, 97]. Although the mechanical properties of carbon nanotubes are comparable to those of graphene, studies have found that graphene is a better nanofiller with excellent thermal and electrical properties [8, 88].

However, the intrinsic properties of the composites are closely related to the dispersion of graphene sheets in the matrix and their interaction with the matrix [98]. Because it has no unstable bonds, graphene has high chemical stability and an inert surface. Moreover, graphene has weak interactions with other media (such as solvents). In addition, there are strong van der Waals forces between graphene layers, leading to agglomeration and thus making it difficult to dissolve graphene in water and common

organic solvents [99, 100].

Rubber is one of the most indispensable and irreplaceable materials in the economy and high technology and is widely used in many fields. The development and utilization of natural rubber have continued for more than 100 years. Chlorinated rubber is synthesized by introducing chlorine atoms to induce flame retardance and sunlight resistance. The introduction of cyano groups into nitrile rubber improves oil resistance. Fluororubber, in which fluorine atoms are incorporated into the side chain of the molecule, has greatly improved heat resistance and antiaging properties. With the development of the chemical industry, rubber materials such as silicone rubber, ethylene propylene diene monomer (EPDM) rubber, acrylic rubber, and styrene-butadiene rubber have been developed and widely used. The strength and flexibility of raw rubber materials are relatively low, so they have little value. They can be used only when reinforcing fillers, antioxidants and other additives are added.

CB and TiO_2 are widely used in various types of rubber reinforcement [101]. Nanocarbon-reinforced materials include those containing CB, fullerenes, CNTs, graphene and graphite. Among these material, graphene is a newly developed nanocarbon material. Since it was discovered and reported in 2004 [21], its excellent physical properties have been gradually demonstrated: it has a large specific surface area (2630 m^2/g), a high Young's modulus (1.1 TPa), a high breaking strength (125GPa), excellent conductivity (106S/m) and excellent thermal conductivity (5300 W/(m*K)) [15, 36, 41]. The revolutionary achievements in this field of material science have also drawn great attention from both academia and industry.

At present, graphene and its derivatives are widely used as an excellent rubber nanofiller in various graphene/rubber composites [17, 39, 40]. To meet functional requirements, the related studies mainly focus on improving the performance of graphene/rubber composites in the following two aspects: ① improving the dispersion of graphene and its derivatives in the rubber matrix and ② enhancing the interfacial interaction between graphene and its derivatives and the rubber matrix. In recent years, researchers have made great breakthroughs in graphene/rubber composites and opened many new research directions in materials, technology and testing methods.

Graphene/rubber composites are very important in the development and utilization of natural rubber. A graphene/natural rubber composite with a mass fraction of 0.5%

prepared by an ultrasonic latex method has better thermal conductivity than natural rubber [102, 103]. The effects of functionalized graphene and CNTs on the composites were investigated by means of X-ray diffraction (XRD) and other tests. The results show that graphene/natural rubber composites have high strain under uniaxial tension, that the stress-strain curve of the modified rubber with a 1% mass fraction of graphene is equivalent to that with 16% mass fraction of CB, and the ultimate tensile strength is even 40% better [104, 105].

To investigate the effect of surface chemistry on the properties of graphene/natural rubber composites, it is very important to control the degree of reduction of GO and change the content of oxidized groups (CO_x). The results show that when the X value is 0.2, the dispersion and interfacial interaction in the graphene/natural rubber composites are optimized [42].

The GO-reinforced composites were prepared by the emulsion aggregation and aggregation methods. Studying the relationship between the fatigue properties and GO addition led to the finding that the composites exhibited the best antifatigue properties when the addition amount of GO was 1 part. Graphene-reinforced natural rubber composites were prepared by emulsion mixing and an in situ reduction method, and the results show that when 0.5 parts of graphene is added, 48% and 80% increases in tensile strength and tensile, respectively, compared to those of raw gum are observed, showing the excellent mechanical properties of the composite [106].

The effect of the morphological structure of reduced graphene oxide (rGO) on the gas barrier properties of graphene/natural rubber composites was studied. The results showed that rGO affected the vulcanization process of natural rubber and crosslinked network construction. The barrier properties of composite materials to oxygen and water vapor were significantly improved, confirming that the morphological structure of the reinforcing fillers is crucial to composite performance [107].

Graphene/natural rubber composites were prepared with multilayer graphene (4 ~ 8 layers) mixed via an emulsion method. The results show that the introduction of multilayer graphene significantly improves the thermal conductivity of the rubber composites [55].

To enhance the reinforcing effect, many nanofiller composites containing graphene have been prepared and applied to the preparation of graphene/natural rubber

composites, including the use of a nano-ZnO/Graphene composite filler (nano-ZnO-GE) to prepare graphene/natural rubber composites. This filler improves the low rolling resistance of graphene/natural rubber composites and is expected to replace ZnO fillers for producing low fuel consumption tires [108].

Graphene/natural rubber composites were prepared using zinc dimethacrylate-functionalized graphene as a filler through liquid phase separation and an in situ reduction process. The performance tests showed that when the addition amount of graphene was 1.4%, the tear strength and modulus were increased by 142% and 76%, respectively. The thermal conductivity is correspondingly improved. The interfacial bonding between graphene and a natural rubber matrix is enhanced by the ionic crosslinking network. The partial replacement of CB with GO or rGO was performed to prepare graphene/natural rubber composites containing two kinds of fillers (NR/CB/rGO and NR/CB/GO), The research findings show that NR/CB/rGO has better flex cracking resistance and lower fatigue heat generation than NR/CB/GO. The graphene and natural rubber substrates were electrically modified and then electrostatically self-assembled to prepare the graphene/natural rubber composites. The percolation threshold of the composites was only 0.21% (volume fraction), while the graphene filled up to 4.16% (volume fraction). Moreover, the composite had a conductivity of 7.31 S/m. The hydrophilicity of GO and the lipophilicity of the matrix were utilized to induce self-assembly and reduction at the water/oil interface in order to prepare a well-dispersed natural rubber composite with a mass loading of 11%. High-loading (30 PHR) graphene/natural rubber composites were prepared by a vacuum-assisted self-assembly method. The test results show that the rubber composites have high conductivity (104S/m) and excellent mechanical properties (tensile strength of 48 MPa, tensile modulus of 1.2 GPa) [109].

The relevant research studies present the following trends:

① To prepare graphene/rubber composites, an increasing number of self-assembly experimental design concepts have been introduced to solve the problem of harsh mixing conditions and poor process economy;

② To solve the problem with the internal interfacial interaction in composite materials, modified graphene composite fillers have been synthesized;

③ Researchers have found that latex can be mixed with natural rubber, styrene-

butadiene rubber, nitrile rubber and other common rubber matrix materials;

④ The applications of graphene/rubber composite materials are continuing to be extended, and some of the technologies have matured;

Notably, the interaction and compatibility between graphene and a polymer matrix are the key factors in the preparation of high-performance polymer-based nanocomposites. To obtain good compatibility, graphene can be uniformly dispersed in the polymer matrix through various methods. Consequently, the modification and functionalization of the graphene surface and the design and control of the interfacial interaction between graphene and the polymer matrix have become urgent problems that need to be solved. In general, the surface modification and functionalization of graphene can be achieved using experimental methods, including hydrogen bonding, π-π stacking, covalent interactions, coordination, nucleation, and crystallization. In this study, the surface functionalization of graphene and the design of the interaction force between different polymers and graphene were studied. The characteristics and the applicable scope of these interfacial forces were also studied. The design of interfacial forces between graphene and polymer matrix will be investigated in the development of high-performance graphene/rubber composite.

2.4.2. Carbon nanotube/rubber composites

The concept of CNTs/polymer composites was proposed and implemented by Ajayan et al. in 1994 [110], and the synthesis, structure, properties, and applications of such composites have been developed for decades.

CNTs, as an allotrope of carbon, have attracted great interest across the world due to their large aspect ratio, nanoscale one-dimensional tubular molecular structure and excellent mechanical, electrical, thermal and optical properties [77]. CNTs have broad application prospects in structural materials, electronic devices, absorbing stealth materials, medical biomaterials, catalyst carriers and other fields. In recent years, the fabrication of CNT/polymer composites has become a very important research direction [16, 111]. Due to the similarity in size and structure between CNTs and polymer chains, the prepared composite material is much better than conventional composite materials with optimized mechanical properties [1]. CNT/polymer composites have great potential applications as high-strength structural materials and have excellent electrical and thermal conductivity. This study will focus on various

factors that affect the performance of composite materials.

Both SWCNTs and MWCNTs can be used to enhance thermosetting polymers such as epoxies, polyurethanes, and phenolic resins [16]. CNTs can also be used to reinforce thermoplastic polymers such as polypropylene (PP), polystyrene (PS) and nylon. CNT composites can be regarded as a particulate composite material with nanoscale size and a high aspect ratio. Compared to the mechanical properties of CNT fillers and resin, the dispersion state of the CNTs is an even more important issue. This article will focus on how to use CNTs to improve the properties of composites. The aspect ratio, the orientation, and the interfacial forces between a CNT filler and a matrix resin are also important considerations in the preparation of composites.

The elastic modulus and tensile strength of PS/CNT composites prepared by dispersing carbon nanotubes with a high aspect ratio of 1.0 wt% in a PS resin matrix are increased by 35% and 25%, respectively [112]. Similar enhancements can also be seen in other literature reports. Some studies have shown that to improve the modulus and strength of composites, the aspect ratio of CNTs should be large. When MWCNT-reinforced epoxy resins with two different aspect ratios are used, only the MWCNTs with a higher aspect ratio can improve performance of matrix [113]. However, the corresponding tensile modulus and strength are only marginally increased (<5%), possibly due to the agglomeration of the CNTs and the poorer interfacial forces with the polymer matrix.

In fact, the dispersion state of CNTs is the most important factor in the preparation of CNT/polymer nanocomposites. Good dispersion not only allows the filler to have a sufficient surface area to bond with the polymer matrix but also prevents agglomerated CNTs from becoming stress concentrators. Therefore, to obtain uniformly dispersed CNTs, the content, length, entanglement, and viscosity of the matrix resin in the composite must be considered. A large number of reports show that CNTs have a key effect on the preparation of CNT composites [114, 115]. When the content of CNT is below the critical filling content, the reinforcing effect of the composite increases with as the CNT content increases. In contrast, when the content of the filler is above the critical filling content, the mechanical properties of the composites will decrease as the CNT content increases and even become worse than the mechanical strength of the pure matrix resin.

The results of these studies lead to the following conclusions:

① A high content of CNTs makes it difficult to achieve uniform dispersion;

② A high content of CNTs will affect the polymerization reaction. When functionalized CNTs are used to prepare polymer composites, the influence of factor 2 is more obvious.

Different CNT dispersion methods greatly affect the mechanical properties of CNT/polymer nanocomposites. The calendaring machine method can achieve the best dispersion of CNTs and therefore can provide the best bending properties.

The use of "uniform dispersion" or "good dispersion" to evaluate the dispersion of CNTs without any distinctive description is inaccurate. For traditional composites, "dispersion" means that the filler is uniformly dispersed in the matrix resin without agglomeration. Geometrically, the free orientation and orientation of the CNTs can cause a large change in the properties of the composite. For example, freely oriented and oriented CNT composites have 10% and 49% increases in storage modulus compared with that of aligned CNT composites [11, 116, 117]. The directional arrangement of CNTs is a special case of CNT dispersion.

Mechanical stretching, melt-spinning, dielectrophoresis, electric and magnetic fields and other experimental methods can be used to achieve the orientation of CNTs in a polymer matrix.

The orientation of CNTs depends on two factors: the CNT diameter and content. Due to their improved stretching fluidity, CNTs with a small diameter can show an increased degree of orientation, whereas large amounts of CNTs can cause agglomeration, resulting in a decrease in the degree of orientation of the CNTs. The orientation of CNTs can maximize the strength and modulus of the composites because the mechanical properties of the composites are anisotropic. That is, the mechanical properties along the orientation direction of the CNTs are increased, but the mechanical properties perpendicular to the orientation direction of the carbon nanotubes are sacrificed. For fiber-reinforced polymer composites, the external force loaded on the CNT/polymer composite must be transferred to the CNT filler to provide the filler with the primary load. The efficiency of load transfer depends on the interfacial forces between the filler and the polymer matrix. It has been reported in the literature that using physical or chemical methods to functionalize carbon nanotubes is an effective

way to increase the interfacial forces between CNTs and the polymer matrix.

The use of CNTs with excellent mechanical properties as a reinforcing filler and polymer matrix composite material can greatly improve the performance of composite materials. At the same time, the excellent electrical, thermal and optical properties of CNTs render CNT/polymer composites very useful. However, the perfect surface of the CNTs makes it difficult to form a good combination between them and macromolecules. The reason is that it is hard to effectively transfer the matrix load to the reinforcing body through the interface. Moreover, obtaining CNTs with excellent mechanical properties is difficult [12, 50, 118]. CNTs are also prone to agglomeration, and their nonpolar surface makes it challenging to achieve good wetting with the polymer, rendering the uniform dispersion of the carbon nanotubes in the polymer matrix extremely difficult and thus affecting the performance of the composite. Problems with the interface and dispersion are consistently the bottlenecks in the development of CNT-reinforced polymer-based composites. CNT/polymer composites are ideal structural materials due to their excellent mechanical properties, light weight, and resistance to chemical and environmental corrosion. However, as noted earlier, their weak interface limits their performance.

2.4.2.1. Mechanical properties

CNTs have a maximum modulus of 1 TPa, a tensile strength 100 times greater than steel, and a density of only 1/6 of that of steel. The good mechanical properties and unique structure of CNTs make them an ideal reinforcing filler for rubber composites.

Natural rubber usually has a modulus at 300% elongation of 1.8 MPa, a tensile strength of 7.1 MPa and an elongation at break of 690%. After 25 parts of ball-milled CNTs were added, the 300% modulus and tensile strength of natural rubber were increased to 12.3 and 25.5 MPa, respectively, whereas the elongation at break decreased to 490%. Lu et al. found that with the addition of MWCNTs, the tensile strength of hydrogenated nitrile butadiene rubber (HNBR) increased from 13.3 MPa to 21.6 MPa, and the 300% modulus increased from 1.30 MPa to 6.63 MPa [119]. The synergistic effect between CNTs and silica greatly impact the mechanical properties of rubber composites. As the amount of CNTs was increased and the amount of silica was decreased, the tensile strength of rubber composites increased from 14 MPa to 17 MPa, but the elongation at break was almost unchanged. When the amount of carbon

nanotubes reached 10 parts compared to 80 parts of silica, the elongation at break of the rubber composites was reduced from 400% to 300% [120].

2.4.2.2. Electrical properties

CNTs have not only good electrical conductivity but also a large aspect ratio. Therefore, as long as a small amount of CNTs are added to the rubber matrix, a completely conductive network structure can be formed to improve the electrical conductivity of the rubber material.

The volume resistivity of rubber decreased from $10^{14}\ \Omega \cdot$ cm to $10^{6}\ \Omega \cdot$ cm when 2 to 4 parts of CNTs were added to styrene-butadiene rubber. Therefore, the threshold value of styrene-butadiene rubber composites is considered 2 to 4, which is far below the 30 ~ 40 copies required for CB/styrene-butadiene rubber nanocomposites [121]. When the amount of CNTs is 1 to 2 parts, the electrical conductivity of CNT/rubber composites is increased from 10^{-13} S/cm to 10^{-4} S/cm, and there is a clear conductive "threshold permeability" phenomenon [44]. The electrical conductivity and dielectric constant of natural rubber increase as the amount of CNTs are increased. When the amount of carbon nanotubes reaches or exceeds 6, however, the growth trend disappears. The addition of CNTs can increase the conductivity of rubber materials, and the required amount of carbon nanotubes is generally less than 5, which can effectively avoid the problem of excessive cost [122].

2.4.2.3. Thermal properties

CNTs have high thermal conductivity and oxidation resistance, and a large number of functional groups exist on their surface and fracture after acid treatment. These functional groups can be directly bonded with the rubber molecular chain to increase the crosslinking density in the matrix. Therefore, mixing CNTs and rubber can not only improve the thermal degradation temperature of rubber but also reduce its heat degradation rate.

After the addition of CNTs, the thermal degradation temperature of styrene-butadiene rubber increased from 447.4°C to 455.1°C, and the thermal degradation temperature of nitrile rubber increased from 445.7°C to 452.7°C [123]. The synergistic effect between clay and CNTs on the thermal stability of HNBR has also been investigated. When the amounts of clay and CNTs added were 5.0 and 0.8, respectively, the temperature corresponding to the maximum thermal degradation rate of HNBR

increased from 452°C to 457°C [124]. No significant initial difference in thermal degradation temperature among the natural rubber, CB/natural rubber composites and CNT/natural rubber composites were observed. However, during thermal degradation, the CNT/natural rubber composites have the highest remaining mass among the samples at every temperature [125]. A comparative test of high-temperature, high-pressure performance between CNT/fluorine rubber composites and CB/fluorine rubber composite shows that the former did not crack or leak when kept at 260°C and 239 MPa for 14 h, whereas the latter had broken and leaked when kept at 260°C and 165 MPa for the same operating time [126]. This result shows that the addition of CNTs helps improve the stability of rubber composites in extreme environments such as high temperatures and high pressures.

Rubber, as a traditional insulation material, usually has a thermal conductivity of 0.1~0.2 W/(m*K). By contrast, CNTs have good thermal conductivity. The maximum thermal conductivity of SWCNTs is predicted to be 6600 W/(m*K), and the thermal conductivity of MWCNTs is 3000 W/(m*K) [25]. A larger aspect ratio can help form a complete and effective heat conduction network structure in the rubber matrix. Therefore, CNTs are ideal fillers for the preparation of thermally conductive rubber composites.

The effect of the amount of CNTs on the thermal conductivity of rubber has been investigated. When the amount of carbon nanotubes is four parts, the thermal conductivity of the rubber increases from 0.08 W/(m*K) to 0.14 W/(m*K) [127]. When the addition amount of carbon nanotubes increases to 20%, the thermal conductivity of thermoplastic polyurethane can reach 0.5 W/(m*K), which is three times greater than that of pure thermoplastic polyurethane [128].

The excellent mechanical, electrical, and thermodynamic properties of CNT/rubber composites give them potential applications in many fields, such as the automobile and aerospace industries. However, although the addition of CNTs can improve the tensile strength and modulus of rubber composites to a certain extent, the improvement has been found to not be obvious, and the enhancement effect of CNTs is not better than that of CB or silica. Moreover, CB and silica are much less expensive than carbon nanotubes.

For example, when CNTs are added to a rubber composite, the elongation at break

remains unchanged or is even reduced. This behavior may due to the "agglomeration" and the poor interface between the matrix and filler. The structure of the CNTs is another major contributing factor. In addition, although CNT/rubber composites have fairly improved thermal conductivity compared with that of raw rubber, they does not show the obvious phenomenon of "threshold infiltration", which may mainly be due to the poord association between the rubber and CNT filler.

The heat conduction in composites of rubber and CNTs is dominated by the "phonon conduction mechanism". When the CNTs are dispersed in a rubber matrix, the phonon vibration among the scattered CNTs is weakened due to obstruction by the polymer molecular chain. Therefore, to study the thermal conductivity of CNT/rubber composites, we can research the structure of the thermal conductivity network in composites and the thermal interface between CNTs and rubber matrices [129-131].

At present, the traditional thermal conductive fillers used for preparing thermally conductive insulating polymer composites can be mainly divided into the following categories:

① Metal filler, such as copper, silver, gold, nickel, and aluminum.

② Carbon filler, such as amorphous carbon, graphite, diamond, CNTs and graphene.

③ Ceramic filler, which is the most widely used type, such as boron nitride, aluminum nitride, silicon nitride, silicon carbide, magnesium oxide, beryllium oxide, aluminum oxide, zinc oxide, and silicon oxide.

Commonly used carbon fillers are carbon fiber, graphite, diamond powder, CNTs and graphene. Carbon has many different allotropes, and different allotropes have very different thermal conductivities. For example, the thermal conductivity of amorphous carbon is only 0.01 $wm^{-1}k^{-1}$, whereas the thermal conductivity of diamond at room temperature can exceed 2000 $wm^{-1}k^{-1}$.

Recently reported thermal conductivity values of carbon allotropes and the most widely used thermal fillers are shown in Table 2-1.

Table 2-1 Thermal conductivity of various fillers at room temperature

Material	Thermal conductivity	Material	Thermal conductivity
Ag	417	BeO	240
Au	315	MgO	36
Al	240	Al_2O_3	30
Ca	380	NiO	12
Fe	63	SiO_2	1
Mg	103	ZnO	21
Ni	91.4	CaO	15
Pt	71.4	Si_3N_4	180
Sn	67	BN	290
Be	219	AIN	300
Zn	121	SiC	80-120
Ti	22	Mica	0.71
Pb	35	Clay	0.15-2.5
Cu	398	MWCNTs	3180
Graphite	209	SWCNTs	3500
Graphene	4840-5300	Diamond	2000

Diamond has extremely high thermal conductivity and is now used in the semiconductor industry to help dissipate heat.

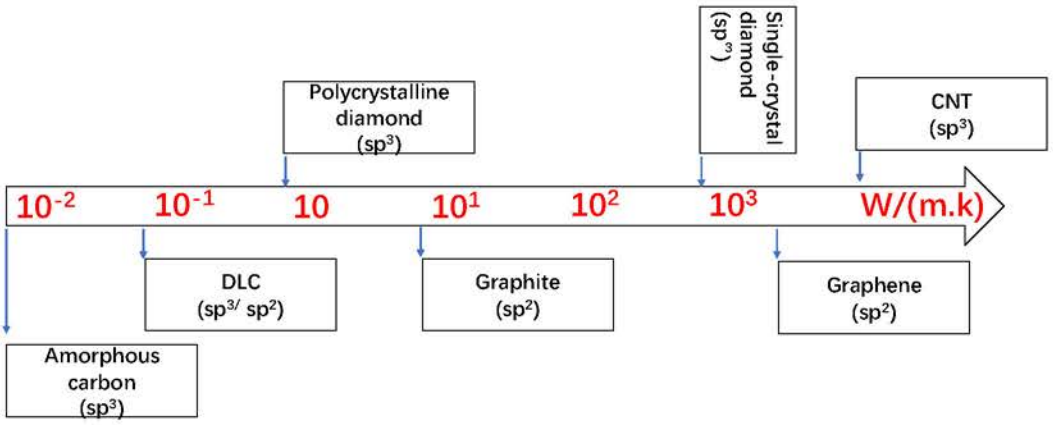

Figure 2-1 Thermal conductivity of various carbon allotrope fillers

Molecular dynamics simulation analysis of a functionalized CNT composite shows that CNT functionalization can reduce the thermal interface of the CNTs and then reduce their thermal conductivity. When the percentage of functionalized carbon reaches 1%, further CNT functionalization will no longer affect the thermal conductivity; that is, the thermal conductivity will be close to a constant value [132]. When different types of CNTs are used as a thermal conductivity filler in an epoxy composite, the MWCNTs have a smaller specific surface area than the SWCNTs, the interface between the two phases in the composites is weakened, and the effect of scattering on phonon conduction is weaker. Thus, the thermal conductivity of the composite will be increased more. Another reason is that except for the outermost layer, the inner wall of the CNTs does not interact with the epoxy matrix and therefore has a lower coupling loss of the phonon conduction. This method is also useful to improve the thermal conductivity of the composites [133].

The purification of CNTs has a great influence on the thermal conductivity of composites. One study found that acid treatment of CNTs may cause defects, which greatly affect their thermal conductivity. During the preparation of polymethylmethacrylate matrix composites using MWCNTs or SWCNTs, the thermal conductivity of the unpurified CNT composites is much higher than that of purified CNT composites. The length and mixing state of CNTs also have a great influence on the ultimate thermal conductivity [121].

2.5. Principles of fiber-reinforced composites

2.5.1. Interface theory

In composite materials, the region between the filler and matrix, which appears discontinuous, is referred to as the interface of the composite. In fact, the filler and matrix are not completely separated: there is a three-dimensional transition region with a gradient of energy, structure, and composition between the two phases. Therefore, "interface layer" or "interface phase" can better describe the state of the composite interface. The reinforcing fillers dominate the composite load force, and the role of the matrix material is to bond the reinforcing fillers together and give the material a certain rigidity and a specific geometry. The role of the interface between the filler and matrix is to load uniform and effective conduction from the matrix to the reinforcing filler, which can effectively block the further expansion of cracks. Thus, the performance of the interface in composites is very important.

As the research on the interface of composite materials intensifies, a variety of theories of the interface of composite materials have been proposed, including infiltration theory, chemical bond theory, diffusion theory, gear connection theory, diffusion theory, electrostatic theory, transition layer theory and weak boundary layer theory, among which infiltration theory and chemical bond theory are the most influential.

2.5.1.1. Infiltration theory

Different aggregates of fillers produce different interfaces. The most typical solid-liquid interface for polymer-based composites is infiltration theory, which was proposed by Zisman in 1963 [127]. In the infiltration theory, two-phase infiltration is considered as one of the basic conditions for forming an interface. According to the infiltration theory, the bonding strength of the interface is affected by infiltration through interface defects and breakage. Due to the rough surface of the matrix, the unevenness of the interface, air entrapment and other factors, the interface infiltration process can produce a large number of tiny holes. In addition, the size of the holes is closely related to the infiltration process. Therefore, infiltration has an important effect on the interface defects and bonding properties of the composites. Poor infiltration can result in defects at the interface, leading to reduced interfacial strength, Good infiltration improves fracture energy and adhesion, which in turn leads to enhanced bond strength.

Good contact between the two phases at an interface is beneficial, as it can reduce defects and increase the number of mechanical anchor points of contact and the fracture energy [134].

Infiltration theory indicates that the best infiltration condition in terms of the interface strength is to match the polarity and surface tension of the components. At this stage in the field of polymer-based composite interfaces, the study of infiltration theory mainly focuses on enhancing the surface energy of the body. Matching surface energy of the reinforcing filler to the surface tension of the polymer matrix has been found to be the key factors in improving the interfacial strength of the composite. Therefore, increasing the free energy of the surface of the reinforcing filler improves the infiltration of the filler and increases the interfacial adhesion strength between the reinforcing filler and the polymer matrix. However, there has been controversy regarding infiltration theory as to whether the polarity corresponds to the interface performance. In additional studies, researchers also found that infiltration is not the sole factor that makes an interface bond well. Since bonding is an extremely complicated process, it cannot sufficiently be explained only by infiltration theory, and there are many aspects in the infiltration theory that need to be improved[135].

2.5.1.2. Chemical bond theory

Chemical bond theory is the most widely used and most accepted theory currently. The core idea is that chemical bonds between the reinforcing filler and the matrix plays a major role in the interfacial adhesion strength. However, the van der Waals forces between the two phases will weak the impact of chemical bonds on the interfacial bonding strength and cause the mechanical interlocking of the rough surfaces. The theoretical basis for the chemical bond theory is the fact that the chemical bond has a much higher binding energy (50-250 kcal/mol) than van der Waals forces (2.5-5 kcal/mol) and thus can effectively prevent the movement of the matrix molecules at the interface. However, the mechanism of mechanical interlocking is a purely mechanical action, and the relative sliding force is hindered by the friction generated by the two-phase contact, which has little effect compared with the chemical bonds. According to the chemical bond theory, the two-phase surface should contain reactive groups that can react chemically to form the interfacial phase [136-139].

However, the chemical bond theory is old interface theory that is not perfect. There

are a large number of interfacial phenomena that cannot be explained by the chemical bond theory. Moreover, there are still some controversies in the development of this theory. Although the chemical bonds formed at the interface of two phases are stronger than the van der Waals forces, the van der Waals forces still exist in the interface. The formation of chemical bonds requires reactive sites to be close each other and satisfy certain quantum chemical conditions. Therefore, the number of chemical bonds formed at the interface is limited. During the process of strengthening the matrix design and studying the interface, researchers must consider the impact of various factors, and the role of chemical bonds, such as hydrogen bonding and acid-base effects, should be included.

2.5.1.3. Gear connection theory

Gear connection theory refers to the presence of a microstructure. The roughness on the surface of the solid can increase the specific surface area. The large surface can improve the wetting state of the substrate and the reinforcing filler and then provide a bonding center of contact. It will increase the interfacial bonding strength between the matrix and the reinforcing filler.

2.5.1.4. Diffusion theory

Diffusion theory states that matrix self-adhesion and the bonding between the two phases are generated by molecular diffusion at the interface. However, this theory has great limitations. For polymer-based composites, interfacial diffusion does not occur between the reinforcing filler and the polymer. Therefore, the diffusion theory cannot be used to explain such composites.

2.5.1.5. Electrostatic theory

The electrostatic theory states that the matrix and reinforcing filler have different electronic states and structures. Furthermore, when they are in contact with each other, electron transfer occurs to form an electrical double-layer structure, and electrostatic force plays a major role in forming the structure of the composites.

2.5.1.6. Transition layer theory

This theory suggests that there is a transition layer between the filler and the matrix to eliminate the internal stress in the composites. However, the shape and function of this transitional layer are still controversial. One theory is that the transitional layer has a

flexible layer, that is, a "deformation layer", that can relax stress. The other theory is that the transition layer is not a flexible layer; however, the modulus of the "inhibition layer" between the matrix and the reinforcing filler can uniformly transmit stress.

2.5.1.7. Weak boundary layer theory

The weak boundary layer theory of considers that due to the processing factors and structural defects, the composite system inevitably has a weak boundary layer where damage is most likely to occur. The probability that this weak boundary layer exists at the interface is only 1/3. Therefore, the probability of damage occurring at the interface is small, and most of the damage occurs in the reinforcing filler and the matrix. Thus, we can see in the analysis of interface failure probability that consideration of the interfacial properties and two phases is lacking and that the probability that weak boundary layers are present is the same as the probability that two phases are present. However, the probability of the presence of a weak boundary layer is in fact far greater than that of the two phases. Therefore, there are some problems in theory that need to be solved urgently.

2.5.2. Interface bonding type

Based on the existing interface theory, to highlight the main contradictions in interfacial research, omit complex and nonessential factors, and establish the most important factors affecting the interface and their relationship with interface performance, the types of interfaces are divided into mechanical combinations and chemical combinations.

2.5.2.1. Mechanical combination

Reinforcement between the matrix and the filler depends on the microstructure of the rough surface. Chimerism and interlocking connection are shown in Figure 2-2. Mechanical binding is mainly affected by two factors: (1) the filler surface with a high degree of roughness, which facilitates the formation of mechanical interlocking and (2) contraction of the base matrix hoop reinforcing filler, which can enhance the mechanical interlocking strength. In fact, a purely mechanical bond is absent (no chemical action), and there is always a weak Van der Waals force between the matrix and the reinforcing filler; thus, mechanical bonding is more accurate, as mechanical bonding dominates. Under normal circumstances, mechanical and chemical bonding coexist. In addition, under normal circumstances, when the stress is parallel to the

interface, the load can be effectively transmitted.

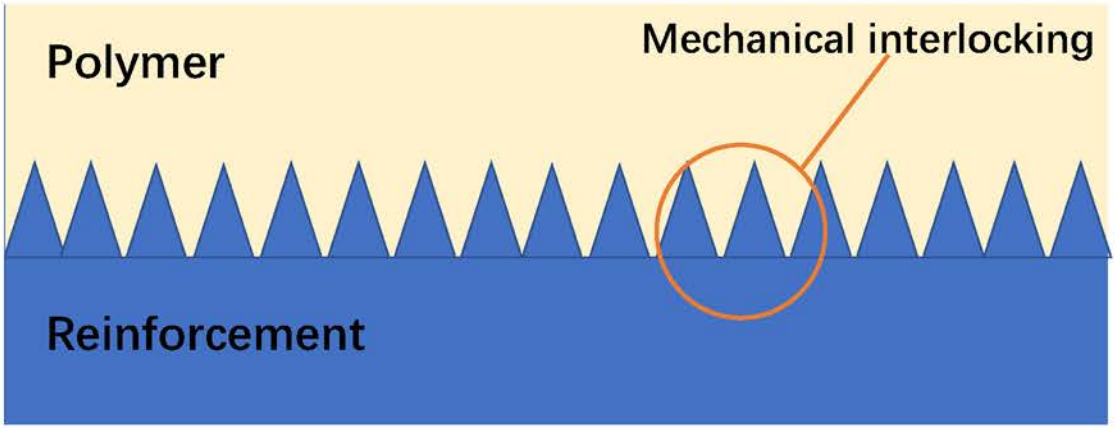

Figure 2-2 Sketch of mechanical interlocking at the interface

2.5.2.2. Chemical combination

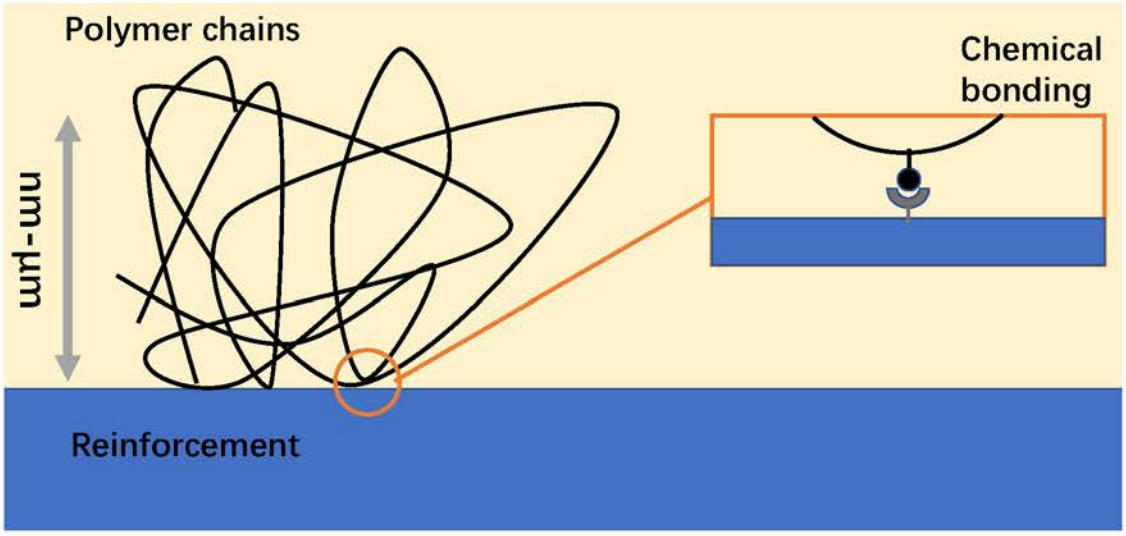

Figure 2-3 Sketch of chemical bonding at the interface

The matrix reacts chemically with the reinforcing filler, forming a chemical bond at the interface (see Figure 2-3). This reaction occurs with surface wetting control. At the same time, we generally cannot think that the chemical reaction itself is chemical binding, and the interface system can be described as a chemical combination only after the chemical reaction. If the interface has a large number of brittle compounds after the reaction, which results in the interfacial embrittlement, it cannot become a chemical combination but instead should be considered a reaction inhibited combination. To achieve a good chemical combination, researchers must choose the best preparation parameters to control the extent of the interfacial reaction.

2.5.3. Thermal conductivity of composites

According to thermodynamics, heat is moving, rotating, and vibrating energy linked to molecules, atoms, electrons, and their components. Therefore, a material's thermal conduction mechanism must be closely related to the movement of the microscopic particles that make up the material. Different substances have different thermal mechanisms and different thermal conductivities. However, the conduction of all matter is the result of collisions and transmission of microscopic particles within that matter. Solid-state thermal carriers are divided into 3 species: electrons, photons, and phonons. The electron plays the main role in the intrinsic heat conduction found in, for example, most metals, polyacetylene, polypyrrole, polythiophene, polyaniline, poly-p-phenylene and several other conductive polymers, as it carries charge. Although the migration process carries much energy, the thermal conductivity of the filler is high, leading to low heat generation. Since photons play a major role in thermal conductivity, the material must have good thermal permeability. Thus, certain glass or single-crystal materials are generally most widely used. Furthermore, at a specific temperature, photons will play a significant role in thermal conductivity. For other materials, the ordered crystal structure forms the phonon free path, which is much larger than the polymer material. As a result, the thermal conductivities of metal oxides and some inorganic nonmetallic materials are much higher than those of polymer materials.

A phonon is not a real particle, and it can be produced and destroyed. In thermally conductive polymer materials, electrons are tethered, and phonons are their main heat-conducting carrier. Thermally insulative polymer materials can be divided into crystal and noncrystal. From the point of view of the thermal mechanism, the crystal thermal conduction mechanism is usually described by the concept of the phonon. The amorphous thermal conduction mechanism depends on the irregular arrangement of molecules or atoms around a fixed position thermally vibrating and subsequently conveying energy to adjacent molecules or atoms. As a noncrystalline material can be seen as an extremely fine crystal, the phonon concept can also be used to analyze its thermal conductivity. However, the polymer itself is not highly crystalline, and its crystallization is not complete. The molecular and lattice anharmonic vibration, resin interface and defects will cause phonon scattering, which means that the thermal conductivity of the polymer is weak. To make a highly thermally conductive polymer, the polymer molecules should have a conjugated structure or perfect crystalline

orientation structure. However, the current technology for heat-conducting polymer processing technology is complex and is inadequate for large-scale production. Therefore, according to the modern microscopic theory of solid-state heat conduction, preparing a thermally conductive polymer-based composite material by doping a polymer matrix material with a metal oxide or an inorganic nonmetal powder is currently still one of the main method to obtain a high-thermal-conductivity material.

For thermally conductive polymer-based materials, the thermal conductivity depends on the synergistic effect of the polymer matrix and the thermally conductive filler. The thermal conductive filler dispersed in the resin has various shapes, such as granular, fibrous, and sheet-like. When the filler is added in a relatively low amount, the filler particles are mainly present in an isolated form in the polymer matrix without mutual contact with other particle. In this case, the continuous phase is also a polymer matrix, and the filler is coated as a dispersed phase, much like the "island two-phase system" structure in a polymer blend. However, when the filler is added at the percolation threshold, the filler or filler aggregates will contact each other in the local conductive chain, or a thermally conductive network will be formed in the composite material. If the amount of filler is increased further, the local heat conduction chain or the heat conduction net will be connected and will penetrate each other to form a heat conduction network that runs throughout the whole polymer matrix. Then, both the polymer and the filler will become a continuous phase, and the heat conduction network of the filler aggregates and the polymer matrix will form a mutual penetration network structure. As a result, the thermal conductivity of filled composites is significantly improved. As shown in the figure, when the heat-conductive filler is added in a specific amount, the particles come into contact with each other to form a path, and the polymer will transition from a poor conductor of heat to a good conductor of heat. This transformation is the so-called "percolation"; thus, the percolation theory applies to the research and development of filled thermally conductive composites. Notably, the thermal conductivity of the material can be greatly and rapidly improved only when the conduction direction of the heat flow is exactly the same as the orientation direction of the heat conduction net chain. If the conduction direction of the heat flow and the orientation direction of the heat conduction net chain are not the same (e.g., the direction of the heat conduction net chain is perpendicular to the conduction direction of the heat flow), the filler will become an obstacle to heat conduction and cause high

thermal resistance, which results in the material having very poor thermal conductivity. Therefore, to obtain high-thermal-conductivity polymer composites, the network of thermal conductivity within the system chain must be as large as possible.

2.6. Functionalization of carbon nanomaterials

Due to their large aspect ratio and specific surface area, carbon nanomaterials are easily agglomerated. This limitation restricts the application of carbon nanomaterials. It is hard to fully take advantage their high strength and high toughness when they are used as a filler in composite materials, and the composites cannot achieve a high fiber volume content. At the same time, most carbon nanomaterials are hydrophobic and thus have low compatibility with the resin, and poor interfacial bonding. Carbon nanomaterials also cannot transfer stress effectively [8, 48]. Surface modification has therefore become an effective method to solve these two problems. The modification of carbon nanomaterials is usually divided into two types of methods: chemical modification (covalent bond modification) and physical modification (noncovalent modification) [51, 140, 141]. Among the many surface modification methods, noncovalent surface modification is the most common approach. In this method, long polymer chains are surrounded by carbon nanomaterials, or surface-active molecules are adsorbed onto the surface of the carbon nanomaterials [57, 142]. Therefore, the modified molecules and carbon nanomaterials combine only through physical adsorption. The covalent bond surface modification method consists of grafting chemical groups to the surface of carbon nanomaterials and using the controlled polymerization method to control the grafting structure. The purpose of these surface modification methods is to modify the surface of the carbon nanomaterials chemically, which can damage the structural integrity of the carbon nanomaterials and reduce their mechanical properties. Different surface modification methods have their own advantages and limitations, so the choice of which method depends on the field in which the polymer/carbon nanocomposite is applied.

2.6.1. Noncovalent functionalization

Since the noncovalent surface modification process does not harm the structure of carbon nanomaterials and thus can ensure their integrity, researchers have considerable interest in it. Noncovalent surface modification involves adjusting the interfacial properties of carbon nanomaterials [143]. The most frequently used methods are

functionalization by aromatics, surfactants, or polymers or the incorporation of ketones. With the above methods, noncovalent modification can maintain the excellent inherent properties of the carbon nanomaterials while significantly improving their solubility. However, physical modification of the surface of the carbon nanomaterials can be a problem when creating a load-bearing structure [144, 145].

Modified noncovalent carbon nanomaterials have been fabricated based on the principle of gel stabilization. Researchers used charged inorganic ZrO_2 nanoparticles as a stabilizing medium and found that the solution of ZrO_2 in the carbon nanotubes was very stable. This stability is due to the electrical repulsion between ZrO_2 particles, which allowed the carbon nanotubes to disperse uniformly in aqueous solution [32, 146].

Aromatic molecules such as pyrene, porphyrin, and their derivatives can be bonded to the surface of carbon nanomaterials through the stacking effect of π-π bonds. Thus, they constitute a new method for the noncovalent modification of carbon nanomaterials. Conjugated polymers are considered the best species for the noncovalent modification of carbon nanomaterials because of their aromatic rings and van der Waals forces [147].

At the same time, a surfactant can also induce surface modification, and the physical adsorption of surfactants reduces the surface energy of carbon nanomaterials through electrostatic repulsion, thereby effectively preventing carbon nanomaterial agglomeration [143, 148, 149].

The efficiency of this method depends directly on the nature of the surfactant, the chemical medium, and the polymer matrix. The following surfactants have been used in combination with carbon nanomaterials [150, 151]:

① Nonionic surfactants such as polyoxyethylene lauryl ether and Triton X-100

② Anionic surfactants such as sodium dodecyl sulfate (SDS) and sodium dodecylbenzenesulfonate (SDBS)

③ Cationic surfactants such as dodecyltrimethylammonium bromide (DTAB) and cetyltrimethylammonium 4-vinylbenzoate(CTVB)

Surfactants are very effective in dispersing carbon nanomaterials, but because of their toxicity, they cannot be applied in the biomedical field and thus limit the potential of surfactants in biomedical applications [34, 111, 137, 152].

2.6.2. Covalent functionalization

Carbon nanomaterials generally have many defects on their surface, and these defects lead to increased reactivity and numerous reaction sites. Examples of such defects include sp^3-hybridized defects and lattice defects.

Chemical modification uses covalent bonds to graft reactive groups onto the surface of carbon nanomaterials, and the reaction can be performed on the surface of carbon nanomaterials with defects. Covalent bond functionalization occurs on highly chemically reactive molecules, along with the shift from sp^2 hybridization to sp^3 hybridization and the reduction of the p-conjugated system in the graphite layer. Initially, researchers considered the surface of carbon nanomaterials to be inert. Because the C-F bond in fluorocarbon nanomaterials is weaker than the C-F bond in alkyl fluorides, the functionalization of carbon nanomaterials by using fluorination allows another functionalization step to afford substituents. For example, Stevens et al. successfully substituted fluorine with amino and alkyl hydroxyl groups. Cycloaddition, nitrogen addition, chlorination, bromination, and hydrogenation reactions have also been used to successfully modify the surface of carbon nanomaterials [95, 153-155].

Another method is the functionalization of carbon nanomaterials defects. Treatment of carbon nanomaterials with a strong acid leaves cavitation defects on the surface, and these defects feature abundant oxygen-containing functional groups. In particular, carbon nanomaterials are easily opened up by strong acids (sulfuric acid, nitric acid or their mixtures), other strong oxides (potassium permanganate, ozone) and reactive plasma treatment. Oxygen-containing reactive groups such as carboxylic acids, ketones, alcohols, and esters bond with surface defects. These reactive groups have high chemical reactivity and can act as reaction precursors to facilitate subsequent reactions such as silanization, polymer grafting, esterification, thiolation, and biomolecular reactions. Covalently modified carbon nanomaterials can be dissolved in many organic solvents due to the various polar or nonpolar groups on their surface [144, 156].

However, there are inevitable disadvantages of chemical modification. In functionalization reaction, especially after ultrasonication treatment, there are many defects on the carbon nanomaterials. In extreme cases, the carbon nanomaterials will be broken up into small fragments. The destruction of the structure leads to a serious reduction in their mechanical properties and π-electron density. In addition, the damage

to the π-electron conjugation system is unfavorable for the conductive properties of carbon nanomaterials because the defects lead to the scattering of electrons and phonons, which decreases conductivity [157, 158].

2.6.3. Cross-scale reinforcing filler

Making carbon nanotubes into a buckypaper cross-scale reinforcing filler is a viable functionalization method. Carbon nanotube buckypaper refers to physically or chemically entangled carbon nanotubes forming a paper-like thin layer structure. Compared with a traditional carbon nanotube film, carbon nanotube buckypaper has excellent mechanical properties, excellent electrical properties, and great application value in sensors, brakes, electrodes, capacitors and fuel cells [159]. The relatively mature technology for the preparation of carbon nanotube buckypaper also offers great potential to enhance the development of composites [160]. The structure of carbon nanotube buckypaper is mainly determined by its preparation method. The current preparation methods for carbon nanotube buckypaper are divided into one-step and two-step methods. The one-step method mainly consists of the preparation of carbon nanotubes via chemical vapor deposition, while the two-step method includes suction filtration, spin-coating and rolling [161].

2.6.4. Plasma surface modification

In physics, plasma is defined as an ionized gas containing positively and negatively charged particles in the same quantity [162]. Plasma includes free electrons, particles, free radicals, UV rays, and highly excited neutrals or dots of matter. The complete plasma is electrically neutral. According to the gas temperature, plasma can be divided into hot plasma and cold plasma [163, 164]. The temperature of hot plasma is equal to the electron temperature, and the gas is completely ionized. In cold plasma, the gas temperature is much lower than the electron temperature, and the gas is not fully ionized [165]. The temperature of all substances in hot plasma, such as electrons, ions, and neutrons, is the same; one example is terrestrial fusion plasma. Plasma balance requires a very high temperature, namely, between approximately 4000 K and approximately 20000 K. By contrast, for cold plasma, the neutral and positively charged species have a low temperature close to room temperature. The electron temperature is much higher than the temperature of other particles because the electron weighs little and thus can be accelerated to a high speed after application of an electromagnetic field. Thus, the

plasma is not stable and can still react at low temperatures [166-168].

Since no waste and toxins are produced during the plasma process, it provides an efficient and environmentally friendly treatment option for industrial applications [169]. At the same time, it has also attracted considerable attention in the life sciences regarding, for example, environmental issues and biological applications. Recently, methods for growing carbon nanotubes using plasma-assisted chemical vapor deposition have been reported, and gas plasmas have been widely used in surface modification treatment [170, 171]. Plasma processing is commonly used for thin-film deposition and for the fabrication of resistive materials. In the field of microelectronics, plasma surface modification is used to make microelectronic circuits and materials [172, 173]. The diverse applications of plasma processing stem from its advantages.

Plasma treatment does not change the size, shape, geometry and type of materials and is highly repeatable. Plasma surface treatment can be divided into different types according to the product: plasma corrosion, plasma polymerization, and plasma modification. Depending on the different gases used, material surface properties and plasma parameters can determine the grafting effect. The plasma treatment process is conducted using a variety of gases, such as O_2, N_2, NH_3, and CF_4, to add chemically reactive groups in the material surface. Compared with chemical treatment, plasma surface treatment is carried out rapidly in a solvent-free environment. Adjustment of plasma parameters such as the voltage, gas, pressure, and treatment time allows a series of functional groups to be grafted onto the material surface.

For the modification of carbon nanomaterials, plasma treatment not only has the advantages described above but also can control the quantity of functional groups grafted to the surface of the nanomaterials. This advantage is important for grafting groups onto the surface of carbon nanomaterials in order to change their thermal conductivity [174, 175].

2.6.4.1. Plasma corrosion

Nonreactive treatment occurs when carbon nanomaterials are treated with argon (Ar) plasma. The argon RF plasma processing of vertically grown carbon nanomaterials has been extensively studied. The results show that exposing the surface of carbon nanomaterials to inert argon plasma produces an effective corrosion and cleaning effect, resulting in structural changes in the carbon nanomaterials and increases in field

emission.

The orientation effect of the carbon nanotubes has been observed to be enhanced after argon RF plasma treatment, and argon plasma is also used to excite the surface of the carbon nanotubes in preparation for subsequent grafting [176].

Using hydrogenation by performing RF plasma treatment under hydrogen increased the number of defects and improved the field emission properties, which is due to the appearance of nodules produced by the bending of the graphite layer along the sidewalls of the material. In hydrogen RF plasma processing, hydrogen ions bombard the surface of carbon nanomaterials to remove carbon from the surface in the form of methyl groups. However, a small portion of the methyl groups are redeposited on the surface. The electrical properties of carbon nanomaterials (the formation of sp^3 defects in the sp^2 graphite network) and the changes in their geometry lead to improved field emission properties.

2.6.4.2. Plasma chemical modification

Carbon nanomaterials can be fluorinated by plasma treatment. Fluorination is one of the most effective ways to modify carbon nanomaterials, as it can be followed by derivatization [177, 178]. Unlike other fluorination reactions [179], CF_4 plasma treatment can enhance the activity of carbon nanomaterials and aliphatic amine compounds at room temperature. It has been reported that two minutes of CF_4 plasma treatment can increase the field emission current of materials [180]. When carbon nanomaterials are subjected to the CF_4 plasma, fluorine atoms are grafted onto the surface of the material. The quantity of grafted fluorine atoms was determined by X-ray photoelectron spectroscopy (XPS), and the Raman spectrum reflected the change in the structure of the surface-treated carbon nanomaterials. High-resolution TEM shows that the outer wall of the materials is grafted with fluoride. Carbon nanomaterials treated with NH_3 glow discharge plasma are superhydrophobic [181]. Hydrophobic carbon nanomaterials are obtained in less than one minute of processing time. Work on grafting oxygen-containing groups by plasma treatment has been extensively reported. Carboxyl and hydroxyl groups are grafted onto the surface of carbon nanomaterials by O_2 and CO_2 RF plasma treatment to form polar groups and increase the binding of carbon nanomaterials to polymer resins [182]. The oxygen content, as calculated by XPS, is up to 14%. The oxygen grafting efficiency during the plasma treatment can be

obtained by measuring the contact angle. The results show that μ-wave plasma treatment leads to better wettability. Other types of plasma treatments, such as atmospheric pressure dielectric barrier discharges, are also used for the microwave plasma grafting of oxygen-containing groups onto the surface of carbon nanomaterials and are easy to handle [183-186].

2.7. Preparation of rubber composites

There are various preparation methods for composites. The main purpose of the preparation method is to mix the matrix and filler and provide high-performance composite materials. Different processing methods affect the distribution of filler in the matrix and affect the aspect ratio and orientation of the filler. As a result, choosing the right process is essential for obtaining a composite with excellent properties.

2.7.1. In situ polymerization

In situ polymerization is a reaction that produces composite materials using a pretreatment method. In the polymerization process, the viscosity of the system will slowly increase, the fillers are evenly dispersed in the matrix, and the final system is transformed from a liquid to a solid. This method causes less damage to the aspect ratio and morphology of the filler, and the fillers are very well dispersed in the system. As a result, industrialized production has been widely used. The most common polymers include polyamides, epoxies, phenolic resins, and polymethylmethacrylate.

2.7.2. Solution mixing

The solution mixing method consists of dissolving the polymer in the solvent first, then adding the filler to the mixture, and finally removing the solvent by precipitation, coating or drying to obtain composites. Due to the large amount of solvent used in the solution mixing process, the viscosity of the system is low, and the filler can be dispersed using vigorous mechanical stirring or ultrasound to obtain a composite material with excellent properties. The solution mixing method is widely used for preparing composites in the laboratory because of its convenience and speed. However, it also has some disadvantages that limit the widespread use of solution mixing in the industry. First, the solution mixing method requires the use of a large amount of solvent, which can negative impact human health during operation and cause considerable environmental pollution. Second, the choice of solvent is a challenge. It is difficult to find a solvent that is a good solvent for both the polymer and the filler. In the dispersion

process, it is often necessary to laboriously solve the problem of filler dispersion. Finally, the solution mixing method for preparing composite materials is costly and difficult to apply in industrialized production [187].

2.7.3. Melt blending

As a simple, quick and easy-to-industrialize processing method, melt blending is the most commonly used blending technique for thermoplastic polymers [188]. The melt blending method is a simple and feasible method and is very suitable for industrial production. Most of the current composite materials are obtained by melt blending. However, it also has its shortcomings. The polymer is easily degraded during processing, and the aspect ratio of the filler can also be damaged. Therefore, controlling the parameters during the process is key to preparing composite materials with excellent performance [189].

When the content of carbon nanotubes is high, a perfect conductive network is formed. As a result, the order of blending has little effect on the electrical conductivity of the composites.

2.8. Conclusions

In recent years, with the development of science and technology, industry has placed more requirements on advanced rubber materials. Traditional rubber materials are not able to satisfy the new requirements of functionality and diversity. Since new carbon nanomaterials, such as carbon nanotubes, graphene and GO, have been discovered, new areas for high-performance rubber composites have emerged. In addition, using carbon nanomaterials to prepare high-performance rubber composites has attracted widespread attention in industry. Compared with traditional rubber fillers such as CB, TiO_2 and SiO_2, carbon nanotubes and graphene can give rubber composites enhanced properties, such as high thermal conductivity, fatigue resistance, and considerably improved mechanical properties. As a result, using carbon materials to prepare rubber composites is development trend in industry. In this research, we explore the interaction between carbon nanomaterials and rubber matrices, and we graft different functional group onto surface of carbon nanomaterials to improve the interaction force. Then, we use the modified carbon nanomaterials to prepare high-performance rubber composites.

1) Using oxygen-containing groups on the surface of graphene and GO to carry out amidation and grafting reactions. We can graft various functional groups, such as

long-chain alkyl groups, PS, styrene-ethylene/butylene-styrene (SEBS) and PP chains. This process will greatly improve the dispersion of carbon nanomaterials in the rubber matrix.

2) Using different chemical treatments to modify the surface of MWCNTs, such as acid oxidation and amination. In addition, we study and explore the effect of different treatments on the morphology, structure and dispersion of carbon nanotubes. We also explore the interfacial bonding strength between carbon nanotubes and rubber matrices.

3) The J-integral is used to characterize the antifatigue properties of rubber composites. We also characterize the process of crack initiation and crack propagation by the J-integral. The strain energy density, which can predict the fatigue lifetime of rubber composites, is calculated from the area under the stress-strain curve. In addition, we explore how to use the strain energy density to measure the crack growth rate in the constant tensile strain condition.

4) Using a fracture method to explore the dynamic fatigue properties of rubber composites. First, we prepare rubber composites by mechanical blending. Then, precut specimen are used to test fatigue properties of the rubber composites. In addition, we explore the synergies between different key factors in carbon nanomaterials and the effect of the dispersion state, filler network, strain-induced crystallization and tearing energy on rubber composites.

Chapter 3. Materials and Methods

3.1. Materials and reagents

The materials and reagents used in this thesis are as follows.

Table 3-1 Materials and reagents

Materials and Reagents	Standard	Company
MWCNTs		Shenzhen Nangang Port Technology
Sulfuric acid	AR	Sigma-Aldrich Co., Ltd
Nitric acid	AR	Sigma-Aldrich Co., Ltd
Thionyl chloride	AR	Sigma-Aldrich Co., Ltd
Dimethylformamide (DMF)	AR	Sigma-Aldrich Co., Ltd
Ethylenediamine	AR	Sigma-Aldrich Co., Ltd
Tetrahydrofuran (THF)	AR	Sigma-Aldrich Co., Ltd
Dichloromethane (DCM)	AR	Sigma-Aldrich Co., Ltd
Ethanol	AR	Sigma-Aldrich Co., Ltd
Sodium hydroxide	AR	Sigma-Aldrich Co., Ltd
Hydrochloric acid	AR	Sigma-Aldrich Co., Ltd
Sodium carbonate	AR	Sigma-Aldrich Co., Ltd
Sodium bicarbonate	AR	Sigma-Aldrich Co., Ltd
Potassium hydrogen phthalate	AR	Sigma-Aldrich Co., Ltd
GO		Shenzhen Nangang Port Technology
Graphene		Shenzhen Nangang Port Technology
Octadecylamine	97%	Sigma-Aldrich Co., Ltd
Dicyclohexylcarbodiimide	99%	Sigma-Aldrich Co., Ltd
Thionyl chloride	AR	Sigma-Aldrich Co., Ltd
Propargyl alcohol	99%	Sigma-Aldrich Co., Ltd
Triethylamine	AR	Sigma-Aldrich Co., Ltd

Chloroform	AR	Sigma-Aldrich Co., Ltd
CuBr	AR	Sigma-Aldrich Co., Ltd
PMDETA	AR	Sigma-Aldrich Co., Ltd
Styrene	AR	Sigma-Aldrich Co., Ltd
Chlorobenzene	AR	Sigma-Aldrich Co., Ltd
Styrene-ethylene/butylene-styrene (SEBS)	G1651	Shell Co., Ltd
Dioxane	AR	Sigma-Aldrich Co., Ltd
Trimethylchlorosilane	AR	Sigma-Aldrich Co., Ltd
$SnCl_4$	AR	Sigma-Aldrich Co., Ltd
NaN_3	AR	Sigma-Aldrich Co., Ltd
Diaminodiphenylmethane (DPA)	99%	Sigma-Aldrich Co., Ltd
Xylene	AR	Sigma-Aldrich Co., Ltd
NR	#1	Hainan Nature Rubber Co., Ltd.
NR latex	60 wt%	Hainan Nature Rubber Co., Ltd.
Carbon black	N234	Guoyao Company
Carbon black	N330	Guoyao Company
SiO_2		Guoyao Company
Graphite		Sigma-Aldrich Co., Ltd
Hydrazine hydrate	80wt%	Sigma-Aldrich Co., Ltd
Sulfuric acid	98wt%	Sigma-Aldrich Co., Ltd
$KMnO_4$	AR	Sigma-Aldrich Co., Ltd
$NaNO_3$	AR	Sigma-Aldrich Co., Ltd
HCl	36~38%	Sigma-Aldrich Co., Ltd
$NH_3 \cdot H_2O$	25 wt%	Sigma-Aldrich Co., Ltd
H_2O_2	30 wt%	Sigma-Aldrich Co., Ltd
C_6H_6	AR	Sigma-Aldrich Co., Ltd

Toluene	AR	Sigma-Aldrich Co., Ltd
Chlorobenzene	AR	Sigma-Aldrich Co., Ltd
Anhydrous calcium chloride	AR	Sigma-Aldrich Co., Ltd
ZnO		Sigma-Aldrich Co., Ltd
Stearic acid	SA	Sigma-Aldrich Co., Ltd
Wax		Guoyao Company
Sulfur		Guoyao Company
Phenylenediamine	4010NA	Guoyao Company
Dithiodibenzothiazole	DM	Guoyao Company
Zinc dimethyldithiocarbamate	ZDC	Guoyao Company
Benzothiazole sulfenamide	NS	Guoyao Company

3.2. Methods

3.2.1. Preparation of surface-functionalized carbon nanotubes

3.2.1.1. Acidification treatment of carbon nanotubes

The CNTs were sonicated in a mixed solution of sulfuric acid and nitric acid (V/V=3:1). Oxygen-containing functional groups were introduced at the port and defect sites of the carbon nanotubes.

The specific method is as follows: 1 g of pristine carbon nanotubes (MWCNTs-0) were placed in a mixed acid solution and ultrasonicated in a constant-temperature water bath for a certain period. The product was diluted ten times with deionized water and allowed to stand for approximately 12 h. After aging for 12 h, the supernatant was removed. The suspension was repeatedly washed with deionized water and suction-filtrered until the pH of the suspension became 7. The product was then vacuum-dried at 80°C for 12 h to produce acidified multiwalled carbon nanotubes (Modified-MWCNTs-1).

To investigate the effect of the amount of mixed acid solution and the oxidation time on surface modification, some experiments were conducted. First, the acidification effect on the CNTs was investigated by changing the amount of mixed acid solution used (60, 80, 120, 160, and 200 ml). Second, the acidification effect on the CNTs was

investigated by changing the reaction time (1, 2, 3, and 4 h).

3.2.1.2. Amination treatment of carbon nanotubes

Oxygen-containing functional groups on the surface of CNTs increase the hydrogen-bonding interactions between the CNTs. To reduce the surface energy of CNTs, eliminate the surface charge, improve their dispersability, and increase the binding strength at the interface with the substrate, the CNTs oxidized by mixed acid solution were reacted with diamines.

Modified-MWCNTs-1 prepared by the previous reaction were reacted with thionyl chloride ($SOCl_2$) via a two-step amination method. The specific method is as follows:

Modified-MWCNTs-1 (1 g) were placed in a mixed solution of $SOCl_2$ (60 ml) and DMF (3 ml) at a volume ratio of 20:1. The reaction product was washed with THF while heating at 70°C. The product was washed three to five times until the filtrate was clear, and the filter cake was vacuum-dried at 80°C for 12 h to obtain Modified-MWCNTs-2. The dry Modified-MWCNTs-2 were mixed with ethylenediamine and reacted in a constant-temperature oil bath. The reaction product was repeatedly washed with methylene chloride and ethanol for 3 to 5 times until the filtrate was clear, The filter cake was vacuum-dried at 80°C for 12 h to obtain aminated carbon nanotubes (Modified-MWCNTs-3)

The effects of different amounts of ethylenediamine and different reaction times on the surface modification of Modified-MWCNTs-2 were investigated. First, the amination of Modified-MWCNTs-2 was investigated by changing the amount of ethylenediamine used (36, 48, 60, 72, and 84 ml). Second, the amination of the carbon nanotubes was examined by changing the reaction time (12, 24, 48, and 72 h).

3.2.2. Preparation of surface-functionalized graphene

3.2.2.1. Alkylation of graphene

Graphite powder (30 mg) was added to 150 mL of DMF. After one hour of sonication, 200 mg of octadecylamine and 4.1 g of DCC were added to the solution. Then, the reaction proceeded at 90°C for 48 h under nitrogen as a protective gas. After the reaction was terminated, the reaction mixture was suction-filtered with a 0.22 μm pore size PTFE membrane. The filter cake was washed repeatedly with excess ethanol and dried in a vacuum oven at room temperature to obtain long-chain alkyl-grafted

graphene (Modified-Graphene-1).

A suspension of 5 mg of Modified-Graphene-1 was prepared by dispersion in 20 mL of xylene. The Modified-Graphene-1 suspension was suction-filtered with a PTFE filter (0.22 μm pore size, 47 mm diameter) to give a paper-like substance.

3.2.2.2. Polymer-modified GO

1) Preparation of alkyne-containing GO (Modified-GO-1) at the tail

GO (100 mg) was refluxed in 20 mL of thionyl chloride at 70°C for 24 h. After swirling to remove the thionyl chloride, the resulting solid was dried overnight in a vacuum oven at room temperature. Then, the product was slowly mixed with 3 mL of alcohol, 3 mL of purified chloroform and 1 mL of purified triethylamine at 0°C. After the reaction had proceeded in an ice-water bath for 1 h, stirring was continued for 24 h at room temperature. After the reaction was terminated, the reaction solution was filtered with a 0.22 μm pore size PTFE membrane. The filter cake was washed with ethanol four times and with deionized water twice and then dried in a vacuum oven at 35°C to obtain Modified-GO-1

2) Synthesis of azido-modified monodisperse polystyrene (N-PS)

AEBiB (an azide-bearing ATRP initiator, 45.4 mg), 27.61 mg of CuBr, 80 μl of PMDETA, 2 g of purified styrene and 2 g of purified chlorobenzene were mixed. After 3 "freeze-pump-thaw" cycles, the reaction was sealed and heated to 90°C for 8 h. The product was diluted with THF, and the catalyst was removed through a neutral alumina column. Next, the product was precipitated in methanol. The collected solid was dried in a vacuum oven at room temperature overnight to give N-PS. The gel permeation chromatography (GPC) results show that N-PS has a molecular weight of 4600 and an excellent monodispersity of 1.04.

3) Synthesis of azido-modified styrene-ethylene/butylene-styrene triblock copolymer (N-SEBS)

The synthesis of N-SEBS involves two steps: the chloromethylation of SEBS and the azidation of chloromethyl SEBS. SEBS is placed in an ice-water bath with the mixing of12 mL of trimethylchlorosilane and 2 mL of $SnCl_4$. The reaction proceeded at 0°C for 0.5 h and then was placed at room temperature for 6 h. Next, 50 mL of a mixed solvent of methanol/water was added to stop the reaction. The product CH_2Cl-SEBS was obtained by suction filtration, washed repeatedly with chloroform and then dried

in a vacuum oven overnight.

4) Preparation of monodisperse PS on GO (PS-GO)

Modified-GO-1 (20 mg), 200 mg of N-PS, 6.2 mg of CuBr, and 10 μL of PMDETA were dissolved in 15 mL of purified DMF. After 3 "freeze-pump-thaw" cycles, the flask was sealed and stirred at room temperature for 48 h. The product was washed with THF and isolated via filtration with a 0.22 μm pore size PTFE filter. The filter cake was washed with THF five times and dried in a vacuum oven overnight at room temperature to provide PS-GO.

5) Preparation of SEBS grafted onto GO (SEBS-GO)

Modified-GO-1 (40 mg) was mixed with 400 mg of N-SEBS. After 3 "freeze-pump-thaw" cycles, the reaction flask was sealed and reacted at room temperature for 24 h. After completion of the reaction, the reaction mixture was suction-filtered with a PTFE filter having a pore size of 0.22μm. The filter cake was washed with THF five times and dried in a vacuum oven at 40°C to obtain SEBS-GO.

3.2.2.3. Grafted polypropylene chain onto GO

1) Preparation of tail-end amino-containing GO (NH_2-GO)

GO (500 mg) was dispersed in 200 mL of THF by sonication. Then, 500 mg of diaminodiphenylmethane (MDA) was added. The mixture was heated to 80°C and refluxed for 6 h. After termination of the reaction, the reaction product was collected via suction filtration with a 0.22 μm pore size PTFE membrane. The filter cake was washed with ethanol four times and dried in a vacuum oven at room temperature to obtain NH_2-GO.

2) Preparation of PP grafted onto GO (PP-GO)

NH_2-GO (400 mg) was sonicated in 80 mL of xylene. Then, 800 mg of maleic anhydride-grafted polypropylene (MAPP) was added. The mixture was heated to 140°C and refluxed for 3 h. After the reaction was terminated, the reaction mixture was suction-filtered (using a 0.22 μm pore size PTFE filter). The filter cake was rinsed with toluene for 48 h and then dried in a vacuum oven at 90°C to obtain PP-GO.

3.2.3. Preparation of CNT/natural rubber composites

Table 3-2 Experimental formula of composites

Samples	CNT-0	CNT-1	CNT-3	CNT-5	CNT-7	CNT-9
Natural rubber	100	100	100	100	100	100
Modified-MWCNTs-3	0	1	3	5	7	9
Carbon black N234	25	22	16	10	4	0
Carbon black N330	20	20	20	20	20	20
Zinc oxide	5	5	5	5	5	5
Stearic acid	3	4	4	3	3	3
Si69	3.0	3.0	3.0	3.0	3.0	3.0
Sulfur	1.0	1.0	1.0	1.0	1.0	1.0

The formulations for the four carbon nanotube/natural rubber composites are shown in Table 3-2. The amidated carbon nanotubes (Modified-MWCNTs-3) used in this paper are easy to disperse. The functionalized carbon nanotubes are obtained according to the procedure described previously. CNT/natural rubber composites were prepared by mechanical blending. The vulcanization properties of the composites at 143°C were characterized by a rotorless rheometer. The rubber was vulcanized into rubber sheets with a thickness of 2 mm. The vulcanization temperature was 143°C, and the pressure was 15 MPa. The vulcanization time was the optimum curing time t_{90}.

3.2.4. Preparation of graphene/natural rubber composites

The graphene/natural rubber composite formulations are shown below in Table 3-3. Dry modified graphene, natural rubber, and other auxiliaries (shown above) were mechanically blended on a two-roll mill. The vulcanization properties of the mixtures at 143°C were characterized by a rotorless rheometer. The vulcanizates were vulcanized into rubber sheets with a thickness of 2 mm.

The curing temperature was 143°C, and the pressure was 15 MPa. The curing time was the optimum curing time t_{90}

Table 3-3 Experimental formula of composites

Samples	Graphene -0	Graphene-0.5	Graphene -1	Graphene -3	Graphene -5	Graphene -7	Graphene -9
Graphene	0	0.5	1	3	5	7	9
Natural rubber	100	100	100	100	100	100	100
ZnO	5	5	5	5	5	5	5
4010 NA	2	2	2	2	2	2	2
Wax	1	1	1	1	1	1	1
Stearic Acid	2	2	2	2	2	2	2
Sulfur	1.8	1.8	1.8	1.8	1.8	1.8	1.8

3.3. Characterization

3.3.1. Thermogravimetric analysis

Thermogravimetric analysis (TGA) of the samples was carried out by a TGA-DSC analyzer from Mettler-Toledo under N_2 protection. The temperature ranges were set from 50 to 600°C with a heating rate of 10°C/min.

3.3.2. Raman spectroscopy

A Renishaw inVia Reflex micro-Raman spectrometer was employed to obtain Raman spectra at an excitation wavelength of 514 nm.

3.3.3. Fourier transform infrared (FT-IR) spectroscopy

MWCNTs and KBr were ground into tablets, and spectra were obtained from a Nicolet-6700 FT-IR infrared spectrometer (Thermo Instruments, USA) with a resolution of 2 cm^{-1}. The test range was 4000 ~ 400 cm^{-1}.

Regarding the graphene and paper-like material of Modified-Graphene-1 (obtained by suction filtration), IR spectroscopic analysis was performed in total reflection mode.

IR test samples of GO, N-PS, PS-GO and SEBS-GO were prepared by KBr tableting and analyzed with a Nicolet-6700 FT-IR infrared spectrometer. After SEBS, CH2Cl-SEBS and N-SEBS were dissolved in THF, they were dripped onto KBr salt tablets and analyzed by IR spectroscopy.

3.3.4. Gel permeation chromatography (GPC)

The gel chromatography system used was produced by Waters Corporation of America.

3.3.5. Scanning electronic microscopy (SEM)

An ion-sputter source was used to spray gold on the tensile profile of the composite. The morphology of the composite was observed with a Quanta 450 scanning electron microscope (FEI) at an accelerating voltage of 5.0kV.

3.3.6. X-ray photoelectron spectroscopy (XPS)

XPS is a surface-sensitive quantitative spectroscopic technique that measures the elemental composition in the parts per thousand range, empirical formula, chemical state and electronic state of the elements that exist within a material. Examination of the binding energy of 1s allows identification of the chemical elements in the sample. In this paper, a PHI 5000 Versaprobe spectrometer was employed to qualitatively and quantitatively characterize the surface modification of the samples.

3.3.7. X-ray diffraction (XRD)

Characterization was performed on a PANalytical X'pert diffractometer (PANalytical, the Netherlands). Cu Ka (=0.154 nm) was employed as the radiation source, and the operating voltage and current are 40 kV and 40 mA, respectively.

3.3.8. Oxygenated functional groups on acidified CNTs

Boehm titration is commonly used to quantify oxygen-containing groups on the surface of solid carbon materials.

3.3.8.1. Preparation of NaOH standard solution

NaOH solution preparation: 0.521 g of NaOH was dissolved in 1000 mL of boiling deionized water in a volumetric flask; the resulting solution was called the standard solution.

Base potassium hydrogen phthalate pretreatment: 2 g of potassium hydrogen phthalate was placed in a vacuum oven at 105°C for 12 h. After drying, 3 parts of 0.013

g of potassium hydrogen phthalate were accurately weighed.

NaOH standard solution calibration: 0.013 g of potassium hydrogen phthalate was dissolved in 40 mL of boiled deionized water. Then, two drops of phenolphthalein were added as an indicator. The solution was titrated to a pink color with NaOH solution. The volume of the NaOH solution consumed was recorded, and this procedure was repeated twice. A blank experiment was conducted via the same method. With the equation listed below, the concentration of the NaOH standard solutions can be calculated.

$$c = \frac{m}{(v_1 - v_2) \times 0.2042}$$

Equation 3-1

c: Actual concentration of NaOH standard titration solution in mol/L;

m: mass of potassium hydrogen phthalate in g;

V_1: dose of NaOH standard titration solution in L;

V_2: dose of NaOH standard titration solution in the blank experiment in unit L;

0.2042: mass of potassium hydrogen phthalate in g equivalent to 1.00 mL of NaOH standard titration solution [$C_{(NaOH)}$=1 mol/L].

3.3.8.2. Preparation of HCl standard solution

Preparation of hydrochloric acid standard solution: 0.91 mL of 38% hydrochloric acid was added to a 1000 mL volumetric flask. Deionized water was added to the mark on the flask. After shaking, the resulting solution was called the standard solution.

Anhydrous sodium carbonate pretreatment: 1 g of anhydrous sodium carbonate was placed in a vacuum oven and dried under vacuum at 100°C for 12 h.

Hydrochloric acid standard solution calibration: 0.010 g of anhydrous sodium carbonate was dissolved in 40 mL of deionized water. A total of 3 drops of methyl orange was added as an indicator. The as-prepared solution was titrated with hydrochloric acid solution until the color turned orange-red. The volume of hydrochloric acid solution consumed was recorded, and this procedure was repeated twice. The same method was used to conduct the blank experiment. The concentration of the standard hydrochloric acid solution can be calculated with the following formula.

$$c = \frac{m}{(v_1 - v_2) \times 0.0530}$$

Equation 3-2

c: Actual concentration of the hydrochloric acid standard titration solution in mol/L;

m: mass of anhydrous sodium carbonate in g;

V_1: volume of hydrochloric acid standard titration solution in L;

V_2: dose of hydrochloric acid standard titration solution used in the reagent blank experiment in L;

0.0530: mass of reference anhydrous sodium carbonate in g equivalent to 1.00 mL of hydrochloric acid standard solution [$C_{(HCl)}$=1 mol/L].

3.3.8.3. Preparation of Na_2CO_3 standard solution

Anhydrous sodium carbonate was dried under vacuum at 100°C for 12 h. Anhydrous sodium carbonate (1.060 g) was dissolved in deionized water in a 1000 mL volumetric flask. The concentration of the as-prepared Na_2CO_3 solution is 0.01 mol/L.

3.3.8.4. Preparation of $NaHCO_3$ standard solution

Preparation of $NaHCO_3$ solution: 0.860 g of dried sodium bicarbonate was dissolved with an appropriate amount of deionized water in a 1000 mL volumetric flask.

Calibration of the $NaHCO_3$ solution: 10 mL of $NaHCO_3$ solution was titrated by calibrated HCl solution with one drop of methyl orange as an indicator. The volume of HCl solution consumed was recorded. The procedure mentioned above was repeated twice. From the formula below, the concentration of the $NaHCO_3$ standard solution can be calculated.

$$c = c_1 v_1 / v$$

Equation 3-3

c: Concentration of $NaHCO_3$ solution in mol/L;

c_2: Concentration of HCl solution in mol/L;

v_1: volume of HCl solution in mL;

v: volume of $NaHCO_3$ liquid in mL.

3.3.9. Oxygenated functional groups on acidified CNTs

Boehm pointed out that NaOH solution can react with all acidic groups on the surface of MWCNTs, including carboxyl groups, carbonyl groups and hydroxyl groups. Na_2CO_3 solution can react with carboxyl groups and hydroxyl group, while $NaHCO_3$ solution can react only with carboxyl groups. Therefore, the content of oxygen-containing functional groups on the surface of MWCNTs can be determined by dissolving the Modified-MWCNTs-1 in excess NaOH solution, Na_2CO_3 solution and $NaHCO_3$ solution, respectively. Then, hydrochloric acid (HCl) was used to titrate the amount of the corresponding substance left.

Modified MWCNTs (0.100 g) prepared with different mixed acid doses and acidification times were placed in a 100 mL beaker. A certain amount of NaOH solution, Na_2CO_3 solution or $NaHCO_3$ solution was added to formulate mixed solutions. The as-prepared solution was reacted for 24 h. The volume of HCl solution needed to titrate the solution to pH=7.00, pH=3.89 and pH=3.89, respectively, was recorded.

3.3.10. Vulcanization characteristics

The vulcanization characteristics of samples were determined by a rotorless vulcanizer to obtain an optimum cure time t_{90} at 143°C.

3.3.11. Mechanical behavior

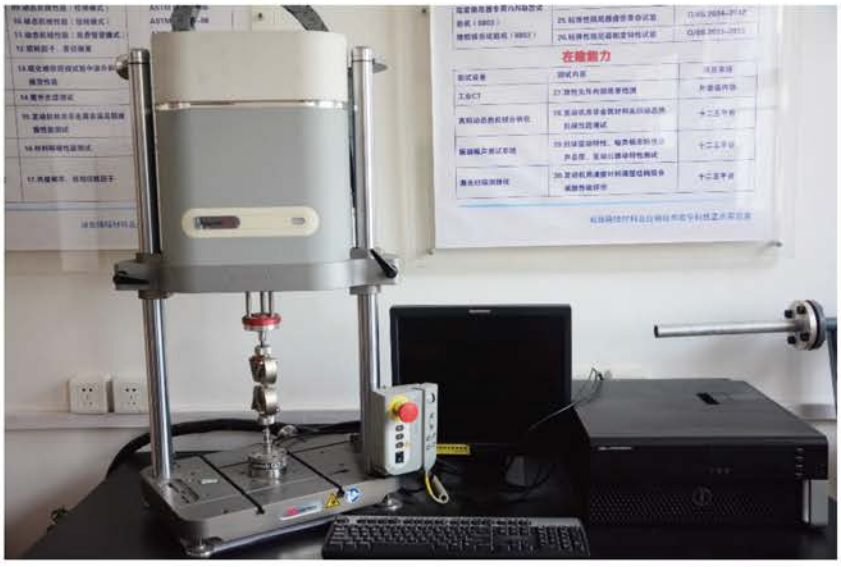

Figure 3-1 Universal testing machine

Figure 3-2 Dynamic fatigue testing machine

The mechanical properties of rubber were tested with a universal testing machine based on testing standards ISO 37:2011 and ISO 34-1: 2010. Additionally, the Shore A hardness of samples was tested via the standard ISO 868: 2003.

3.3.12. Rubber processing analysis

Figure 3-3 Rubber processing analysis RPA2000

The composite material shear storage modulus and strain amplitude relationship was determined by an Alpha Technologies RPA2000 rubber processing analyzer (USA). The rubber mixture was first placed on a sample stage of the RPA2000 for vulcanization at a temperature of 143°C for a time of t_{90}. The temperature was then decreased to 60°C.

3.3.13. Dynamic mechanical thermal analysis

The dynamic thermomechanical properties of the composites in tensile mode were characterized by a dynamic mechanical thermal analyzer (DMTA) manufactured by Metravib Company. The sample size was 15×15×2 mm, the temperature range was -80 to 40°C, the dynamic strain amplitude was 0.1%, and the frequency was 5 Hz.

Figure 3-4 Dynamic mechanical thermal analyzer

3.3.14. J-integral test

3.3.14.1. J-integral calculation for single-notch tensile specimens (SNTSs)

$$J = -(\partial U|\partial A)_{\Delta} = -\frac{1}{B}(\partial U|\partial a)_{\Delta}$$

Equation 3-4

For the natural rubber composites, we used single-notch tensile specimens (SNTSs) to conduct the J-integral test. The width W of the SNTSs with different crack lengths was 15 mm. A sharp blade was used to cut cracks of different lengths in the middle of one side of the specimen. The lengths of the cracks ranged from 1 mm to 12 mm with 1 mm intervals. The stretching rate was 20 mm/min. The tensile curves of SNTSs with precut cracks of different lengths were obtained. The function of the strain energy "U" and the

precut length "a" under a fixed displacement was obtained through calculation. The relationship between "U" and "a" under a fixed displacement is exhibited in Figure 3-5. A quadratic function and a linear function were used to fit the relationship between the strain energy and the precut length. Notably, R^2 is significantly greater for the linear function than for the quadratic function.

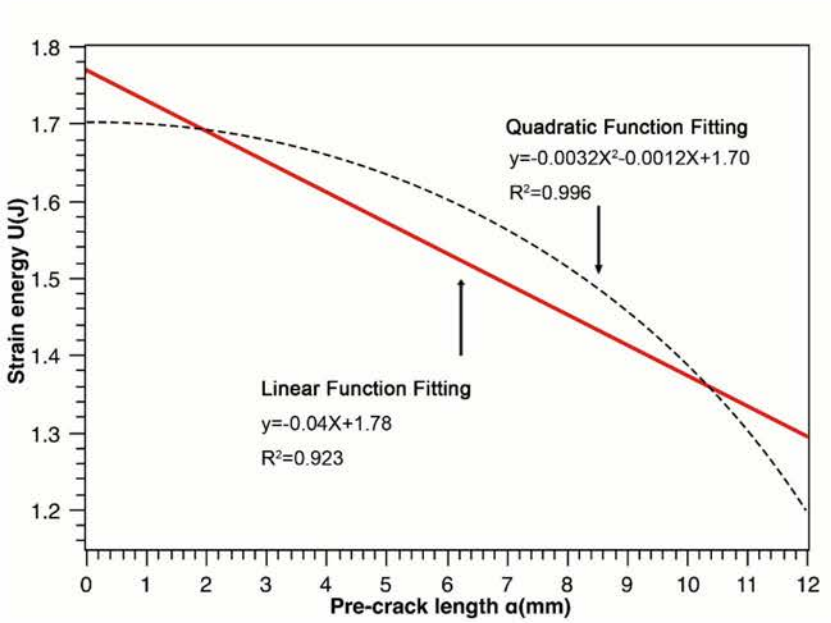

Figure 3-5 Strain energy vs. crack length

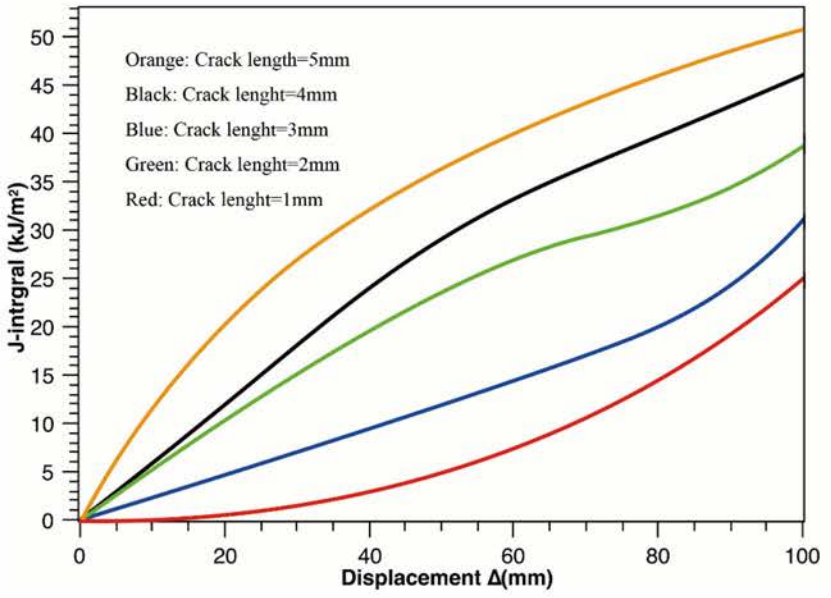

Figure 3-6 Function of displacement

Therefore, in this study, we used a quadratic function to fit and calculate the J-

integral according to the above equations. The J-integrals calculated under different displacements are shown in the Figure 3-6. For SNTSs under a constant displacement, the J-integral value increases as "a" increases.

3.3.14.2. J-integral calculation on pure shear specimens (PSSs)

For the composites prepared in the experiment, we also performed J-integral tests on the pure shear specimens (PSSs). The cut sample had a length of 40 mm, a width of 10 mm and a thickness of 2 mm. The cut length was approximately 3-24 mm. The details of the J-point calculation are described above. In short, after removing the Mullins effect on the sample, a sharp blade is used to cut different length cracks in the middle of the samples. The stress-strain curves of specimens with different precut lengths were recorded at a stretching rate of 3 mm/min. The J-integral value is calculated according to the above equation. The "U" and "a" of the shear specimen show a strictly linear relationship, as shown in Figure 3-7. Therefore, for PSSs, the J-integral at a constant strain is independent of the crack length "a".

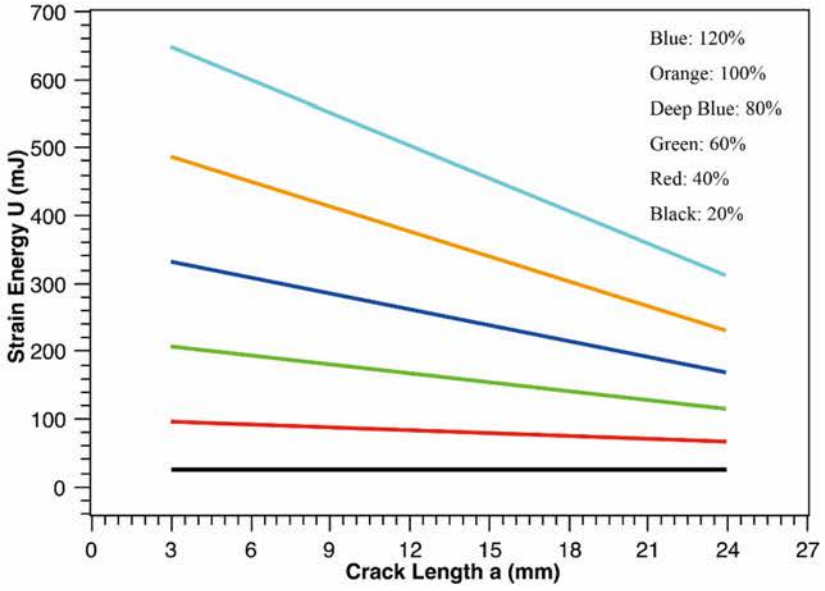

Figure 3-7 Linear relation between the strain energy and precut length

3.3.14.3. Critical J-integral J_{IC} and tear modulus T_R

In this study, the crack-tip opening displacement (CTOD) was used as the starting point of the crack tip, and the J-integral at the CTOD was used as the critical J-integral J_{IC} to characterize crack initiation behavior. During the test, the critical displacement corresponding to CTOD=0.1 mm can be determined. In addition, the corresponding J_{IC}

value can be determined. The tear modulus T_R, which characterizes crack resistance, was calculated according to the following equation

$$T_R = \frac{dJ}{dCTOD}\Big|CTOD \in [0.1mm, 0.5mm]$$

Equation 3-5

To observe crack initiation and crack propagation more easily, the sample was spread over a uniform layer of silver powder. A digital camera was used to observe the size of the CTOD over time. Photoshop software was used to measure the exact value of the CTOD. The curves of the ratio of the J-integral to the CTOD for different precut length samples were obtained. In addition, the corresponding T_R values were obtained.

3.3.15. Dynamic fatigue crack propagation test

3.3.15.1. Dynamic fatigue testing on SNTSs

Figure 3-8 Dynamic and fatigue testing systems

For the composites prepared in this study, a dynamic fatigue test was performed on SNTSs with a precut length of 1 mm. Before cutting composite coupons, the specimens were prefatigued 2000 times to eliminate the Mullins effect and residual deformation.

The specimens were subjected to fatigue testing under constant strain conditions on an 8802 dynamic and fatigue testing system manufactured by INSTRON Co., Ltd. The test strain was 30%-100% with a sine wave at a frequency of 5 Hz at room temperature.

3.3.15.2. Dynamic fatigue testing on PSS

For the composites prepared in this study, we prepared shear specimens for fatigue testing. The PSSs had a length of 40 mm, a width of 10 mm and a thickness of 2 mm. The precut length was 3 mm. The test was performed using a DMA+450 dynamic fatigue tester manufactured in France with a frequency of 20 Hz with a sine wave at a temperature of 23°C. The fatigue crack growth rate, da/dN, was tested under different tearing energies (500, 1000, 1500 and 2000 J/m^2). The specimen should be damaged prior to the test. Then, the constant tearing energy was determined with the corresponding constant strain. To find da/dN, the length of the crack was observed by a microscope fitted to a fatigue tester after the sample underwent the fatigue cycle N times.

3.3.16. Strain energy density (SED) and hysteresis energy density (HED)

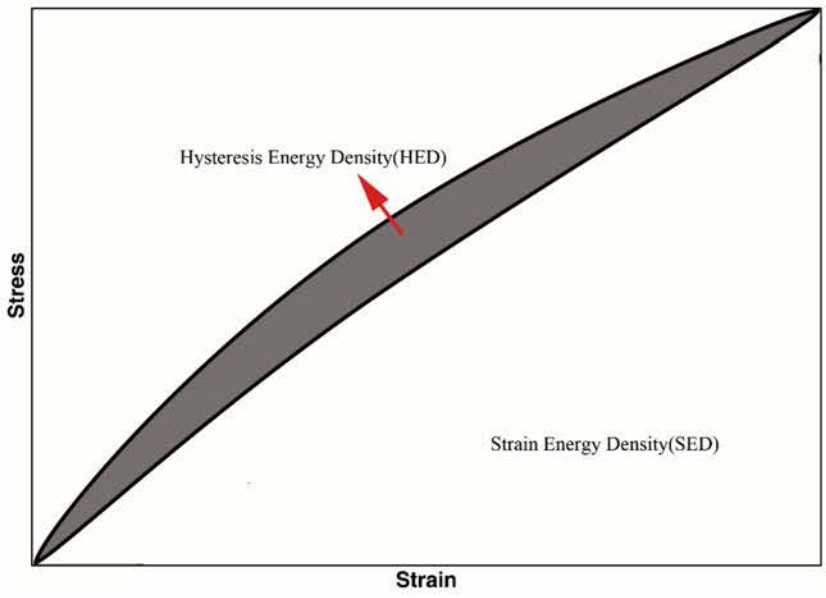

Figure 3-9 SED and HED schematics

Figure 3-9 shows a cyclic stress-strain curve. A sample without a precut crack was used for our testing. As shown in the figure, the strain energy density (SED) is calculated from the integrated area below the recovery curve of the fifth cycle to exclude the Mullins effect. Then, we can see the hysteresis energy density (HED), which is a

parameter that characterizes the energy dissipated during cyclic deformation. In addition, the HED was obtained by measuring the hysteresis loop. The hysteresis loss H (%) at a given strain is the percentage of the HED over the total area of the integral.

Chapter 4. Composites of Natural Rubber and Carbon Nanotubes

4.1. Introduction

Carbon nanotubes (CNTs) have excellent mechanical properties, electrical properties, thermal conductivity and optical properties, making them a very attractive prospect in the field of high-performance composites. However, CNTs are highly polarized and have a smooth surface. There are strong van der Waals forces between CNT particles; thus, CNTs are prone to agglomeration, which often leads to the formation of bundles of dozens or even hundreds of nanotubes. As a result, the applications of CNTs are limited [65, 79, 190]. The purpose of using CNTs as a filler to enhance composites is ensure the effective dispersion of the CNTs. However, CNTs tend to agglomerate. Due to the lack of active groups on their surface, CNTs are hardly soluble in water. Their poor solubility limits the commercialization of CNTs despite their superior physical and chemical properties. If CNTs used as a reinforcing filler can be uniformly dispersed in the natural rubber and form good interfacial compatibility with the natural rubber matrix, then the mechanical properties and thermal conductivity of composites can be effectively improved.

At the same time, the surface of CNTs is highly nonpolar, making them insoluble in all solvents and polymers [80, 119]. Therefore, to improve the dispersibility of CNTs in rubber matrices and enhance the interfacial compatibility between CNTs and rubber matrices, improving the surface activity of CNTs by grafting functional groups onto their surface is necessary. Recently, many studies on functionalization of CNTs have focused on the macroscopic properties of polymers. Additionally, many studies have confirmed that grafting organic functional groups onto the surface of CNTs can effectively functionalize CNTs. Functionalization results in a reduction in the surface energy of the CNTs, which prevents aggregation and improves their dispersibility performance in matrices. Thus, the interfacial adhesion between CNTs and polymers can be enhanced. To establish a good binding force between the CNTs and the natural rubber matrix, the CNTs were modified with reactive amine groups. The specific research ideas are listed below:

The diamine-grafted CNTs can react with the active groups in natural rubber, which

effectively enhances the compatibility between the CNTs and the rubber matrix. Based on this idea, this chapter first explores the acidification process of CNTs and determines the optimal acidification conditions. Next, the structure and properties of amine-functionalized CNTs are investigated.

Regarding the type of rubber, the first consideration should be whether it induces crystallization under external deformation. For example, shape factor, surface activity, dispersion morphology and interfacial strength all play important roles in the failure behavior of composites [191].

However, current research mainly focuses on improving various properties of rubber simply by filling rubber matrices with CNTs. Different kinds of filler systems, such as CNTs and carbon blacks (CBs), have also attracted attention. The combination of CNTs and nano-CB has been found to have a synergistic effect on the mechanical properties and thermal conductivity of composites.

The dynamic crack propagation behavior of rubber composites has received little attention. Therefore, this chapter will focus on the failure behaviors of rubber composites under dynamic conditions [2, 192].

This chapter also focuses on the effect of functionalized CNTs and CB filler networks on the mechanical properties of rubber matrix. In addition, the dynamic crack propagation behavior of natural rubber composites were explored. Rubber composites were prepared by mechanical blending. The crack initiation behavior and crack propagation behavior of the composites were characterized by the J-integral test. We use J_{IC} and T_R to determine the propagation behavior. Moreover, the crack growth rate and fatigue lifetime under different strains were obtained. A synergistic effect between the CNTs and CB that compose the filler network was found; this effect considerably influences the mechanical properties and crack propagation resistance of composites.

4.2. Results and discussion

4.2.1. Functionalization of carbon nanotubes

First, the surface of CNTs was grafted with oxygen-containing functional group by a mixed acid oxidation process. The Modified-MWCNTs-1 were reacted with $SOCl_2$ in dimethylformamide (DMF), and the product is called Modified-MWCNTs-2. Then, Modified-MWCNTs-3 were prepared via the reaction of the easily substituted chlorine

atoms with amine groups by placing Modified-MWCNTs-2 in ethylenediamine. A schematic diagram of the reaction process is shown in Figure 4-1.

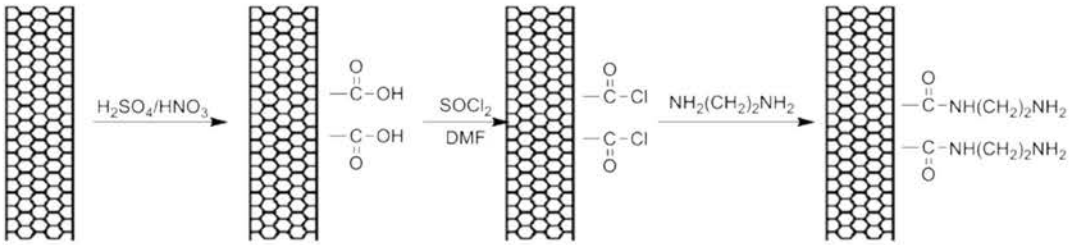

Figure 4-1 Scheme for the preparation of amine-functionalized MWCNTs

A variety of characterization techniques are used to investigate the morphology and structure of functionalized CNTs before and after the modification process. Additionally, the modification grafting efficiency is evaluated to determine the best modification conditions for the preparation of high-performance CNT/rubber composites.

4.2.1.1. Reaction parameters for the acidification of carbon nanotubes

1) Effect of mixed acid dose on the structure of carbon nanotubes

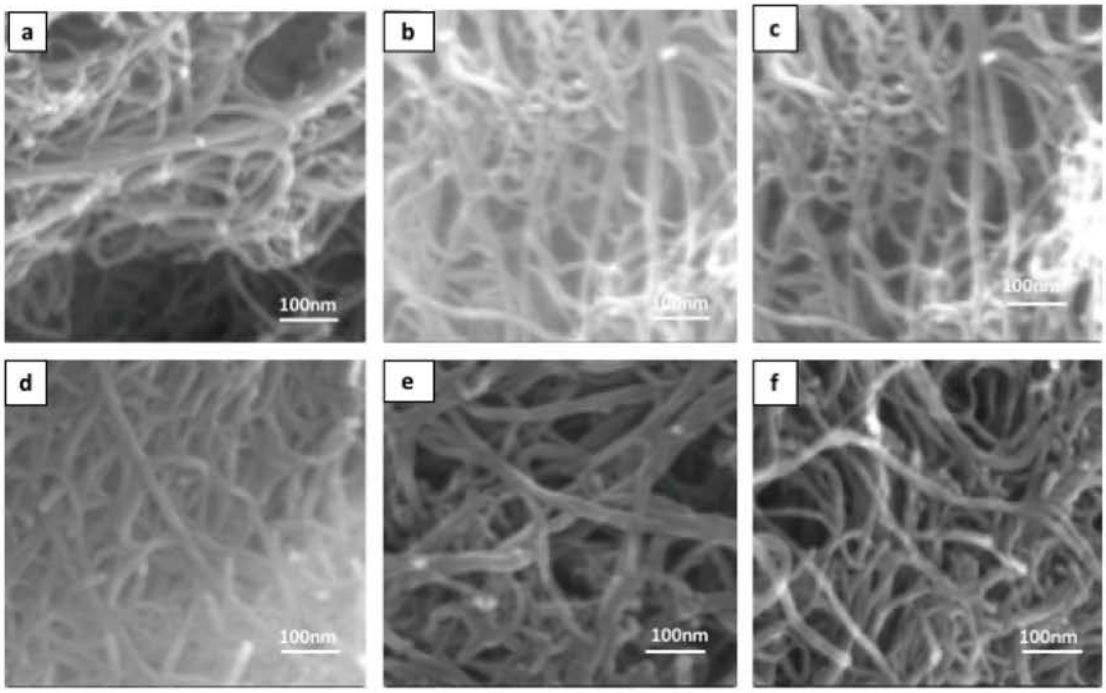

Figure 4-2 (a) MWCNTs treated at 50°C for 2 h with different amounts of mixed acid: (b) 60 mL, (c) 80 mL, (d) 120 mL, (e) 160 mL, and (f) 200 mL.

Figure 4-2 shows SEM images of MWCNTs-0 and Modified-MWCNTs-1 obtained

after mixed acid treatment with various volumes of mixed acid at 50°C for 2 h. The multiwalled carbon nanotubes (MWCNTs) show an irregular winding state, demonstrating there was no adhesion and no agglomeration between the MWCNTs.

When the amount of mixed acid was 60 mL, the MWCNTs were uneven in thickness and irregular in winding state. Figure 4-2 c and d show that when the mixed acid amount is 80 mL and 120 mL, the MWCNTs have a uniform thickness and good dispersibility. Importantly, in these figures, some of the MWCNTs are cut off, and many short tubes appear, which greatly reduced the degree of MWCNT entanglement and improved the dispersibility of the MWCNTs in solution. When the volume of the mixed acid solution increased to 160 mL and 200 mL, most of the MWCNTs became thinner, and the dispersion of the MWCNTs worsened, indicating that the structure of the MWCNTs was greatly damaged. Therefore, when the amount of mixed acid is 80 mL and 120 mL, the MWCNTs can be effectively reduced, and the dispersion of the MWCNTs can be improved.

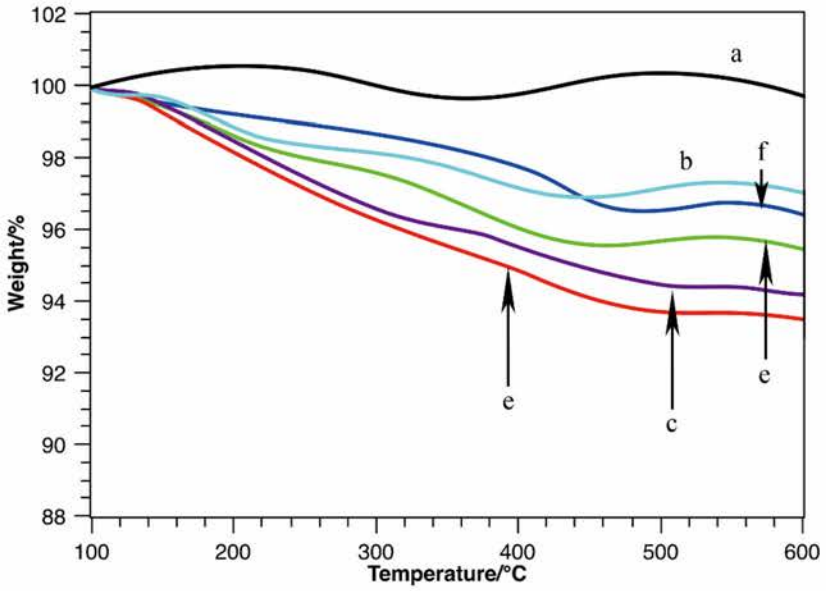

Figure 4-3 TGA curves of MWCNTs. (a) MWCNTs-0 and MWCNTs treated with different volumes of mixed acid at 50°C for 2 h: (b) 60 mL, (c) 80 mL, (d) 120 mL, (e) 160 mL, and (f)200 mL.

Thermogravimetric analysis (TGA) was performed before and after modification to confirm the effect of the mixed acid dose on the modification of the MWCNTs. Figure 4-3 shows the TGA curves of MWCNTs-0 and Modified-MWCNTs-1 treated with 60, 80, 120, 160 and 200 mL of mixed acid at 50°C for 2 h. All the TGA tests were

conducted under an inert atmosphere at a heating rate of 10°C/min. From the curves, it can be seen that under an inert atmosphere, MWCNTs-0 hardly decompose during TGA. Regarding all the MWCNT samples modified by acidification, obvious weight losses appear. The weight loss comes from the decomposition of oxygen-containing functional groups grafted onto the surface of the MWCNTs. Curve b shows that when the volume of mixed acid used is 60 mL, the weight loss rate of the MWCNTs is the lowest. Combined with the SEM images, the TGA results reveal that when the amount of mixed acid is too small, fewer oxygen-containing functional groups are grafted onto the surface of the MWCNTs, and there is less damage to the MWCNTs. Thus, the weight loss rate is also small. When the mixed acid dose is 80 mL or 120 mL (see curves c and d), the weight loss rate of the MWCNTs obviously increases. In addition, the initial weight loss temperature moves to a lower temperature. The weight loss rate also increases as the content of oxygen groups introduced on the surface of the MWCNTs increases. With increasing mixed acid dose, the weight loss rate tends to decrease. Moreover, the SEM images show when too much mixed acid is used, a large adhesion area between the MWCNTs appears, indicating that too many oxygen-containing functional groups were grafted onto the surface of the MWCNTs because of the excess acid. On the other hand, excessive etching will remove some reactive carbon. This loss of reactive carbon causes the remaining carbon structure to be extremely stable, which makes it difficult for the structure to lose weight during TGA analysis.

To quantitatively analyze the effect of different mixed acid doses on the modification of MWCNTs, acid-base titration was used to characterize the samples. The results are shown in below in Table 4-1. It can be seen that as the volume of mixed acid increases, the total content of oxygen-containing functional groups on the MWCNT surface first increases and then decreases, which is consistent with the TGA results. When the 80 mL of mixed acid is used, the total content of oxygen-containing functional groups on the MWCNT surface is 1.416×10^{-3} mol/g. The reason is that, as the volume of mixed acid increases, the oxidation capacity is enhanced. Thus, at the same oxidation time, more of the dangling bonds (unsaturated carbon atoms) on the surface of MWCNTs are oxidized to -COOH. The number of -C=O and -C-OH groups also increases. Overall, the total content of oxygen-containing functional groups increased. The following table also shows that when the mixed acid dose is 80 mL, the MWCNT surface carboxyl content is the largest, which is 5.260×10^{-4} mol/g.

Table 4-1 Results for Modified-MWCNTs-1 treated with different mixed acid volumes

Volume of mixed acid/mL	60	80	120	160	200
Total acidic groups (mol/g)	1.132×10^{-3}	1.416×10^{-3}	$1.411\ 1\times10^{-3}$	1.374×10^{-3}	1.281×10^{-3}
Carboxyl groups (mol/g)	4.002×10^{-4}	5.150×10^{-4}	4.962×10^{-4}	4.583×10^{-4}	4.044×10^{-4}

The combination of the SEM images, TGA curves and acid-base titration results indicate that when the volume of mixed acid is 80 mL or 120 mL, the MWCNTs show good dispersibility, a small degree of entanglement, a large weight loss rate and an increased content of oxygen-containing functional groups. From economic and environmental points of view, the final choice for the optimal mixed acid dose is 80 mL.

2) Effect of mixed acid treatment time on the composition and structure of carbon nanotubes

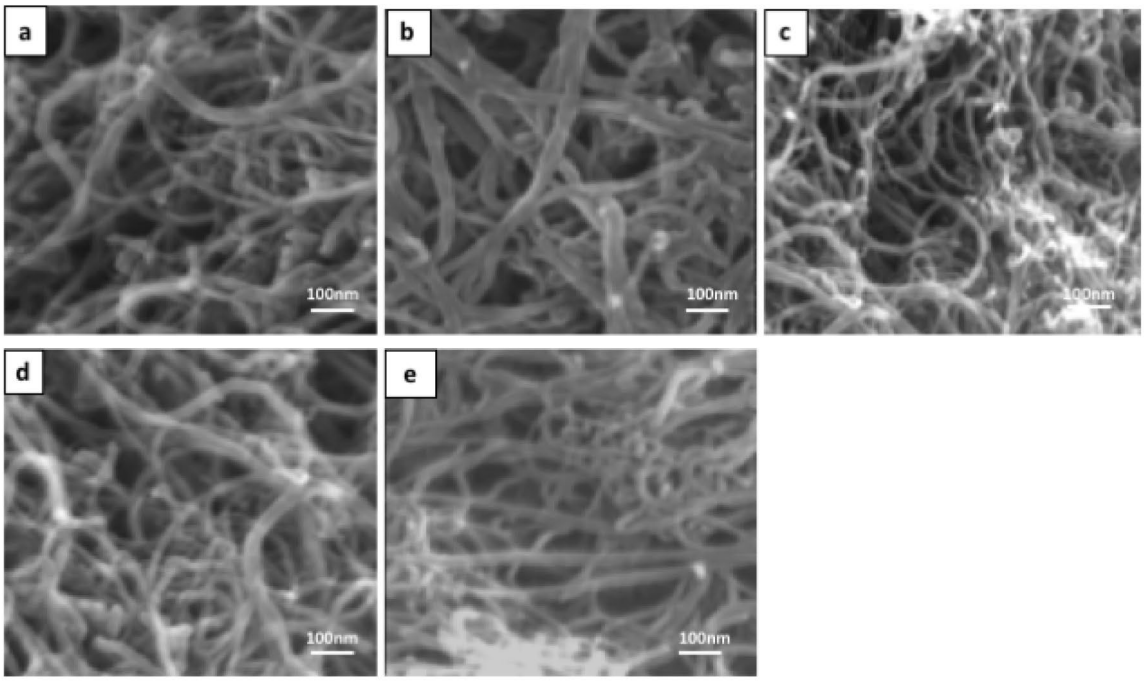

Figure 4-4 SEM images of MWCNTs: (a) MWCNTs treated at 50°C with 80 mL of mixed acid for (b) 1 h, (c) 2 h, (d) 3 h and (e) 4 h.

The SEM images in Figure 4-4 are images of MWCNTs-0 and Modified-MWCNTs-1 treated for 1, 2, 3 and 4 h with 80 mL of mixed acid at 50°C. Figure 4-4 shows that the MWCNTs are not uniform in thickness and that there is no obvious

change in the degree of entanglement when the acidification time is 1 h. This result indicates that when the acidification time is too short, the damage to the structure of MWCNTs is minor, and the degree of acidification is not uniform.

Figure 4-4 c shows that MWCNTs prepared with an acidification time of 2 h have a uniform thickness and good dispersion. In addition, some of the MWCNTs are truncated, and many short tubes appear. The degree of wrapping of the MWCNTs is also greatly reduced. This change is conducive to improving the dispersion of the MWCNTs in solution or in a polymer. With further prolongation of the acidification time to 3 h and 4 h, serious agglomeration and agglomeration, respectively, appear. The structure of the MWCNTs was severely damaged, and many broken and thin tubes appeared. In addition, their dispersion became worse. To further evaluate the effect of acidification time, the MWCNTs modified for different acidification times were characterized by TGA.

Figure 4-5 shows TGA curves for MWCNTs-0 and Modified-MWCNTs-1 obtained after 1, 2, 3 and 4 h of treatment with 80 mL of mixed acid at 50°C under an inert atmosphere. It can be concluded that the MWCNTs obtained after different acidification times show obvious weight loss under an inert atmosphere. In addition, the weight loss comes from the decomposition of the oxygen-containing functional groups grafted onto the MWCNT surface.

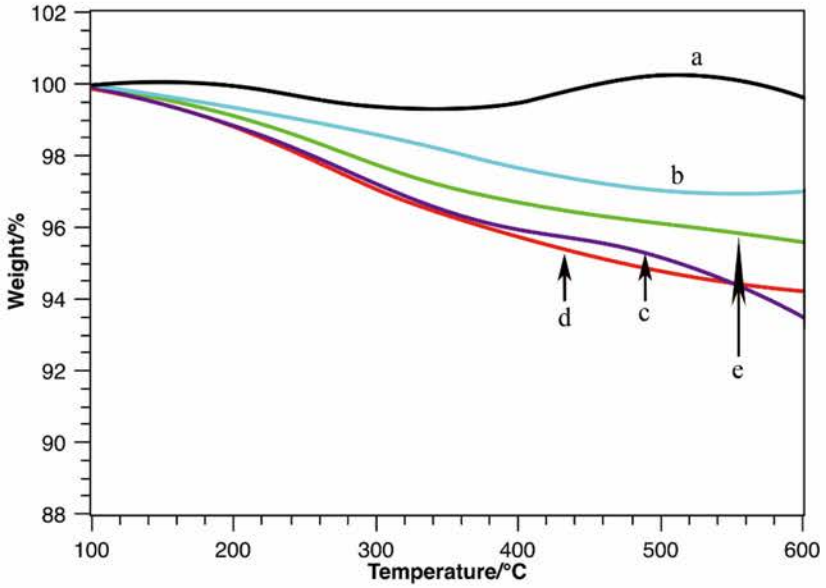

Figure 4-5 TGA curve of MWCNTs: (a) MWCNTs treated at 50°C with 80 mL of mixed acid solution for (b) 1 h, (c) 2 h, (d) 3 h and (e) 4 h.

Curve b shows that the weight loss rate of the MWCNTs with the acidification time of 1 h is the lowest. Combined with the SEM images, these results reveal that when the acidification time is too short, the weight loss rate is small, indicating that the surface of the MWCNTs have fewer oxygen-containing functional groups. In curves c and d, compared with that of the MWCNTs treated for 1 h, the weight loss rate of the MWCNTs prepared with acidification times of 2 h and 3 h increased obviously. Combined with the SEM images, the TGA suggest that the surface of these MWCNTs was grafted with more oxygen-containing functional groups. In addition, their structure was destroyed to a certain extent as the rate weight loss increases. Regarding the 3 h acidification time sample, although there was significant weight loss, the MWCNT surface was still grafted with a certain content of oxygen-containing functional groups. However, the SEM images of these MWCNTs showed that they were aggregated. In addition, the weight loss rate decreased with increasing mixed acid treatment time. The longer the mixed acid treatment time was, the greater the adhesion between the MWCNTs. Furthermore, the thickness of the MWCNTs became small and uniform, indicating that the acidification treatment time is too long. This resulted in serious damage to the structure of the MWCNTs themselves, increasing the content of surface hydrogen bonds, decreasing the weight loss rate and making their dispersion uneven.

Table 4-2 Results for Modified-MWCNTs-1 treated for different times

Reaction time/h	1	2	3	4
Total acidic groups (mol/g)	7.713×10^{-4}	1.416×10^{-3}	1.224×10^{-3}	9.117×10^{-4}
Carboxyl groups (mol/g)	2.054×10^{-4}	5.150×10^{-4}	3.493×10^{-4}	2.151×10^{-4}

From Curve b shows that the weight loss rate of the MWCNTs with the acidification time of 1 h is the lowest. Combined with the SEM images, these results reveal that when the acidification time is too short, the weight loss rate is small, indicating that the surface of the MWCNTs have fewer oxygen-containing functional groups. In curves c and d, compared with that of the MWCNTs treated for 1 h, the weight loss rate of the MWCNTs prepared with acidification times of 2 h and 3 h increased obviously. Combined with the SEM images, the TGA suggest that the surface of these MWCNTs was grafted with more oxygen-containing functional groups. In addition, their structure was destroyed to a certain extent as the rate weight loss increases. Regarding the 3 h acidification time sample, although there was significant

weight loss, the MWCNT surface was still grafted with a certain content of oxygen-containing functional groups. However, the SEM images of these MWCNTs showed that they were aggregated. In addition, the weight loss rate decreased with increasing mixed acid treatment time. The longer the mixed acid treatment time was, the greater the adhesion between the MWCNTs. Furthermore, the thickness of the MWCNTs became small and uniform, indicating that the acidification treatment time is too long. This resulted in serious damage to the structure of the MWCNTs themselves, increasing the content of surface hydrogen bonds, decreasing the weight loss rate and making their dispersion uneven.

Table 4-2 above, it can be seen that with increasing acidification time, the total content of oxygen-containing functional groups first increases and then decreases. In addition, the carboxyl group content also increases first and then decreases. When the acidification time is only 1 h, the total content of acid groups in the Modified-MWCNTs-1 is the lowest, which is 7.713×10^{-4} mol/g. This is because the reaction between the mixed acid and MWCNTs is incomplete when the acidification time is short. When the acidification time is 2 h, the MWCNTs are oxidized by the mixed acid, and the content of oxygen-containing functional groups on the surface of the MWCNTs increases to 1.416×10^{-3}mol/g. The MWCNTs are overoxidized as the acidification time is increased further. The structure of MWCNTs is destroyed, leading to the detachment of the oxygen-containing functional groups introduced onto the surface of the MWCNTs. This detachment resulted in a lower content of acidic groups. When the acidification time is 2 h, the content of carboxyl groups on the surface of the MWCNTs is the largest, which is 5.50×10^{-4} mol/g. The combination of the SEM images, TGA curves and acid-base titration results indicates that when the acidification time is 2 h, the MWCNTs have good dispersity, a small degree of entanglement, a high weight loss rate, and an increase content of surface acidic oxygen-containing functional groups is more. Therefore, 2 h of acidification is considered the most suitable treatment time.

Through analysis of the volume of mixed acid and the acidification time, the following optimized acidification conditions of MWCNTs were obtained: 1 g of MWCNTs were dispersed in 80 mL of mixed acid solution for a reaction time of 2 h at a reaction temperature of 50°C. The obtained Modified-MWCNTs-1 have good dispersibility, a low degree of entanglement, a high grafting rate and abundant surface acidic oxygen-containing functional groups.

4.2.1.2. Reaction parameters for the amination of carbon nanotubes

1) Effect of ethylenediamine dose on the composition and structure of carbon nanotubes

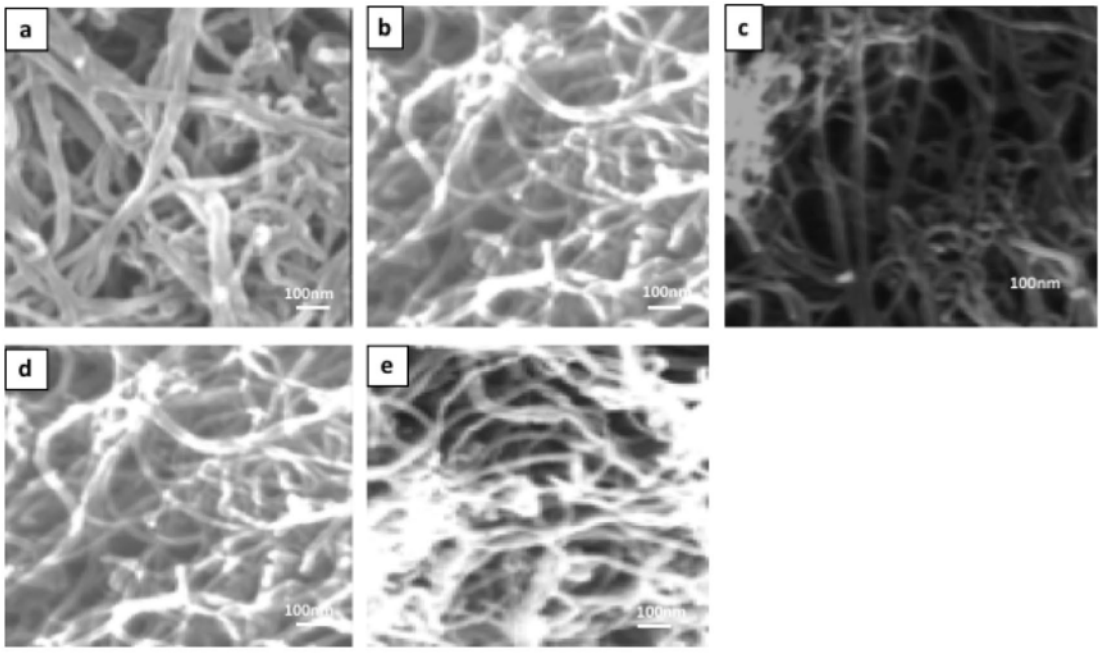

Figure 4-6 SEM images of Modified-MWCNTs-3 treated with different content of ethylenediamine: (a)36 mL (b)48 mL (c)60 mL (d)72 mL and (e)84 mL at 100°C and 48 h.

Figure 4-6 shows the SEM images of Modified-MWCNTs-3 obtained after the reaction of 0.3 g of Modified-MWCNTs-2 with various doses of ethylenediamine at a constant temperature of 100°C for 48 h. As shown in Figure 4-6 a, the Modified-MWCNTs-3 disperse poorly when the volume of ethylenediamine is 36 mL. The poor dispersion is because when the amount of ethylenediamine is small, the chloride groups grafted onto the surface of the Modified-MWCNTs-3 are not completely replaced. Thus, the polar electrostatic effect still exists, resulting in the agglomeration of Modified-MWCNTs-3. As the volume of ethylenediamine increases, the weight of the Modified-MWCNTs-3 obtained remained uniform. In addition, compared with the Modified-MWCNTs-1, the Modified-MWCNTs-3 were loosely packed, indicating that the Modified-MWCNTs-3 were less bonded and entangled. They also redispersed well in solution.

With increasing ethylenediamine volume, more of the chloride groups grafted onto the surface of Modified-MWCNTs-3 were consumed, thereby reducing the electrostatic

attraction between the Modified-MWCNTs-3. On the other hand, due to the steric hindrance effect of ethylenediamine, the gap between the CNTs enlarges in the Modified-MWCNTs-3, causing the Modified-MWCNTs-3 to show loose accumulation and reduced adhesion. When the volume of ethylenediamine was increased to 84 mL (see Figure e), the dispersibility of the Modified-MWCNTs-3 became worse. In addition, a large amount of sticking and entanglement occurred due to the increased hydrogen bonding with the terminal amino groups resulting from the excess amount of ethylenediamine used. This leads to reappearance of adhesion between Modified-MWCNTs-3. Graphs c and d show that the optimal volumes of ethylenediamine are 60 mL and 72 mL.

To further determine the effect of the volume of ethylenediamine on the amination reaction, SEM analysis and Fourier transform infrared (FT-IR) spectroscopy were used to characterize the Modified-MWCNTs-3 prepared with different amounts of ethylenediamine.

Figure 4-7 shows the IR spectra of Modified-MWCNTs-3 treated with different amounts of ethylenediamine. It can be seen that the characteristic amide absorption appeared at 1637 cm^{-1}. Curve d shows that when the amount of ethylenediamine is 72 mL, the absorption peak of the CN bond in amides appeared obviously at 1070 cm^{-1}. The bending and stretching vibrational peaks of CH bonds appeared between 2800 and 3000 cm^{-1}, while the -COOH absorption peak at 1730 cm^{-1} disappeared. Considering the changes in these peaks, we can conclude that when 72 mL of ethylenediamine is used to treat the MWCNTs, many amine groups linked through an amide bond form on the surface of the MWCNTs.

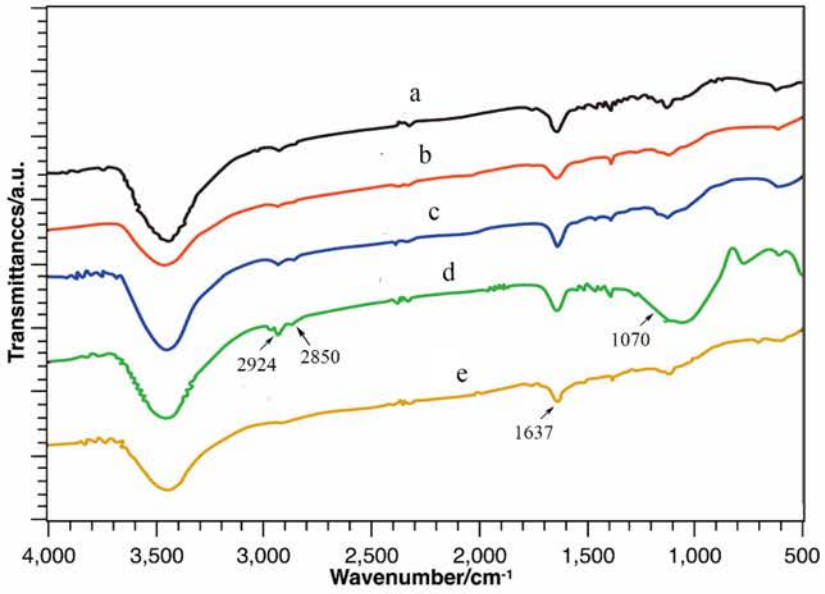

Figure 4-7 FT-IR spectra of Modified-MWCNTs-3 treated with different volumes of ethylenediamine at 100°C for 48 h : (a) 36 mL, (b) 48 mL, (c) 60 mL, (d) 72 mL and (e) 84 mL.

The SEM and FT-IR characterization results led to the selection of 72 mL as the amount of ethylenediamine to use in the optimized amination reaction

2) Effect of ethylenediamine treatment time on the composition and structure of carbon nanotubes

Considering that the different reaction times may have an impact on the amination reaction, an experiment in which the reaction time of this process was adjusted was carried out. The reaction time was selected as 12, 24, 48 and 72 h. In addition, a series of characterization analyses were conducted on the resulting products.

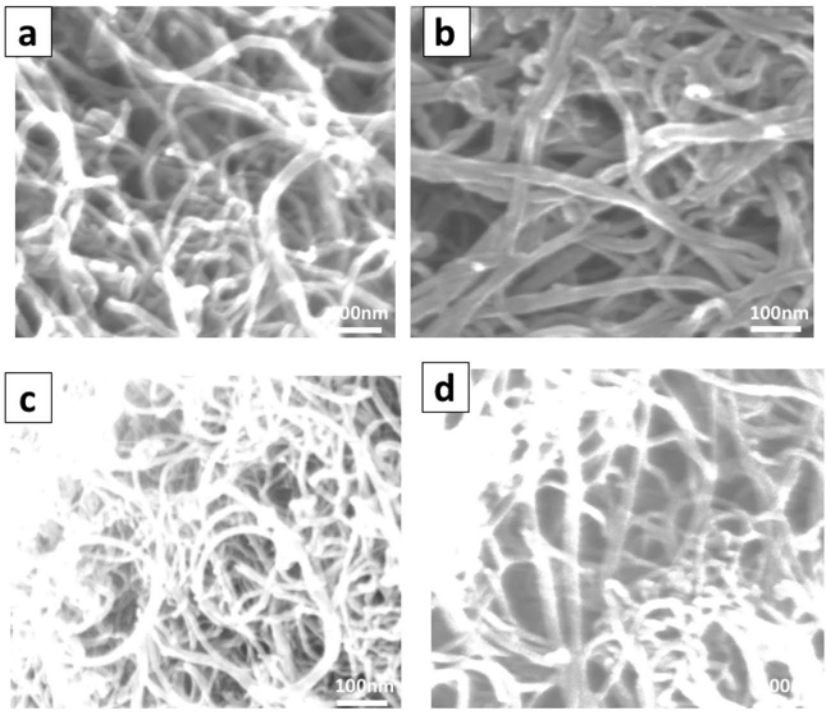

Figure 4-8 SEM images of Modified-MWCNTs-3 treated with 72 mL of ethylenediamine at 100°C for (a) 12 h, (b) 24 h, (c) 48 h and (d) 72 h

Figure 4-8 shows SEM images of Modified-MWCNTs-3 obtained after the amination of 0.3 g of Modified-MWCNTs-2 and 72 mL of ethylenediamine at a constant temperature of 100°C for different reaction times. From Figure 4-8 a, it can be seen that the MWCNT products prepared with a 12 h reaction time have a smooth surface, a uniform size, a small gap between tubes, a long tube length and decreased damage. Figure 4-8 b shows that the product has better dispersibility and basically no bonding or winding phenomena. Notably, these MWCNT also have an uneven thickness. When the reaction time was increased to 48 h (see Figure 4-8 c), the MWCNT reaction product showed slight winding between the tube wall and the port at the uneven. In addition to winding and bonding, more serious fracture appears in the 72 h reaction product (Figure d). According to this analysis, the optimized reaction times were concluded as 24 h and 48 h.

To determine the optimal amination reaction time, the structure of the product obtained from different amination reaction times was characterized by FT-IR spectroscopy. Figure 4-9 shows the IR spectra of the Modified-MWCNTs-3 sample obtained after amination for various times. The characteristic absorption peak of the N-H bond in the amide group was observed at 1637 cm^{-1}. The absorption peak of the C-

N bond in the amide group at 1070 cm^{-1} was most obvious when the reaction time was 48 h.

Bending and stretching vibration peaks of weaker C-H bonds also appeared between 2800 and 3000 cm^{-1}, and no -COOH absorption peak was observed at 1720 cm^{-1}. Thus, the carboxyl groups were considered totally substituted by the chloride groups and by the subsequent amination reaction. In addition, the amino group is grafted to the surface of the MWCNTs with amide bond formation. Moreover, when the reaction time is 48 h, many more amide groups were observed on the surface of the Modified-MWCNTs-3. According to the SEM and FT-IR characterization results, the optimum amination reaction time was 48 h.

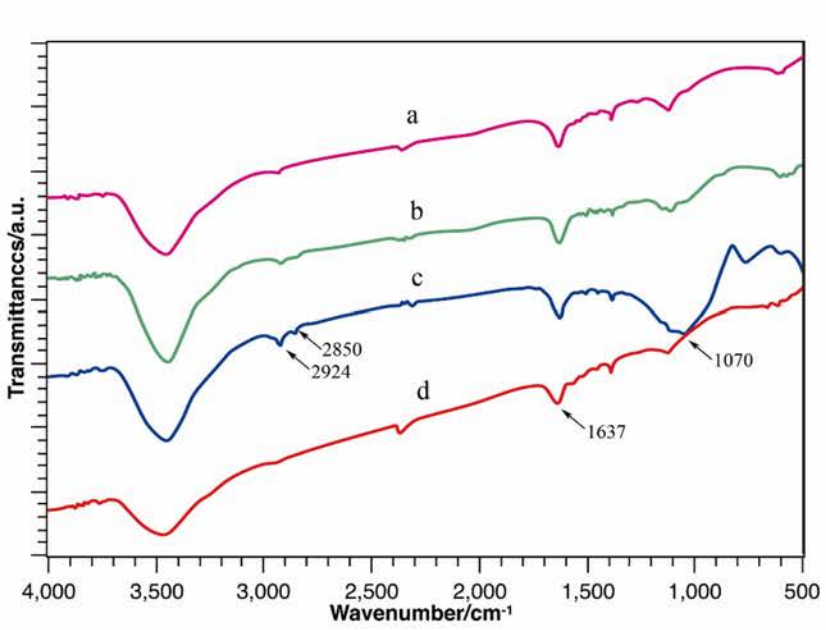

Figure 4-9 FT-IR spectra of MWCNTs treated with 72 mL of ethylenediamine at 100°C for different times: (a) 12 h, (b) 24 h, (c) 48 h and (d) 72 h.

Therefore, SEM and FT-IR analysis of Modified-MWCNTs-3 shows that the best amination reaction time and conditions are as follows: 0.3 g of Modified-MWCNTs-2 were dispersed in 72 mL of ethylenediamine and reacted for 48 h at 100°C. Then, we obtain Modified-MWCNTs-3 with the best dispersibility, a lower degree of entanglement and more surface-grafted amide groups.

4.2.1.3. Structure of functional carbon nanotubes

1) FT-IR analysis of differently modified carbon nanotubes

FT-IR spectra of MWCNTs at different modification stages are shown in Figure 4-10. In the figure, MWCNTs-0 showed no obvious absorption except for the -OH absorption peak at 3449 cm^{-1}. The appearance of this peak is related to the strong water absorption of MWCNTs-0. The Modified-MWCNTs-1 showed two new absorption peaks at 1730 and 1634 cm^{-1}, which originate from the stretching vibrations of -COOH and C=O groups, respectively. Moreover, a C-O absorption peak appeared at 1400 cm^{-1}. After amine functionalization, the -COOH and C-O absorption peaks at 1720 and 1400 cm^{-1} disappear. Symmetrical and asymmetric stretching vibrational absorption peaks of C-H bonds at 2925 and 2851 cm^{-1} appeared, and a peak corresponding to the N-H bonds was observed at 1637 cm^{-1}. In addition, the absorption at 1070 cm^{-1} was attributed to the C-N stretching vibration. FT-IR analysis shows that amide functional groups were introduced into the MWCNTs through amine functionalization.

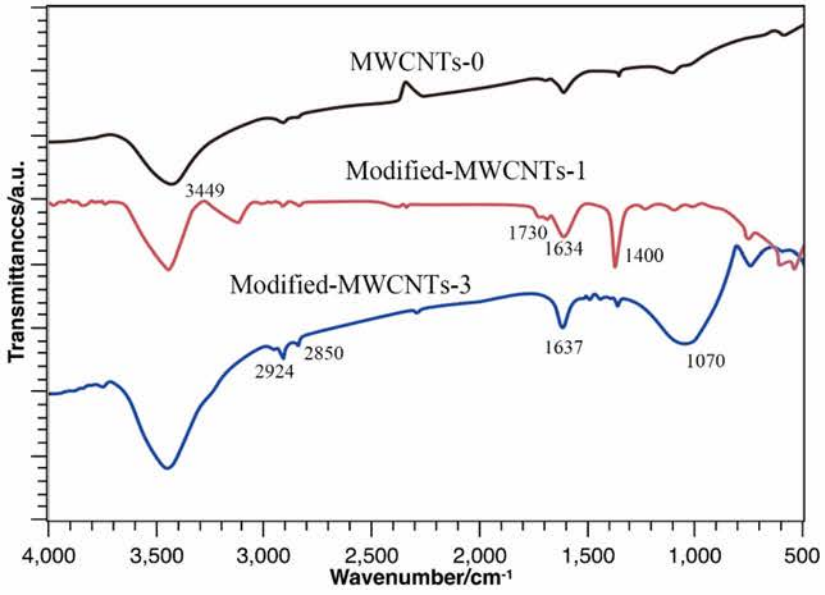

Figure 4-10 FT-IR spectra of modified MWCNTs

2) TGA of differently modified carbon nanotubes

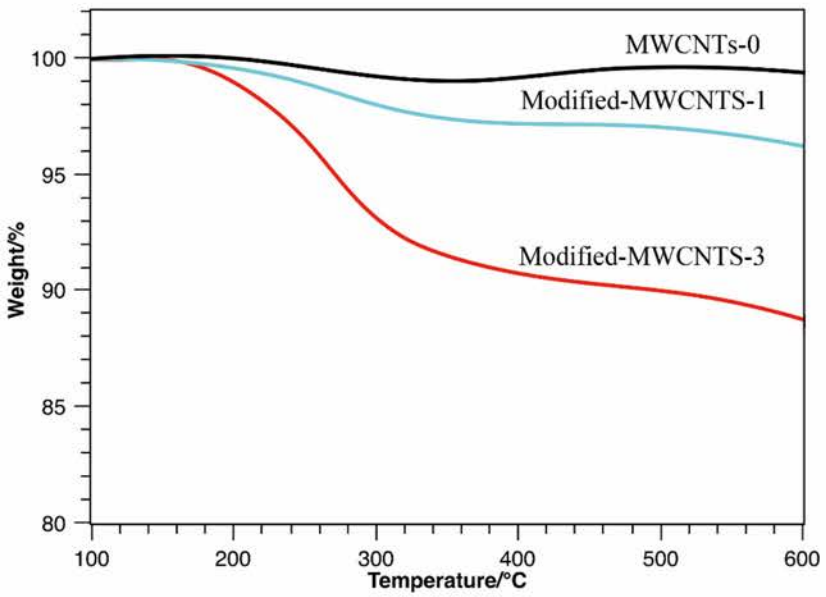

Figure 4-11 TGA curves of modified MWCNTs

Figure 4-11 shows TGA curves of MWCNTs in different modification stages under an inert atmosphere. Under an inert atmosphere, the weight loss rate of MWCNTs can be calculated by the formula:

$$\gamma = (W_0 - W)/W_0$$

Equation 4-1

where W_0 is the original weight before warming and W is the weight after warming

The weight loss rate of MWCNTs-0 at 600°C, which was calculated from the curves in the figure above, is only 1%. MWCNTs-0 show almost no decomposition under an inert atmosphere. By contrast, the Modified-MWCNTs-1 and Modified-MWCNTs-3 show significant weight loss. The weight loss stems from the decomposition of functional groups on the surface of the MWCNTs. Among all the samples, Modified-MWCNTs-1 have a relatively smooth weight loss curve with a weight loss rate of 4.6%. This behavior derives from the decomposition of the surface oxygen-containing functional groups. The weight loss curve of Modified-MWCNTs-3 shows two distinct steps between 100 and 300°C. In addition, the main weight loss peak appears at 220°C, while the second weight loss peak appears near 340°C. This second peak can be attributed to the decomposition of alkane segments on the surface of the Modified-MWCNTs-3. Importantly, the peak appears above 120°C, indicating that it was not

caused by ethylenediamine, which has a boiling point of 117°C. If ethylenediamine was simply adsorbed on the surface of the MWCNTs, the peak should appear below 120°C (the boiling point of ethylenediamine). Thus, the TGA results further illustrate that ethylenediamine is chemically grafted onto the MWCNT surface. According to the formula, the ethylenediamine grafting rate is 12.4%.

3) XPS analysis of differently modified carbon nanotubes

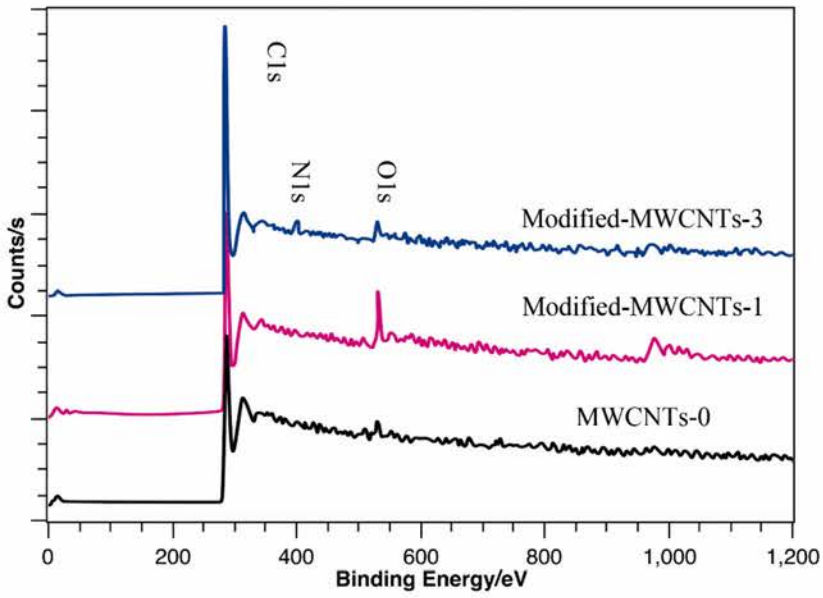

Figure 4-12 XPS survey spectra of modified MWCNTs

To further investigate the surface functional groups of MWCNTs treated by different modification methods, XPS survey analysis of the MWCNTs was carried out as shown in Figure 4-12. As seen from Figure 4-13 and Figure 4-14, in all the XPS spectra of the MWCNTs, the C1s peak appeared at 284 eV. In addition, there was no impurity peak from the catalyst, such as Fe or Ni. After mixed acid modification, the O1s peak of the oxygen atom in the O-H groups appeared at 532 eV. This result demonstrated that the acidification process introduced oxygen-containing functional groups onto the surface of the MWCNTs. Furthermore, after amination modification, the N1s peak corresponding to nitrogen in the amide group appeared at 402 eV. The lack of a N1s peak at 399 eV corresponding to the nitrogen atom in an amine group demonstrated that ethylenediamine is grafted onto the surface of the MWCNTs via amide bond formation. To analyze the change in oxygen-containing functional groups on the surface of differently modified MWCNTs, the C1s and O1s peaks were analyzed.

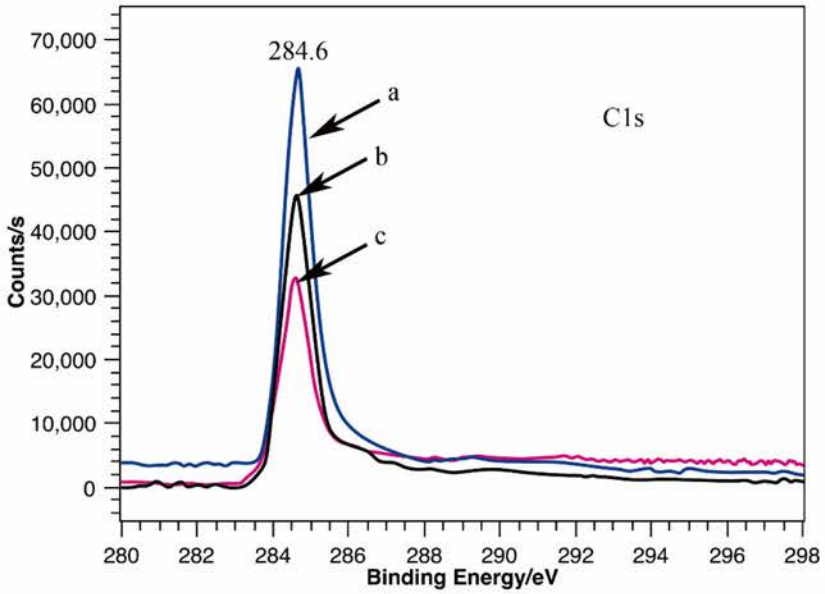

Figure 4-13 C1s spectra of modified MWCNTs: (a) MWCNTs-0, (b) Modified-MWCNTs-1, and (c) Modified-MWCNTs-3

As shown Figure 4-13 above (the C1s peak spectra), the intensity of the C1s peak of MWCNTs-0, Modified-MWCNTs-1 and Modified-MWCNTs-3 decreases gradually, indicating that a modified layer is formed on the surface of the MWCNTs. From Figure 4-14, for the O1s peak, the peak of Modified-MWCNTs-1 was the strongest, indicating that more oxygen-containing functional groups were grafted onto the surface of the MWCNTs after acidification. Compared with that of the Modified-MWCNTs-1, the O1s peak intensity of the Modified-MWCNTs-3 is weaker. Moreover, the binding energy of the O1s peak of the Modified-MWCNTs-3 is reduced. This change is due to the substitution of the hydroxyl groups in the carboxyl groups on the surface of the Modified-MWCNTs-1 by amine groups during the amination process, which leads to a decrease in the oxygen content. At the same time, the amino groups have a strong electron-donating effect and cause a shift in the O1s peak to a lower binding energy.

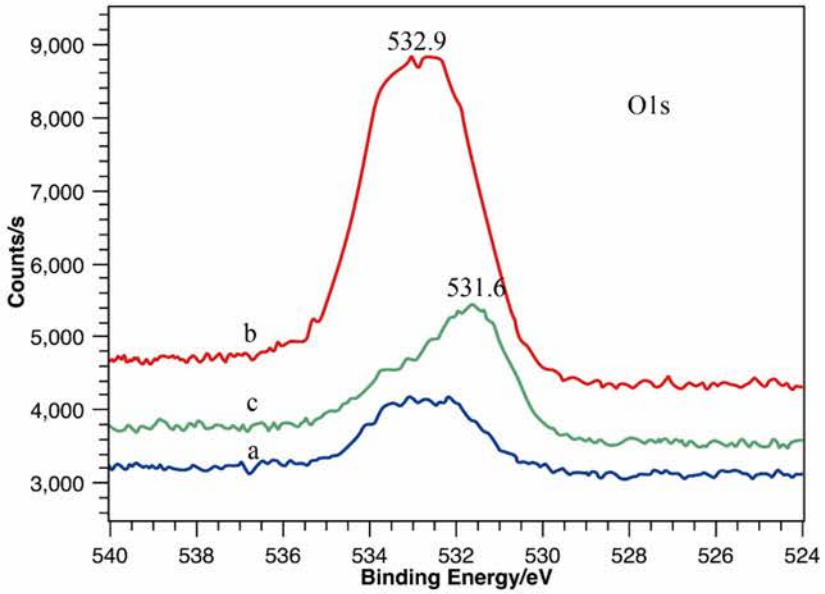

Figure 4-14 O1s spectra of modified MWCNTs: (a) MWCNTs-0, (b) Modified-MWCNTs-1, and (c) Modified-MWCNTs-3

4) SEM analysis of differently modified carbon nanotubes

Figure 4-15 shows SEM images of differently modified carbon nanotubes. The figure reveals that the packing of MWCNTs-0 is relatively loose. After mixed acid treatment, the length of the MWCNTs became shorter, and polar functional groups were formed on the surface of the MWCNTs. Thus, hydrogen-bonding interactions were generated, leading to the adhesion and aggregation of the MWCNTs. Due to the enhanced force between MWCNTs, the MWCNTs are not easily redispersed even after repeated grinding. This finding shows that after mixed acid treatment, the structure of the MWCNTs is changed. Furthermore, carboxyl functional groups are grafted onto the surface of the MWCNTs, which enhances the interaction between MWCNTs. After amination, the distance between MWCNTs increased, making them fluffy again. Moreover, the amine functional group also has a steric hindrance effect, which weakens the hydrogen-bonding interaction between the MWCNTs and forms amide groups on the surface of the MWCNTs. This helps improve the dispersibility of the MWCNTs in the matrix and enhance the interfacial phase between the MWCNTs and the matrix.

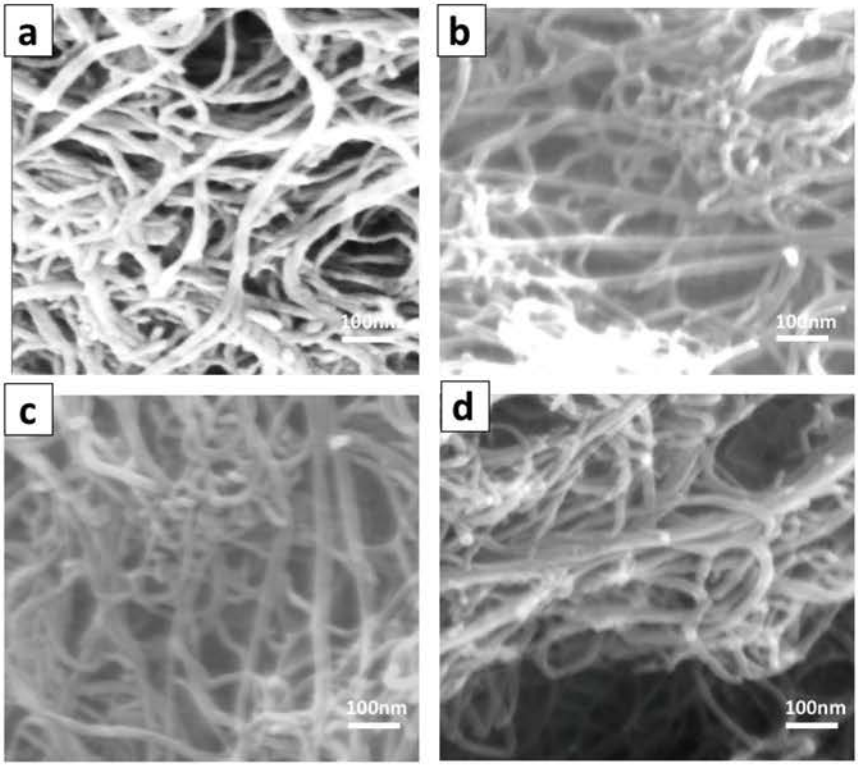

Figure 4-15 SEM images of modified MWCNTs: (a) MWCNTs-0, (b) Modified-MWCNTs-1, (c) Modified-MWCNTs-2, and (d) Modified-MWCNTs-3

4.2.2. Properties of carbon nanotube/natural rubber composites

4.2.2.1. Dispersion state and hybrid filler network of Modified-MWCNTs-3

The dispersion of the filler in the polymer matrix is an important factor affecting the mechanical properties of composites. The uniform dispersion of carbon nanotubes and the formation of hybrid filler networks ensure efficient stress transfer and additional energy dissipation under deformation conditions. These factors are conducive to improving the mechanical properties of rubber composites. The nonlinear viscoelastic properties of composites with shear strain were studied. In general, the absolute value of the storage modulus G' in the low-strain region can characterize the filler network strength and the interaction between the filler materials.

As shown in Figure 4-16, the storage modulus of the composites nonlinearly decreases with increasing strain, which is also known as the Payne effect. These results show that the Payne effect of the natural rubber composites prepared in this experiment follows the order CNT-9, CNT-7, CNT-5, CNT-3, CNT-0, and CNT-1, indicating that an effective hybrid filler network forms only when the CNT filler amount in the composites is equal to or greater than that of CNT-3. Although CNT-9 was filled with

the lowest amount of filler, it exhibited the highest storage modulus and Payne effect, indicating the formation of the strongest filler network.

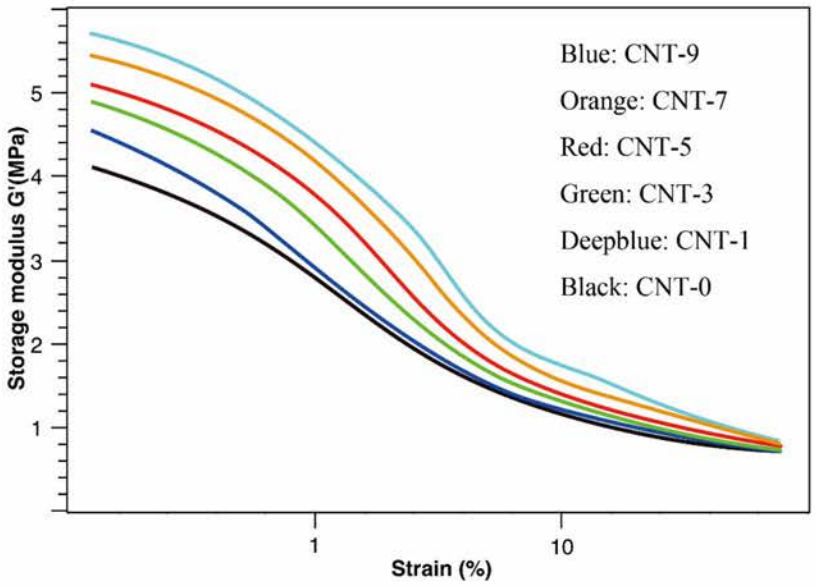

Figure 4-16 Shear storage modulus G' versus dynamic strain amplitude

4.2.2.2. Mechanical properties

The natural rubber composites prepared in this study have similar hardness. In addition, the mechanical properties of the composites are shown in the Table 4-3 below.

Table 4-3 Mechanical properties of different CNT/NR composites

	CNT-0	CNT-1	CNT-3	CNT-5	CNT-7	CNT-9
Tensile Strength/MPa	23.1	26.3	27.1	29.1	29.0	28.1
Tear Strength/kN m^{-1}	92.1	100.1	102.9	101.4	102.3	101.1
100% Modulus /MPa	2.1	2.6	2.9	3.9	3.3	3.1
300% Modulus /MPa	9.1	10.7	12.1	14.2	13.3	12.2
Elongation at Break/%	643	633	603	585	550	530

Due to the introduction of defects and crack randomness, different rubber materials can have different crack propagation behavior. Tear strength may provide erroneous results and information if the fracture toughness behavior of the material is determined only by the deformation.

As the amount of CNTs increases, the 100% modulus and 300% modulus of all the

corresponding samples increase significantly, especially for the CNT-5 composites. Compared to those of CNT-0, the 100% and 300% modulus of CNT-5 increased by 64% and 57%, respectively. The tensile strength and tear strength are also improved, indicating that as the amount of CNTs increases, the mechanical and fatigue properties are improved. Fibrous CNTs have higher enhancement efficiency than spherical CBs. This result can be attributed to the significant enhancement effect of CNTs. The tensile strength and tear strength of rubber materials are determined by the maximum breaking force.

4.2.2.3. Hysteresis loss

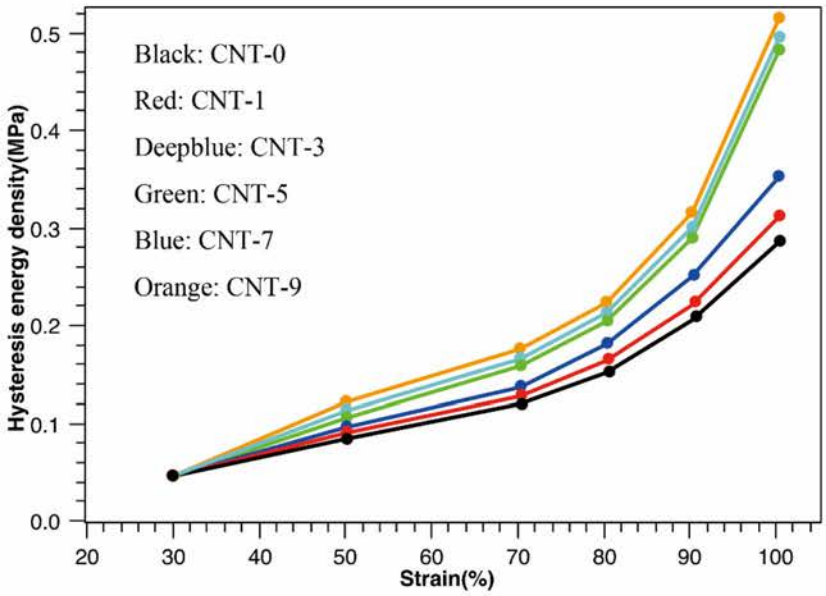

Figure 4-17 HED of CNT/NR composites under varied strains

There are two main sources of energy dissipation in elastomeric materials. Many scholars have studied the relationship between hysteresis loss and crack propagation. One mathematical formula shows that hysteresis loss can increase the energy at break. For dynamic cyclic conditions, hysteresis loss can lead to increased crack propagation resistance, which means that the fatigue resistance of the composites is improved.

The hysteresis energy density (HED), a parameter that characterizes the hysteresis loss of composites, can be found directly over the hysteresis loop. The HEDs of CNT/natural rubber composites at different strains are shown in Figure 4-17. Although the CNT-9 composite is filled with the lowest amount of filler, it exhibits the highest HED, especially at higher strain. The tearing energy G(v) on the crack tip at a fixed

crack growth rate v can be expressed by the following equation:

$$G(v) = G_0\left[1+\frac{2}{\pi}\sum{}_0\int_0^{2\pi v/a} d\omega \frac{F(\omega)}{\omega} J^n\right]^{-1}$$

Equation 4-2

where G_0 is the critical energy of crack propagation and $F(\omega)$ is a function. The viscoelastic loss parameter J" can be found from the storage modulus E' and the loss modulus E" according to the following equation:

$$J'' = \frac{E''}{E'^2 + E''^2}$$

Equation 4-3

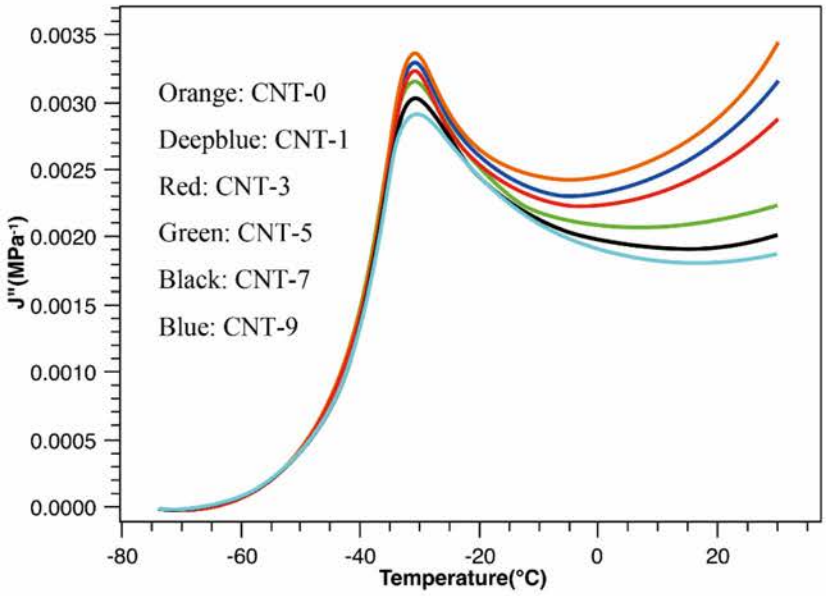

Figure 4-18 Dependence of the loss compliance J" on the temperature for CNT/NR composites

A dynamic mechanical thermal analyzer (DMTA) was used to test the natural rubber composites. Figure 4-18 shows that composites with a lower J" value have higher values of G(v), indicating higher hysteresis loss at the same crack growth rate. All the composites were studied at different temperatures. It can be seen that CNT-9 has the lowest J" value, indicating the greatest hysteresis loss on the crack tip. The combination of the HED and J" results indicates that CNT- 9 exhibits the highest hysteresis loss in the matrix. For natural rubber composites filled with unmodified carbon nanotubes, the high hysteresis under cyclic strain is due to the weaker interfacial interaction between

the unmodified carbon nanotubes and the rubber molecular chains. The highest hysteresis loss under dynamic conditions of CNT-9 leads to significant heat build-up and a temperature increase, promoting breakage of the rubber molecular chain and inhibiting the strain-induced crystallization (SIC). This eventually leads to a reduction in the fatigue crack propagation resistance of the composite.

4.2.2.4. Dynamic fatigue properties

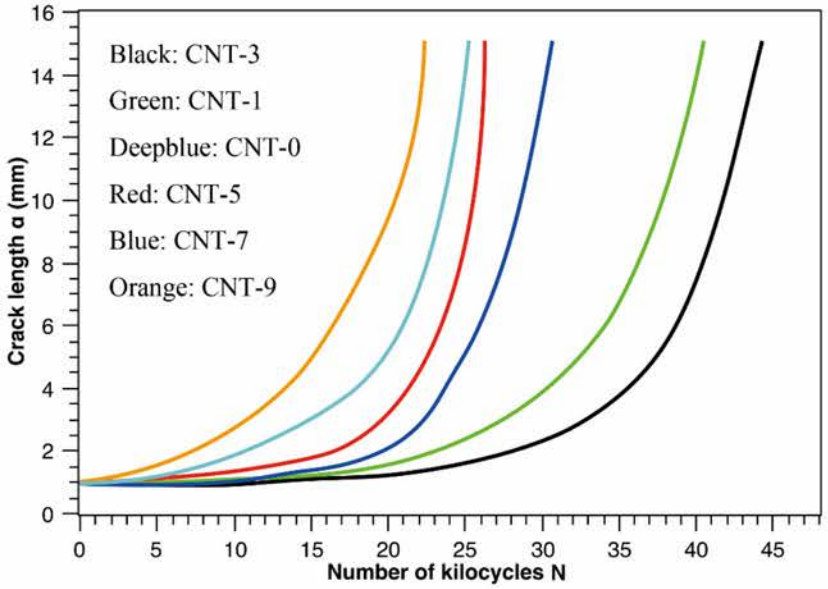

Figure 4-19 Crack length versus the number of dynamic cycles

Singe-notch tensile specimens (SNTSs) with a precut crack length of 1 mm specimens were used for dynamic fatigue testing over a wide range of strains (30% to 100%). Fatigue crack growth curves of various samples at 70% strain are shown in Figure 4-19. In the initial stage of crack propagation, i.e., when the crack length ranged from 1 mm to 3 mm, the crack propagation behavior can be considered a stable expansion process. Above this range, crack propagation becomes unstable, and failure occurs. The crack growth rate da/dN is obtained by measuring the linear slope of the curve between the crack length (crack range from 1 mm to 3 mm) and the number of cycles.

The fatigue lifetime of natural rubber composites is shown in Figure 4-20. CNT-3 exhibits the longest fatigue lifetime, followed by CNT-1 and CNT-0. This result indicates that CNT-3 has the best antifatigue crack propagation properties. However, the fatigue lifetime of CNT-5 is significantly lower than those of CNT-3, CNT-1 and

CNT-0, especially under large strain conditions, which is inconsistent with the mechanical and J-integral test results.

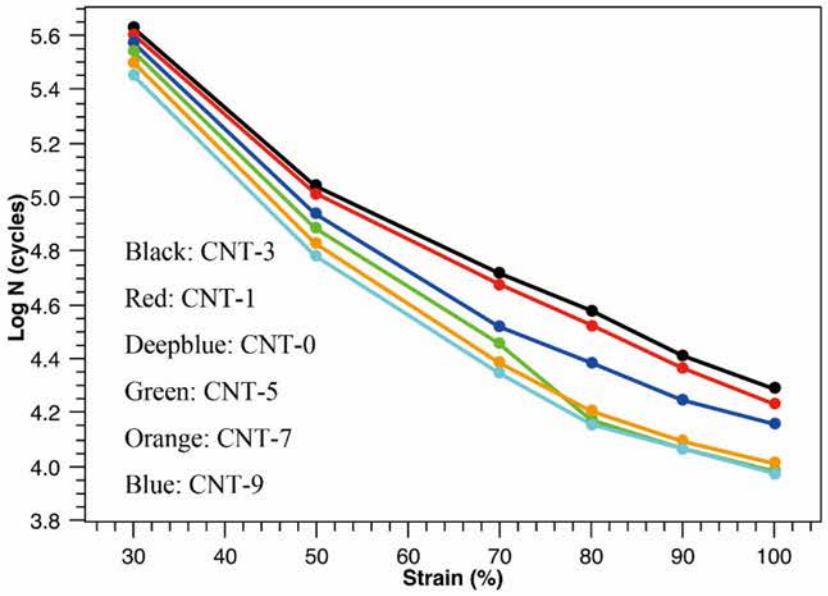

Figure 4-20 Fatigue lifetimes of natural rubber composites

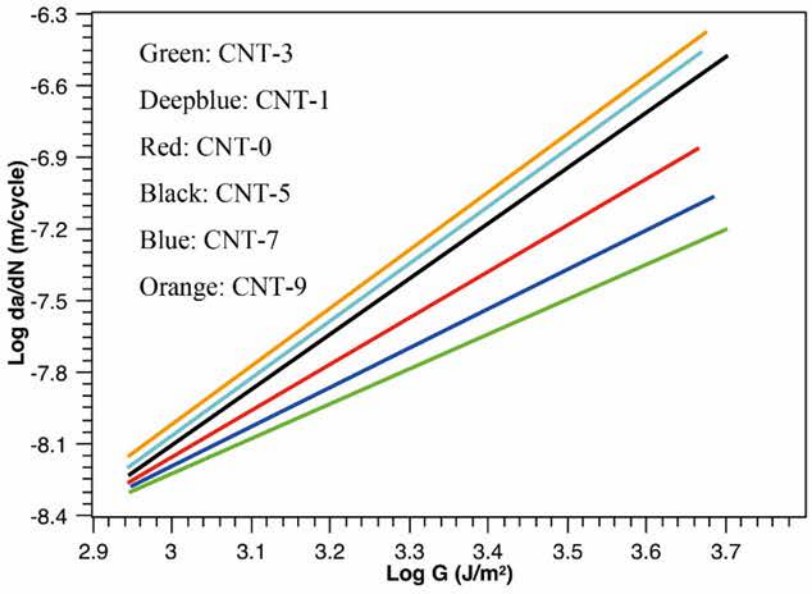

Figure 4-21 Crack growth rates for natural rubber composites

The logarithmic relationship between the crack growth rate da/dN and the tearing energy G at different strains for the composites is shown in Figure 4-21. The da/dN and G of the four composites are all fit well with the power law within the range of the

tearing energy. The fatigue parameters B and β are listed in Table 4-4. It can be seen that at a given tearing energy, CNT-3 exhibits the weakest da/dN and the lowest β, indicating that it has the strongest antifatigue properties. In addition, CNT-9 has the highest da/dN and β, indicating that it has the weakest antifatigue properties.

Table 4-4 Fatigue parameters and the correlation coefficient R^2 of the rubber composites

	B	β	R^2
CNT-0	5.3E-15	2.21	0.97
CNT-1	2.4E-14	1.74	0.99
CNT-3	9.1E-14	1.53	0.98
CNT-5	8.4E-16	2.31	0.97
CNT-7	9.1E-16	2.01	0.98
CNT-9	9.7E-16	2.46	0.97

4.2.2.5. Strain-induced crystallization (SIC) properties

We characterized the SIC behavior of the carbon nanotube/natural rubber composites by their stress-strain curves. For crystalline rubber materials, the sharp rise in the stress-strain curve is mainly due to two factors: limited molecular extensibility and SIC. The classic Mooney-Rivlin equation cannot distinguish between the two factors. Thus, we studied a new kind of modification of the parameters to exclude the limited elongation of the rubber molecular chain as follows:

$$\sigma = 2\left(C_1 + \frac{C_2}{\lambda}\right)\left(\lambda - \frac{1}{\lambda^2}\right) f(\lambda)$$

Equation 4-4

$$f(\lambda) = \left(1 + \frac{1}{3}\frac{\lambda^2}{\lambda_m^2}\right)$$

Equation 4-5

where σ is the nominal stress, λ is the draw ratio, λ_m is the maximum draw ratio at break, and C_1 & C_2 are constants. The boundary conditions range from $(\lambda - \lambda^2) f(\lambda)$ to $F(\lambda)$. The plot for the reciprocal λ^{-1} of the draw ratio λ should produce a linear

region.

The critical turning point λ_{up} of the draw ratio is considered the point of SIC and is obtained from the equation:

$$\lambda_{up}^{3} = \frac{3\lambda_{m}^{2}C_{2}}{2C_{1}}$$

Equation 4-6

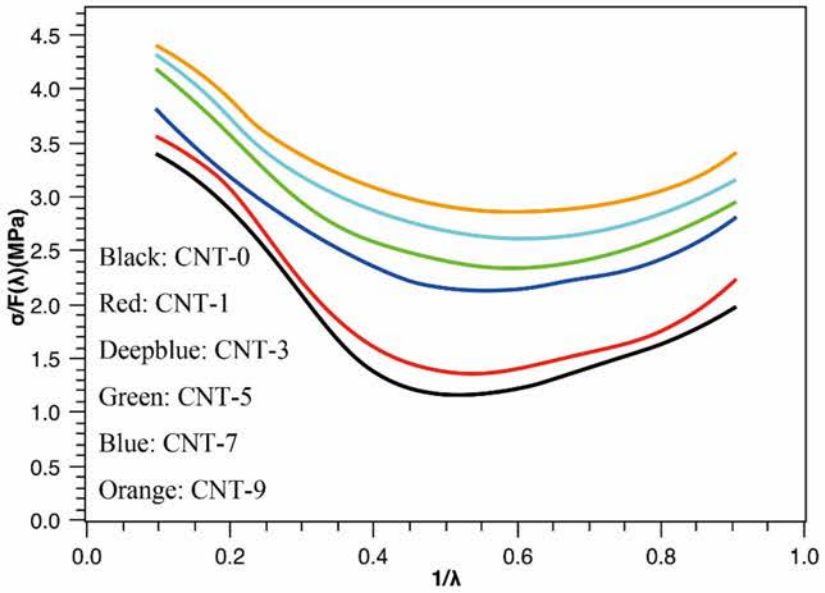

Figure 4-22 Modified Mooney-Rivlin plots of rubber composites

The relationship between $\sigma/F(\lambda)$ and λ^{-1} for natural rubber composites is shown in Figure 4-22. The resulting C_1, C_2 and critical λ_{up} values are shown in Table 4-5. C_1 reflects the modulus of elasticity and crosslinking density of the corresponding samples. CNT-9 shows the largest C_1 value. The $\sigma/F(\lambda)$~λ^{-1} curves of all the composites showed large and sudden drops in the low λ^{-1} region. CNT-9 has the lowest λ_{up}, indicating that the addition of CNTs enhances the SIC of natural rubber composites. There are two main reasons for this enhancement. First, fibrous CNTs with a high degree of anisotropy are easily oriented in the stretching direction. Oriented CNTs reduce the entropy of the mixed system, resulting in easy orientation and crystallization of the rubber molecular chains. Second, the fibrous CNTs produce more pronounced crack-tip strain amplification effects than spherical CBs. Highly oriented rubber molecular chains and CNTs at the crack tip increase the crack deflection, passivation and branching ability. The morphology of the fracture specimen under 70% strain is shown in the Figure 4-22.

The deflection tendency of the crack is found to gradually increase as the CNT content increases, which indicates that the crack propagation resistance gradually increases.

Table 4-5 Values of C and λ

Samples	C_1 (MPa)	C_2 (MPa)	λ_{up}
CNT-0	0.353	0.407	4.50
CNT-1	0.474	0.414	4.17
CNT-3	0.631	0.451	3.91
CNT-5	0.732	0.431	3.51
CNT-7	0.791	0.451	3.32
CNT-9	0.809	0.403	3.21

4.2.2.6. Tearing energy

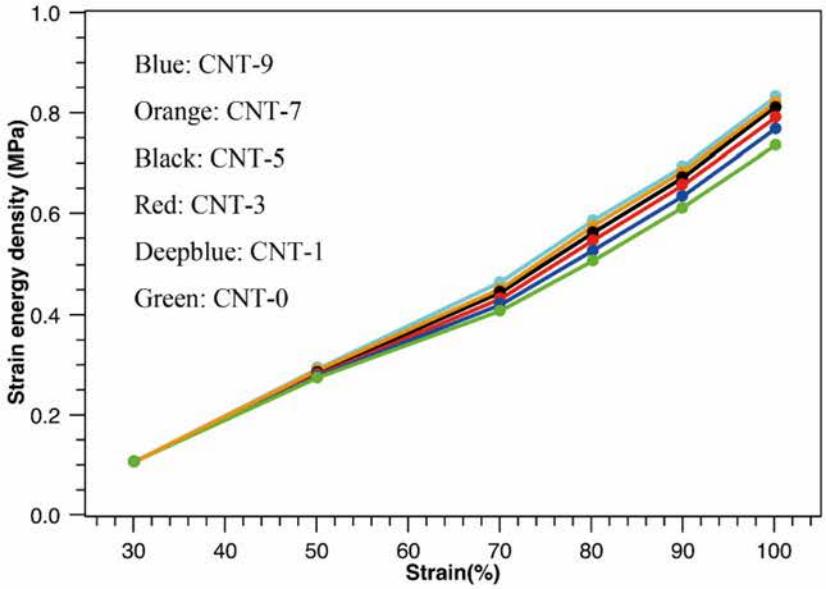

Figure 4-23 SED of carbon nanotube/natural rubber composites under different strains

Tearing energy directly affects the fatigue crack growth performance and fatigue lifetime of rubber materials. The tearing energy can be proportional to the strain energy density (SED) for an SNTS with a specific crack length at a particular strain. The SED values for different composites at different strains are shown in Figure 4-23. Compared to the other composites, CNT-9 shows a higher SED at all strains. However, the gap between the SEDs is very small. For example, the SED gap between CNT-0 and CNT-

9 at 100% strain is only 9%. Here, we can assume that under certain strain conditions, the input of tearing energy with a repetitive fatigue cycle with the increase in CNT fraction can be similar, which means that the "driving forces" of the four composites are almost equal in terms of fatigue crack growth.

4.2.2.7. J-integral test

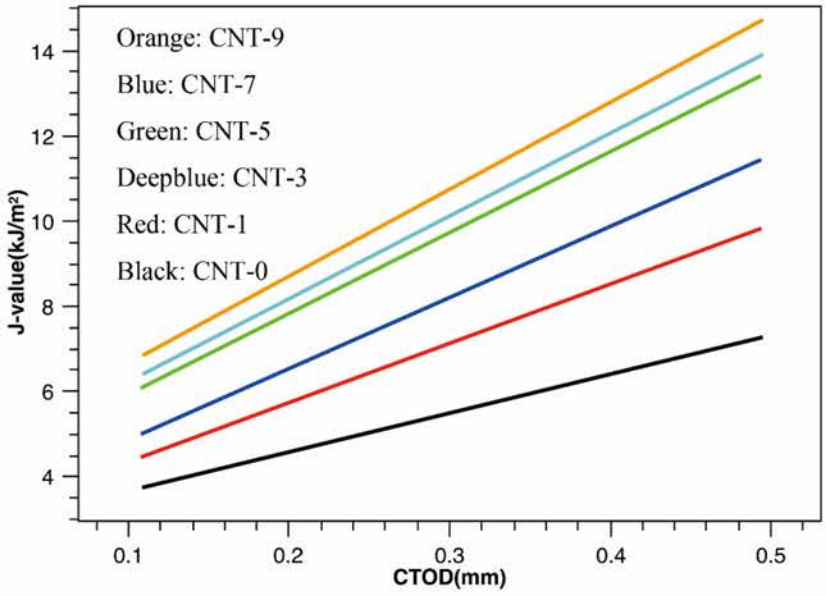

Figure 4-24 *J*-value versus crack-tip opening displacement

We preparaed samples with a 4 mm precut crack. The relationships between the J-integral and the crack-tip opening displacement (CTOD) of the composites are as shown in Figure 4-24. The critical energy J_{IC} is an evaluation criterion for crack initiation behavior.

Table 4-6 J_{IC} and T_R of composites

Samples	T_R(MPa)	J_{IC}(kJ • m^{-2})	R^2
CNT-0	11.1	4.04	0.97
CNT-1	15.3	4.65	0.99
CNT-3	17.3	5.34	0.98
CNT-5	19.4	6.32	0.99
CNT-7	20.3	7.33	0.99
CNT-9	20.2	7.98	0.99

The J_{IC}, T_R and correlation coefficient R^2 values are shown in Table 4-6. Based on the results of the J-integral test, we believe that the partial replacement of CB with CNTs can indeed improve the resistance against crack initiation and crack propagation.

4.3. Summary

By studying the effects of different mixed acid treatments on the structure and properties of MWCNTs, we found that mixed acid treatment time and volume have a great influence on the surface grafting rate of MWCNTs. In addition, as the mixed acid treatment time and amount increase, the content of oxygen-containing functional groups on the surface of the MWCNTs first increases and then decreases quickly. This behavior is observed because of the damage to the MWCNTs by the acid treatment. According to the SEM and TGA results, the optimal conditions for the acidification were as follows: 1 g of MWCNTs were treated with 80 mL of mixed acid at 50°C for 2 h. The Modified-MWCNTs-1 resulting from the optimal acidification conditions were then reacted with ethylenediamine in a two-step procedure. The effects of the ethylenediamine amount and amination time on the surface amidation of Modified-MWCNTs-1 were investigated. The results show that under the optimal reaction conditions, the Modified-MWCNTs-1 can be effectively acylated and amidated to form the amidated product (Modified-MWCNTs-3). According to the SEM and FT-IR results, the optimal parameters of the amination process were the reaction of 0.3 g of Modified-MWCNTs-2 with 72 mL of ethylenediamine at 100°C for 48 h. Through SEM, TGA, FT-IR, and XPS analyses, it was proved that the diamine group could be grafted onto the surface of the MWCNTs through amination.

The combination of CNTs and CB has synergistic effect on the mechanical properties and crack propagation resistance of natural rubber composites. Adding a small amount of CNTs can significantly improve anti-crack-initiation performance and anti-crack-propagation performance. CNT-3 shows the strongest antidynamic fatigue performance. The addition of CNTs will increase the SIC of natural rubber, which tends to cause crack deflection. CNT-9 shows the weakest dynamic fatigue performance because its hysteresis loss is much higher than those of the other rubber composites. Severe fatigue heat can significantly reduce the dynamic fatigue resistance of composites. Therefore, finding the best method to modify CNTs and the best formula for rubber composites is essential for achieving the synergistic effect between CNTs and CB.

Chapter 5. Composites of Natural Rubber and Graphene

5.1. Introduction

Graphene and graphene oxide (GO) have great potential for industrial application. However, there are still many problems with the processing of graphene and GO [82]. For example, graphene and GO are hardly dispersible in nonpolar solvents. Furthermore, the compatibility between graphene and nonpolar polymers such as natural rubber, polypropylene (PP), and polystyrene (PS) is poor. To solve these problems, we need to modify and functionalize graphene and GO. The most important method is chemical modification, which can not only enhance the weak interaction of graphene and GO but also improve the performance of graphene and GO, which can expand their application scope. For example, GO-grafted clay nanoparticles can provide GO with red fluorescence. This red fluorescent GO can be used in the fields of biolabeling and cytochemistry [8].

GO has oxygen-containing functional groups, such as carboxyl groups, hydroxyl groups and epoxy groups, that can serve as reaction sites to facilitate the covalent modification of GO. For example, the carboxyl groups on GO can be amidated with amino groups, and the epoxy groups on GO are easily substituted by nucleophilic groups. Grafting graphene and GO through covalent bonds to a polymer can improve their dispersion in solvent, which can greatly enhance compatibility between graphene or GO and rubber composites.

Moreover, due to the chemical diversity of polymers, we can control the intrinsic properties of graphene and GO by changing the molecular weight and type of the grafted polymers.

In this chapter, we improve the dispersibility of modified graphene or GO in nonpolar organic solvents such as xylene. Subsequently, we use the modified graphene in the next step: preparation of high-performance rubber composites.

In this chapter, we prepared 7 kinds of rubber composites. The influence of modified graphene loading on the mechanical properties and crack propagation performance of natural rubber composites is investigated.

5.2. Results and discussion

5.2.1. Functionalization of graphene

5.2.1.1. Structure and performance of Modified-Graphene-1

The reaction to prepare Modified-Graphene-1 is shown in Figure 5-1. We use the carboxyl group on graphene to react with octadecylamine (ODA) via amindation, and then we obtain long-chain alkyl-grafted graphene.

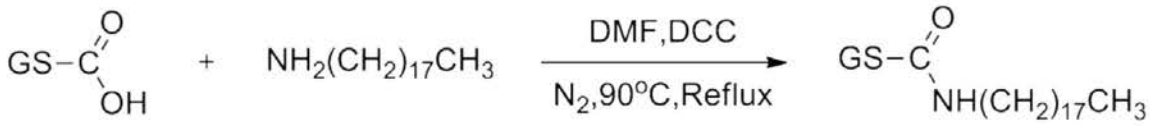

Figure 5-1 Reaction to synthesize Modified-Graphene-1

The grafting of octadecyl amine considerably changes the surface properties and solvent dispersibility of graphene. To demonstrate the difference in solvent dispersibility between graphene and modified graphene, we disperse them in ammonia solution (concentration of approximately 0.1%, pH 10) and toluene. After the ultrasonication step, the mixed solvent will be in two phases due to the immiscibility of the ammonia solution and toluene. While graphene was mainly dispersed in the ammonia solution, modified graphene was dispersed in the toluene solution. The ability of modified graphene to be dispersed in nonpolar solvent such as toluene indicates the successful grafting of ODA onto the surface.

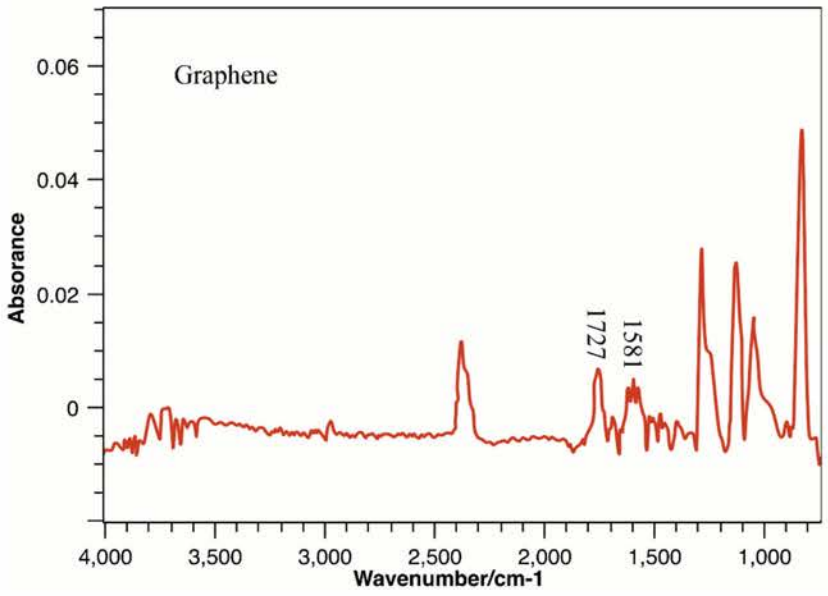

Figure 5-2 FT-IR spectra of graphene

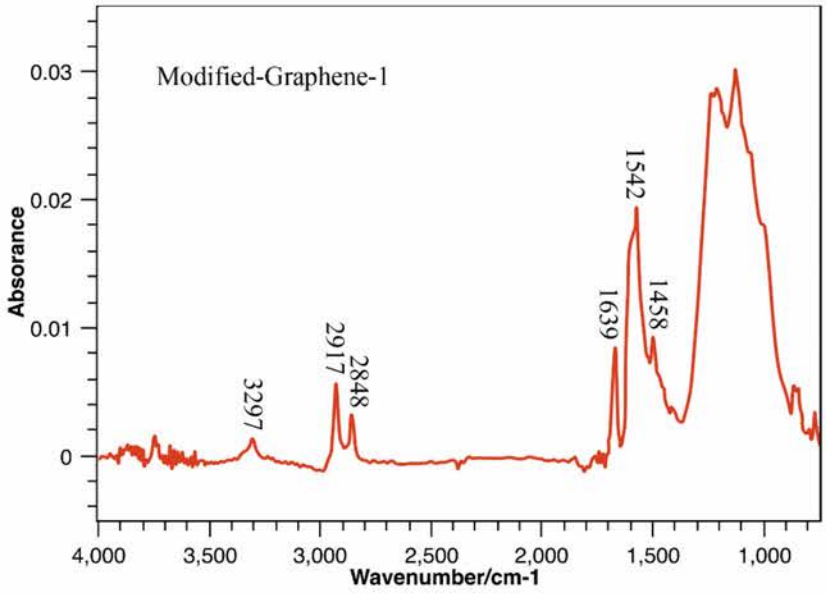

Figure 5-3 FT-IR spectra of Modified-Graphene-1

FT-IR spectroscopy provides evidence for the successful grafting of ODA onto graphene. As shown in Figure 5-2, graphene has two peaks at 1727 and 1581 cm^{-1} corresponding to the stretching vibration peak of C=O in the carboxyl group and the stretching vibration peak of C=C in the conjugated system, respectively. Figure 5-3 shows that after reaction with ODA, the peak at 1727 cm^{-1} corresponding to the carboxyl group disappeared and was replaced by the peak at 1639 cm^{-1} corresponding to the C=O stretching vibration of the amide group. In addition, several new peaks appear in spectrum, such as the peak at 3297 cm^{-1}, corresponding to the stretching vibration peak of N-H in the amide group, and the bending vibration peak of N-H at 1542 cm^{-1}. The IR results indicate that ODA was grafted onto graphene via the amidation reaction.

5.2.1.2. Structure and performance of PS-GO

The preparation route for monodisperse polystyrene (PS) on GO (PS-GO) is shown in Figure 5-4. First, the carboxyl groups on GO are activated with $SOCl_2$ to form acid chloride groups, which then react with the hydroxyl groups on propargyl alcohol. At the same time, the ATRP polymerization of styrene was initiated by AEBiB (an azide-based ATRP initiator) to afford azido-modified monodisperse PS (N-PS) with a molecular weight of 4600 and a monodispersity of 1.04. The tail-alkyne-containing GO underwent a "click" reaction with N-PS to obtain modified PS-GO. The "click" reaction can be carried out at room temperature, and the reaction conditions are very mild. The

experimental route is shown in Figure 5-4. This reaction can adjust the molecular structure of the grafted polymer. In this work, we successfully grafted PS with a uniform molecular weight onto GO.

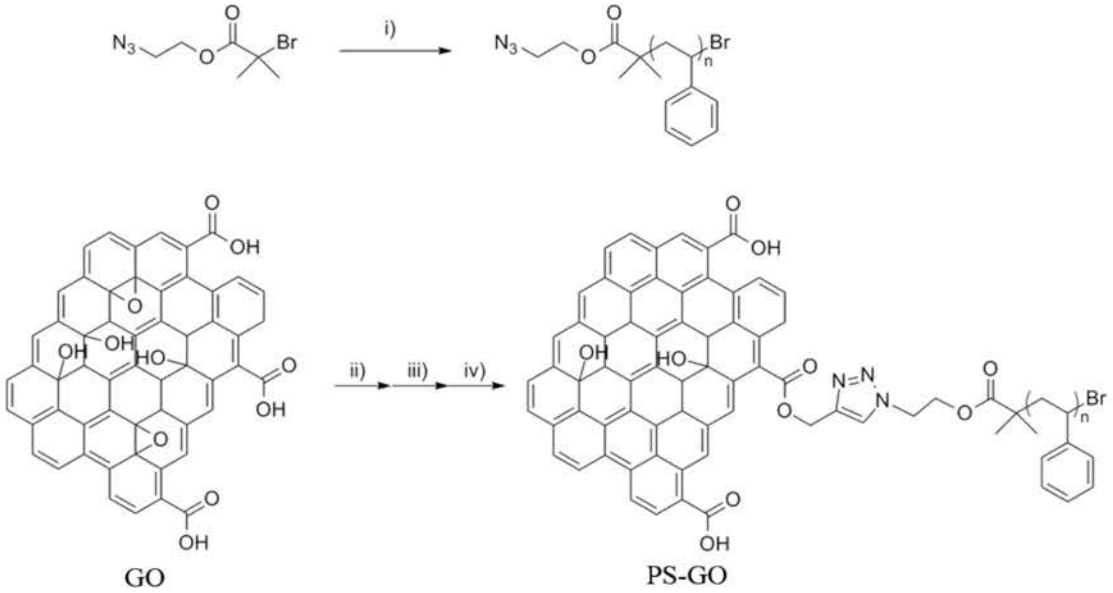

Figure 5-4 Strategy for grafting PS onto GO; i) CuBr, PMDETA, styrene, chlorobenzene, 90°C; ii) $SOCl_2$, 70°C; iii) Propargyl alcohol, TEA, $CHCl_3$, rt; iv) CuBr, PMDETA, DMF.

The easiest way to test whether PS is grafted onto GO is to test the solvent dispersibility of PS-GO. We can conclude that PS-GO disperses well in dimethylformamide (DMF), tetrahydrofuran (THF), methylene chloride and toluene but cannot be dispersed in water and methanol. The above results show that PS is grafted onto GO and determines the solvent dispersibility of the product PS-GO.

FT-IR spectroscopy can also inform us whether PS is grafted onto GO. As shown in Figure 5-5, N-PS has a stretching vibration peak of N_3 at 2100 cm^{-1}, indicating that the N_3 group has not been destroyed during the ATRP polymerization of styrene. In addition, GO has two peaks at 1725 and 1615 cm^{-1} corresponding to the stretching vibration peak of C=O in the carboxyl group and the stretching vibration peak of C=C in the conjugated structure, respectively. After being grafted with PS, the spectrum of PS-GO had several new peaks at 2920, 2850 and 1615 cm^{-1}. These new peaks correspond to the C-H stretching vibration peaks and bending vibration peaks on PS. Therefore, FT-IR spectroscopy confirms that PS was grafted onto GO.

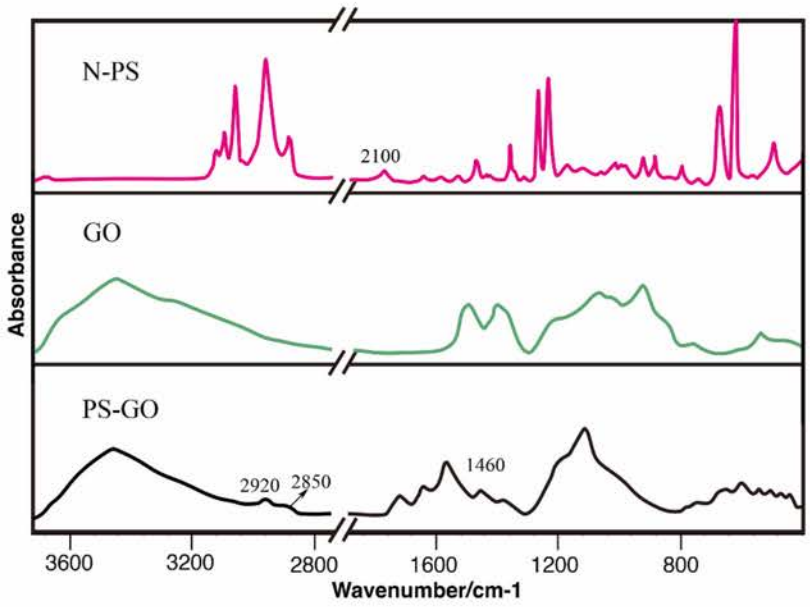

Figure 5-5 FT-IR spectra of N-PS, GO and PS-GO

To quantitatively determine the grafting rate of PS-GO, we performed TGA tests of PS-GO under a nitrogen atmosphere. As seen from the TGA curves in Figure 5-6, Figure 5-7 and Figure 5-8, PS-GO has two weight loss peaks.

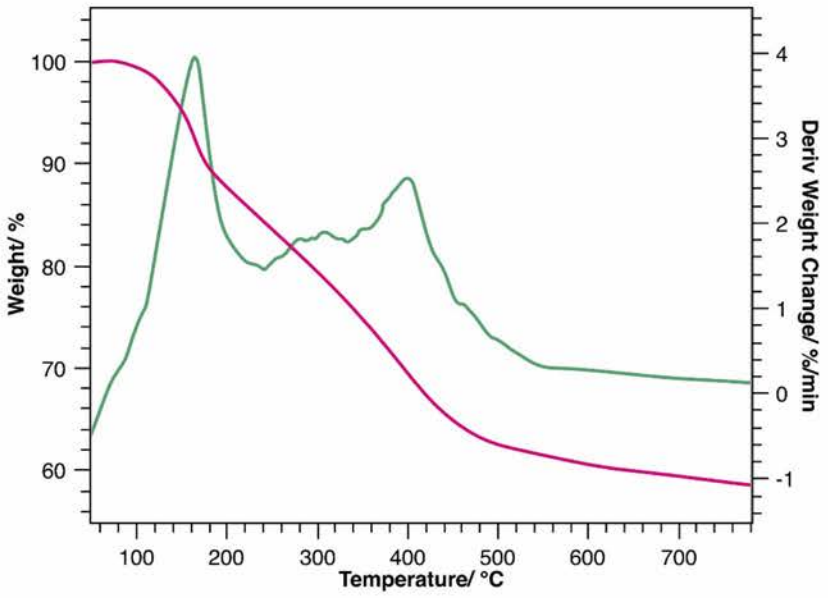

Figure 5-6 TGA and DTG curves of PS-GO

The first peak for GO at 170°C, which can also be seen in the corresponding derivative thermogravimetric analysis (DTG), is consistent with the thermal cracking of the oxygen-containing functional groups on GO. The second peak at 410°C,

corresponding to the thermal decomposition of PS, can also be seen in the DTG curve of N-PS. For PS-GO, the second peak, which is also the thermal decomposition peak of PS, corresponds to a weight loss of 20%; i.e., we can determine that the content of PS on PS-GO is approximately 20 wt%.

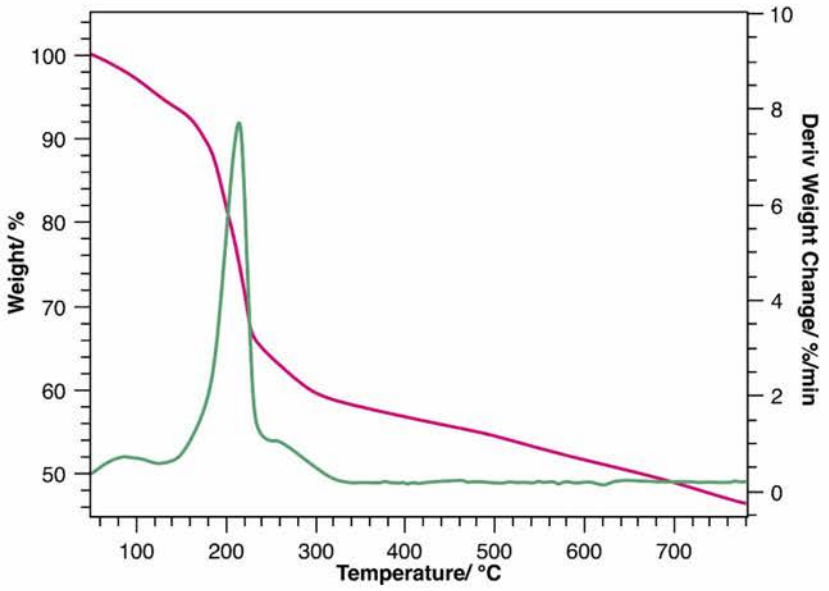

Figure 5-7 TGA and DTG curves of GO

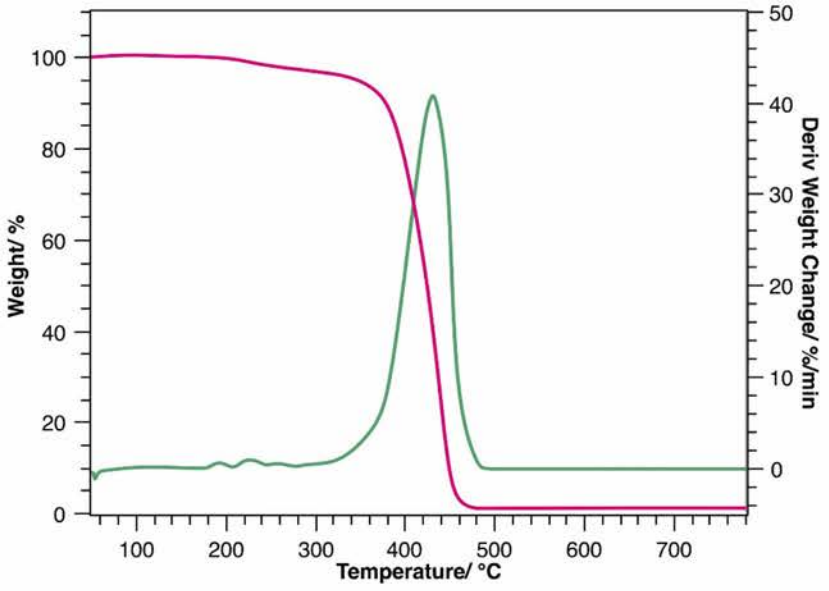

Figure 5-8 TGA and DTG curves of N-PS

Because the molecular weight of grafted PS is 4600, this result indicates that there is one PS chain grafted onto GO for every 1500 carbon atoms. In other words, the

reaction has very high efficiency, and the molecular structure of the grafted polymer is controllable.

Figure 5-9 shows the X-ray diffraction (XRD) curves of GO and PS-GO. GO has a diffraction peak at 10.7° corresponding to a layer spacing of 0.83 nm in GO. There are no obvious diffraction peaks in the XRD curve of PS-GO, indicating that all the layers in PS-GO are disorganized.

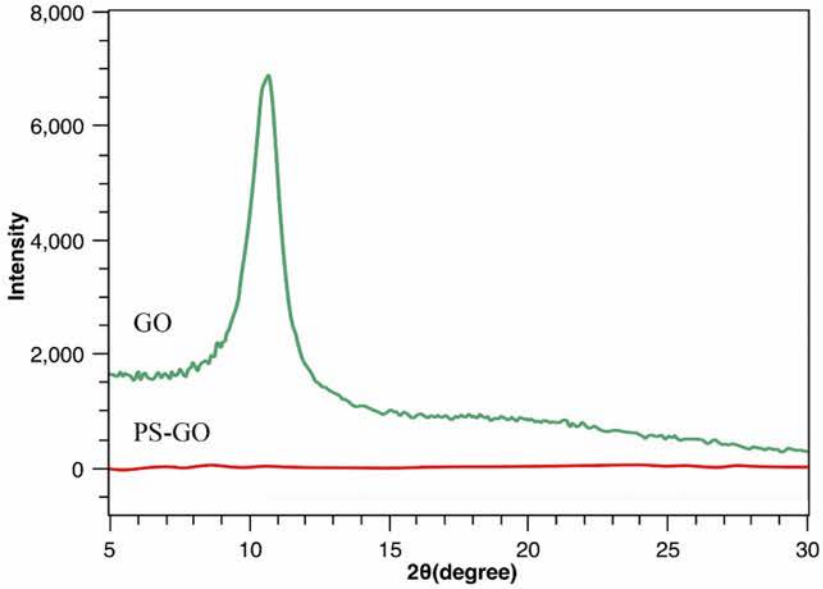

Figure 5-9 XRD curves of GO and PS-GO

The disordered structure of PS-GO should favor its complete stripping in solvent. In addition, the grafting of polymers onto GO often leads to an increase in the thickness of the sheet.

5.2.1.3. Structure and performance of styrene-ethylene/butylene-styrene (SEBS) grafted onto GO (SEBS-GO)

Block polymers are composed of two or more different polymer chains and have unique segment structures. Block polymers have wide range of applications in many areas, such as polymer reinforcements and polymer compatibilizers. Grafting block polymers onto nanoparticles can often give the nanoparticles multiple properties. This strategy is also a popular research direction. However, block polymers have a complicated structure, and it is difficult to obtain the block polymer-grafted nanoparticles by a grafting method. On the other hand, the traditional "grafting-to" method suffers from low graft efficiency. Therefore, we use the highly efficient "click" reaction to graft the

block polymer styrene-ethylene/butylene-styrene (SEBS) onto GO in this study. The SEBS-GO preparation route as shown Figure 5-10. The tail alkynyl group-modified GO has been prepared in the previous experiment. In addition, azido-modified SEBS (N-SEBS) was obtained by a chloromethylation reaction. By comparing the FT-IR spectra of SEBS, CH_2Cl-SEBS, and N-SEBS shown in Figure 5-11, we can see that CH_2Cl-SEBS has a peak at 1265 cm^{-1} corresponding to the stretching vibration peak of C-Cl, indicating that the chloromethylation of SEBS was successful. Compared to CH_2Cl-SEBS, N-SEBS has a distinct peak at 2095 cm^{-1}. This peak corresponds to the stretching vibration peak of N_3, indicating that the azidation of CH_2Cl-SEBS was also successful. Moreover, the appearance of this peak means N-SEBS can be used for the subsequent grafting reaction, in which the tail-terminated alkynyl GO is reacted with N-SEBS to afford SEBS-GO.

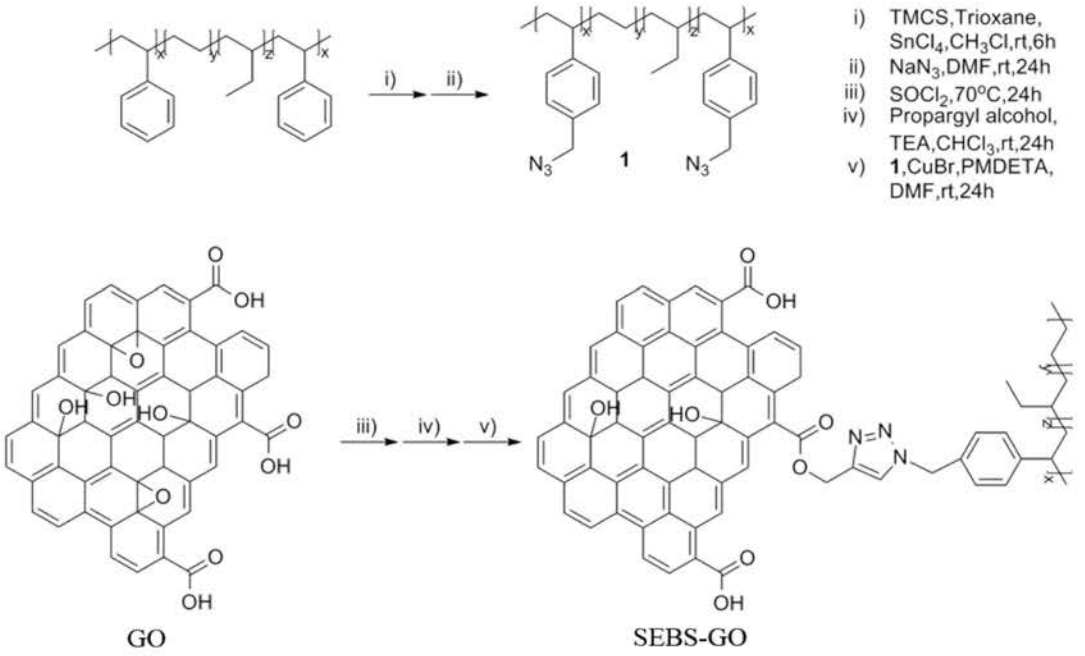

Figure 5-10 Strategy for grafting SEBS onto GO

This study explores the dispersion of SEBS-GO. The modified graphene can be uniformly dispersed in dimethylformamide (DMF), tetrahydrofuran (THF), and N-methyl-2-pyrrolidone (NMP). The above results show that SEBS was successfully grafted onto GO and demonstrated the solvent dispersibility of the product. Because most organic solvents are good solvents for SEBS, we can recognize that modified SEBS-GO will disperse well in most organic solvents.

Figure 5-12 shows FT-IR spectra of GO and SEBS-GO. Compared to GO, SEBS-

GO has two sharp peaks at 2924 and 2854 cm^{-1} corresponding to the stretching vibration peak of C-H on SEBS. At the same time, there is also a peak at 1647 cm^{-1} corresponding to the peak of the triazoles formed in the grafting reaction. These FT-IR data indicate that SEBS is grafted onto GO successfully.

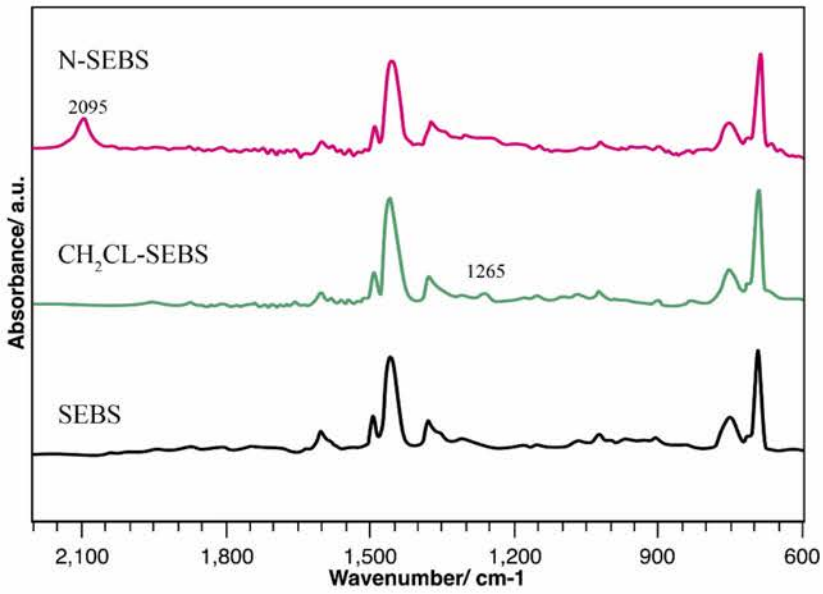

Figure 5-11 FT-IR spectra of SEBS and modified SEBS

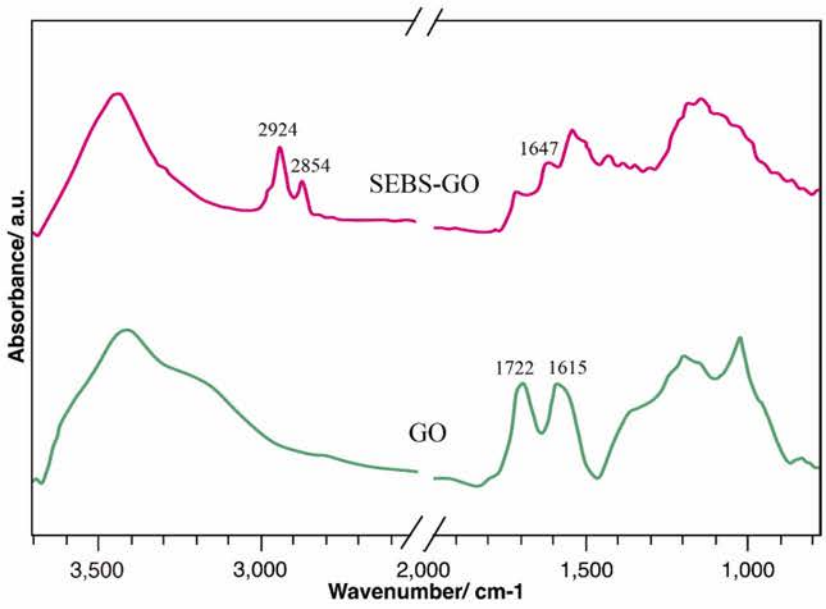

Figure 5-12 FT-IR spectra of GO and GO modified with SEBS

As can be seen from Figure 5-13, SEBS-GO has two weight loss peaks in TGA. The first peak at 473°C, corresponding to the thermal decomposition of SEBS, can also be

seen on the DTG curve of N-SBES shown in Figure 5-14. The second peak at 577°C, corresponding to the combustion of the carbon material, can also be seen on the DTG curve of GO shown in Figure 5-15. The first peak of SEBS-GO, that is, the thermal decomposition peak of SEBS, corresponds to a weight loss of 35%; i.e., the SEBS content in SEBS-GO is approximately 35 wt%. This value is higher than weight of the PS group on PS-GO (20 wt%),

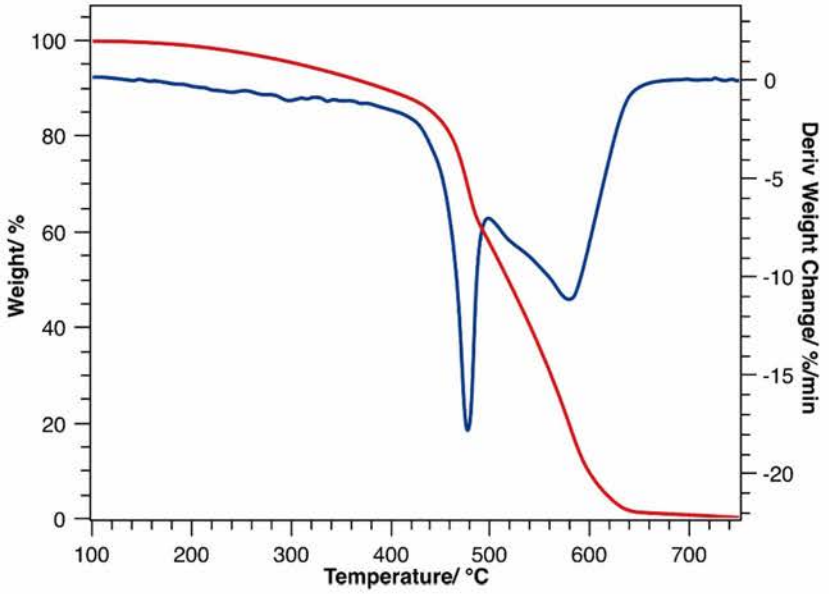

Figure 5-13 TGA and DTG curves of SEBS-GO

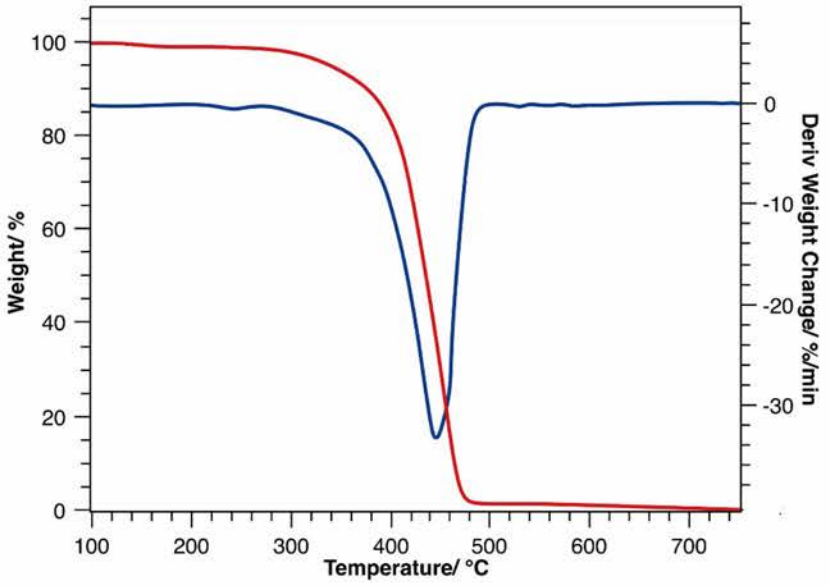

Figure 5-14 TGA and DTG curves of N-SEBS

which is probably due to the higher molecular weight of SEBS (about 170,000). We note that SEBS-GO has no weight loss peak near 200°C that corresponds to the thermal cracking of the oxygen-containing functional groups on GO. This result indicates that the reduction of GO occurred during the preparation of SEBS-GO and that this reduction may be solvent-induced thermal reduction.

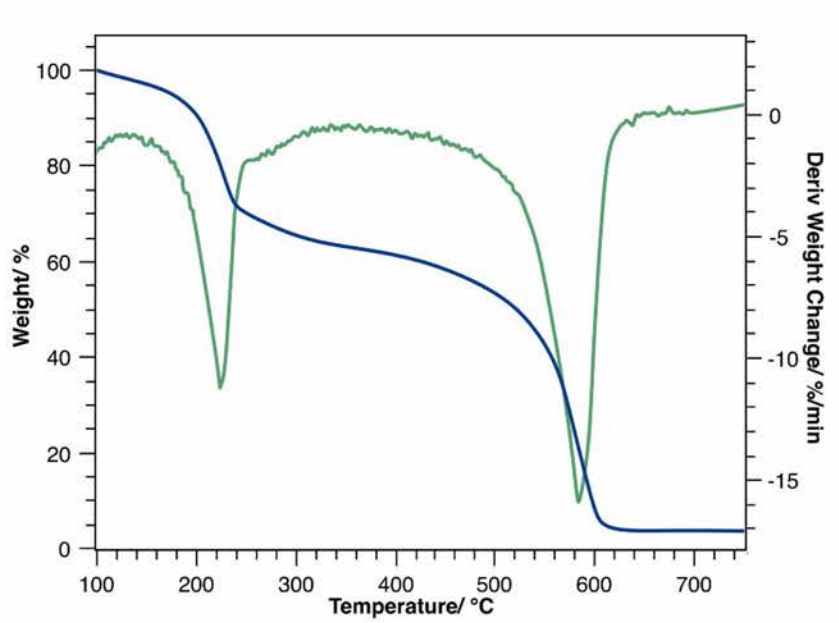

Figure 5-15 TGA and DTG curves of GO

In general, both oxidative modification and covalent modification introduce defects in graphite materials, and these defects are reflected well in Raman spectra. Figure 5-16 shows the Raman spectra of graphite, GO and SEBS-GO. In all samples, there are two peaks at 1350 and 1580 cm^{-1}. These two peaks are called the D band and G band, respectively, For graphite, the intensity ratio of the D band to the G band can be used to calculate the lattice size. The calculation was based on the formula $La(nm)=2.4\times10^{-10}\times\lambda^{4}\times(I_D/I_G)^{-1}$, where L_a is the lattice size and λ is the wavelength of excitation light (514 nm in this study). Based on the data in the figure, we can estimate that the crystal sizes of graphite, GO, and modified GO are 120.8, 21.3 and 17.1 nm, respectively. This result indicates that there are so many defects that the crystal size is greatly reduced. After SEBS was grafted onto GO, the number of defects increased, indicating that GO and SEBS have covalently bonded with each other.

Figure 5-17 shows the XRD patterns of graphite, GO, and SEBS-GO. Graphite has a strong diffraction peak at 26.5°. According to the Bragg equation, the interlamellar spacing of each layer in graphite can be calculated as 0.34 nm. At the same time,

compared with that of graphite, the diffraction peak of GO is obviously weakened, indicating that GO is more porous than graphite. However, SEBS-GO does not show any diffraction peak, indicating that all SEBS-GO is disordered.

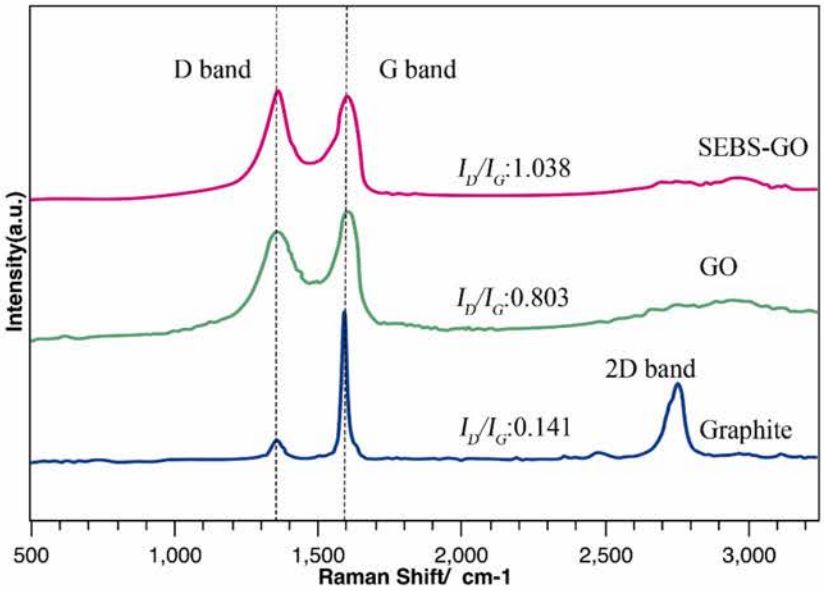

Figure 5-16 Raman spectra of graphite, GO and SEBS-GO

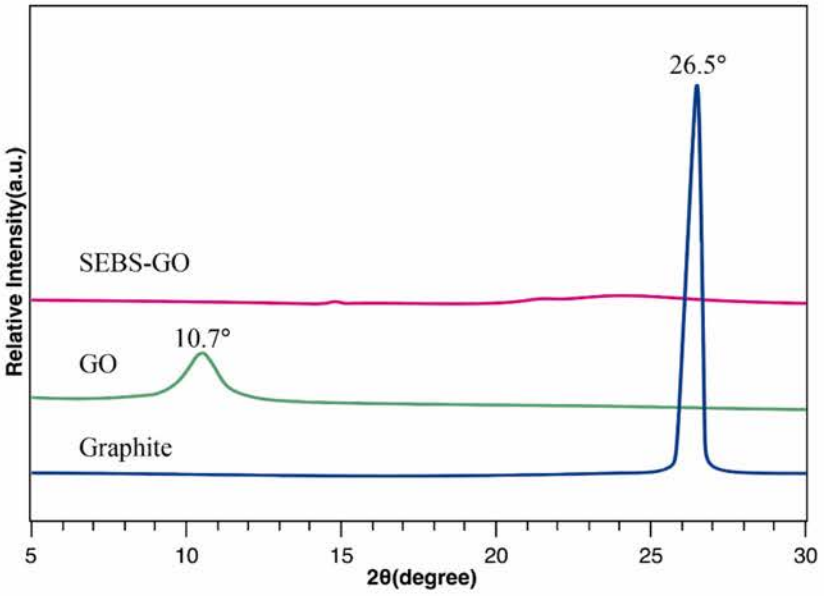

Figure 5-17 XRD spectra of graphite, GO and SEBS-GO

5.2.1.4. Structure and performance of polypropylene (PP) grafted onto GO (PP-GO)

The preparation route for polypropylene (PP) grafted onto GO (PP-GO) is shown in Figure 5-18. First, the epoxy group on GO undergoes a nucleophilic substitution

reaction with the amino group on diaminodiphenylmethane (MDA) to graft MDA onto GO. Then, the other amino group on MDA reacts with the acid anhydride on maleic anhydride-grafted polypropylene (MAPP) to form an amide group, achieving covalent grafting of PP chains onto GO. The product is modified PP-GO.

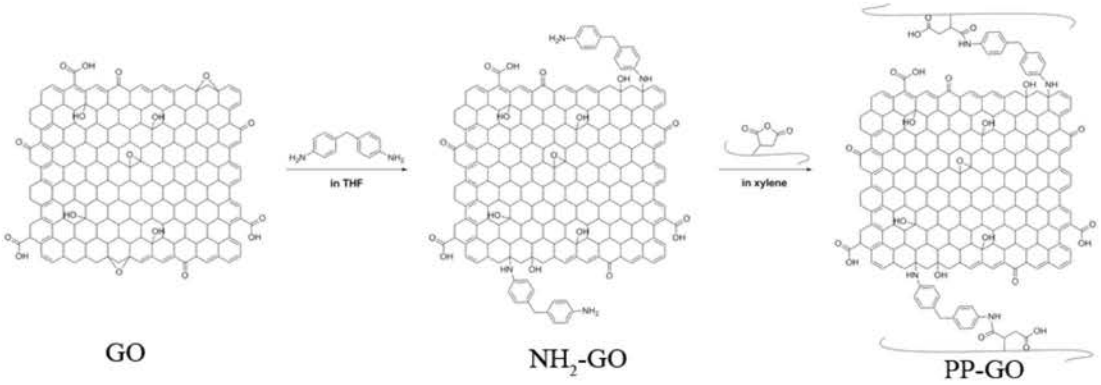

Figure 5-18 Strategy for covalently grafting PP chains onto GO

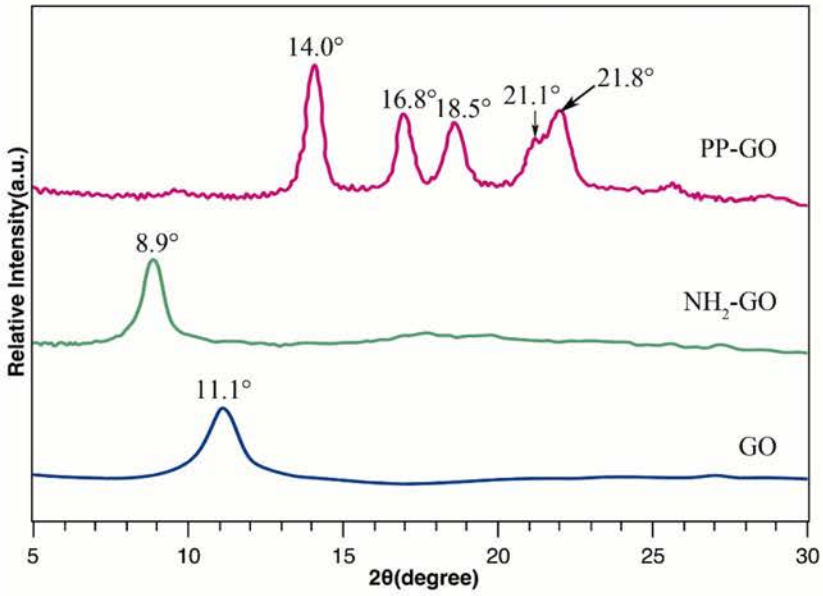

Figure 5-19 XRD patterns of GO, NH_2-GO, and PP-GO

Figure 5-19 shows XRD patterns of GO, NH_2-GO, and PP-GO. GO has a diffraction peak at 11.1°, which corresponds to a layer spacing of 0.80 nm. In general, GO and small molecules will undergo a nucleophilic substitution reaction, and the small molecules will be inserted into the layers of the film, causing the layer spacing to change. The XRD results of NH_2-GO confirm this conclusion. The diffraction peak at 8.9° corresponds to a layer spacing of 0.99 nm, demonstrating that MDA indeed underwent a nucleophilic substitution reaction with GO. However, after the reaction

between NH_2-GO and MAPP, the peak corresponding to the interlayer distance of GO disappeared, indicating that all the layer in PP-GO are disorganized. In place of this peak, peaks appeared at 14.0, 16.8, 18.5, 21.1 and 21.8°. These peaks correspond to the diffraction peaks of the α-crystal form of PP, indicating that the PP chains will still fold into their α-crystal form after being grafted onto GO.

FT-IR spectra can give us direct evidence for the covalent grafting of MAPP. The FT-IR spectra of GO, NH_2-GO and PP-GO are shown in Figure 5-20. GO has a peak at 1000-1150 cm^{-1}, which corresponds to the stretching vibration peak of C-O in the epoxy group. After the nucleophilic substitution reaction with MDA, the same peak in the spectrum of NH_2-GO became significantly wider. The nucleophilic substitution reaction produces C-OH and C-N bonds, and the stretching vibration of these two bonds will peak at 1000 ~ 1300 cm^{-1}, which will make this peak appear very wide. In addition, NH_2-GO showed two peaks at 2924 and 2860 cm^{-1}, corresponding to the stretching vibration peak of the methyl groups on MDA. For PP-GO, there are two peaks at 2924 and 2860 cm^{-1} that became large because there are a large number of methyl and methylene groups in the PP chain. In addition, there are three new peaks at 1653, 1572 and 1464 cm^{-1} in the spectrum of PP-GO. These three new peaks correspond to the C=O stretching vibration, N-H bending vibration and C-N stretching vibration in the amide bonds, respectively. The FT-IR data indicate that MAPP was grafted onto GO.

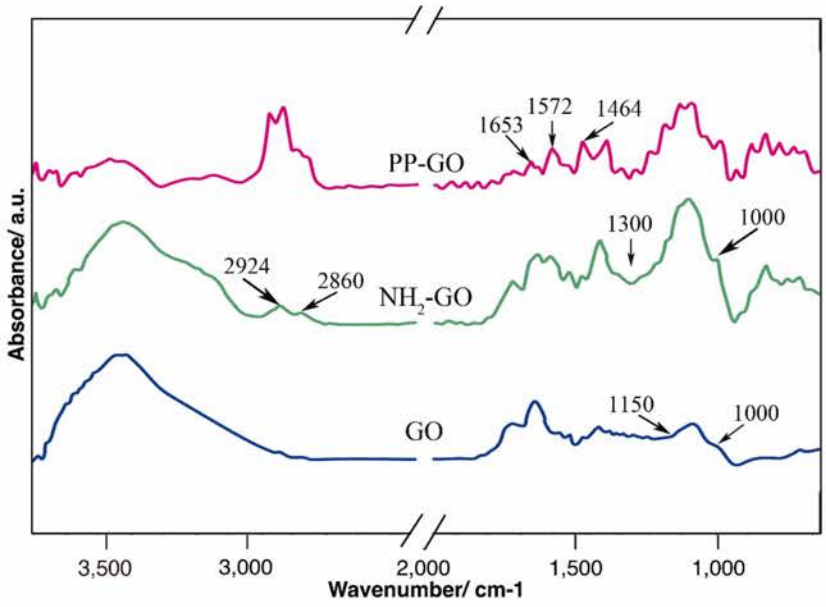

Figure 5-20 FT-IR spectra of GO, NH2-GO and PP-GO

To quantitatively determine the extent of grafting of the PP chain, we performed

TGA under nitrogen conditions. As can be seen from Figure 5-21, PP-GO has only one weight loss peak at 492°C. This weight loss peak, corresponding to the thermal decomposition of the PP chain, can also be seen on the DTG curve of MAPP (curve b). For PP-GO, this peak corresponds to a weight loss of 67 wt%, which means that 1 mg of GO was grafted with 2 mg of PP. The grafting efficiency of this method is very high. Importantly, the PP-GO weight loss peak at approximately 200°C, which corresponds to the thermal cleavage of the oxygen groups on GO, shows that the reduction of GO occurred during the preparation of modified PP-GO.

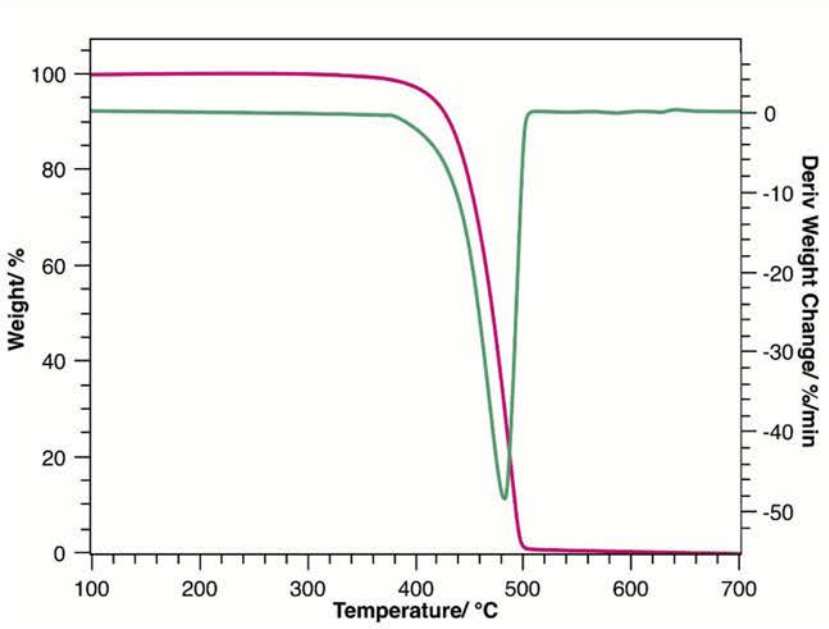

Figure 5-21 TGA and DTG curves of MAPP

5.2.2. Properties of graphene/natural rubber composites

5.2.2.1. Mechanical properties

The mechanical properties of rubber composites are shown in Table 5-1, and the corresponding stress-strain curves are shown above in Figure 5-22. It can be seen that as the loading of modified graphene increases, the 100% modulus, 300% modulus, tensile strength, tear strength and Shore A hardness of the composites are significantly increased.

Compared with Graphene-0, the Graphene-5 composites showed 100% and 257% increases in 100% modulus and 300% modulus. However, for composites, which filled with 5 parts of CB N330, the 100% Modulus was increased only 24% and the 300% Modulus increase only 40%. Therefore, the composites filled with the same content of

graphene achieved a more significant increase in tensile modulus.

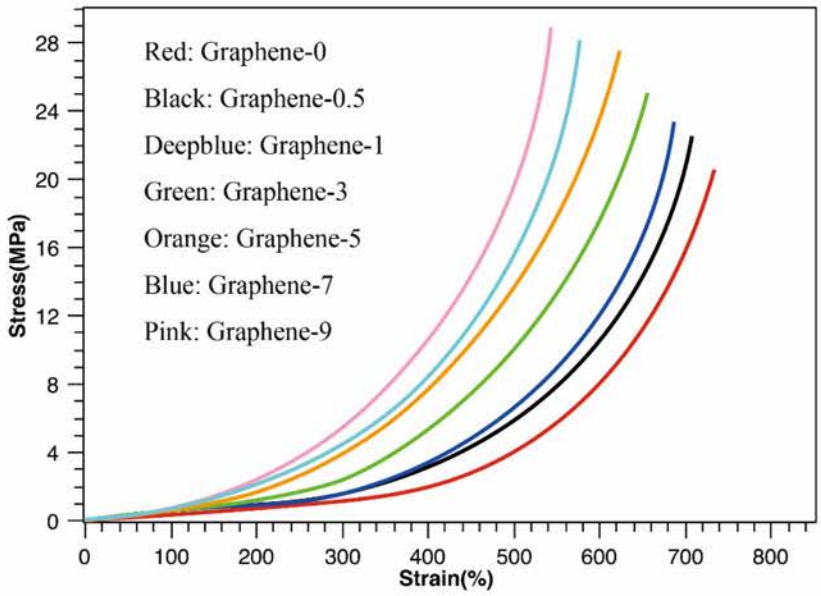

Figure 5-22 Stress-strain curves of graphene/natural rubber composites

Table 5-1 Mechanical properties of graphene/natural rubber composites

Samples	Graphene-0	Graphene-0.5	Graphene-1	Graphene-3	Graphene-5	Graphene-7	Graphene-9
100% Modulus (MPa)	0.7	0.8	0.9	1	1.3	1.4	1.5
300% Modulus (MPa)	1.4	2.0	2.3	3.5	5.1	5.3	5.5
Elongation at Break (%)	744	720	710	685	660	620	590
Tear Strength ($kN\ m^{-1}$)	26.4	29.3	31.7	38.9	46.9	48.6	49.9
Tensile Strength (MPa)	21.6	23.9	25.1	26.8	28.9	30.2	31.4
Shore A Hardness	35	37	39	45	48	49	50

Strain-induced crystallization (SIC) has a very important effect on the enhancement of natural rubber. We used the modified Mooney-Rivlin equation to investigate the effect of graphene on the SIC properties. According to the equation, we

convert the stress-strain curve to a modified Mooney-Rivlin curve to eliminate the finite elongation of the rubber molecular chains.

$$\sigma = 2\left(C_1 + \frac{C_2}{\lambda}\right)\left(\lambda - \frac{1}{\lambda^2}\right) f(\lambda) = 2\left(C_1 + \frac{C_2}{\lambda}\right) F(\lambda)$$

Equation 5-1

σ: nominal stress, λ: the draw ratio, C_1, and C_2: Mooney-Rivlin constants, $f(\lambda)$: the function of λ. The equation is as follows:

$$f(\lambda) \cong \left(1 + \frac{1}{3}\frac{\lambda^2}{\lambda_m^2}\right)$$

Equation 5-2

λ_m: maximum draw ratio at break. The transition of the $\sigma/F(\lambda)$ and λ^{-1} curves is mainly due to the SIC effect of natural rubber. The critical turning point λ_{up} of the draw ratio of SIC can be obtained by the following equation.

$$\lambda_{up}^3 = \frac{3\lambda_m^2 C_2}{2C_1}$$

Equation 5-3

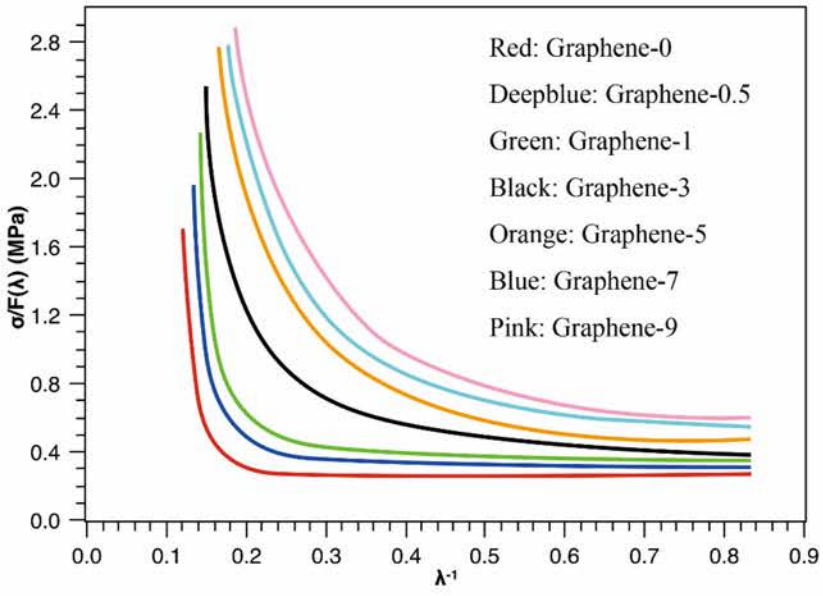

Figure 5-23 Modified Mooney-Rivlin curves of graphene/natural rubber composites

The relationship between $\sigma/F(\lambda)$ and λ^{-1} is shown in Figure 5-23. The corresponding C_1, C_2, and λ_{up} values are presented in Table 5-2. As the content of

modified graphene increases, we can see that the C_1 value gradually increases, indicating there is an increase in elastic modulus and crosslinking density. In addition, as the graphene content increases, the turning point gradually moves toward a high λ^{-1} (lower strain), and the critical λ_{up} value gradually decreases, indicating that the initial strain of SIC gradually decreases. Thus, the addition of modified graphene improves the SIC ability of natural rubber.

Table 5-2 Values of C and λ obtained from modified Mooney-Rivlin plots

Samples	C_1 (MPa)	C_2 (MPa)	λ_{up}
Graphene-0	0.143	0.067	3.69
Graphene -0.5	0.163	0.070	3.51
Graphene -1	0.215	0.079	3.29
Graphene -3	0.258	0.078	3.03
Graphene -5	0.295	0.073	2.77
Graphene -7	0.310	0.070	2.73
Graphene -9	0.320	0.069	2.72

5.2.2.2. Hysteresis loss

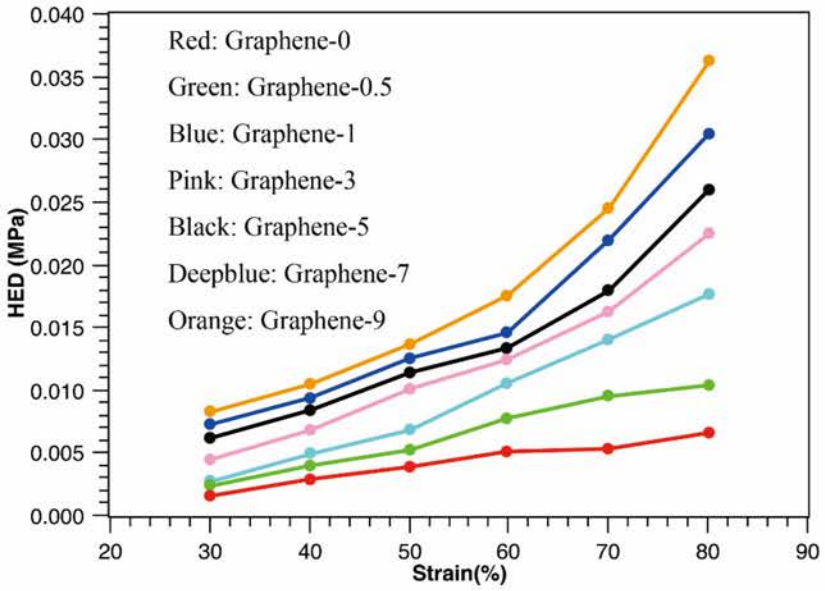

Figure 5-24 Hysteresis energy density for graphene/natural rubber composites

The viscoelastic dissipation mechanism is important to fatigue properties. In

addition, hysteresis loss has an important effect on crack propagation; i.e., hysteresis loss can improve anti-crack-propagation performance by dissipating energy. However, hysteresis loss can also adversely affect dynamic crack propagation because it is translated into heat energy. However, heat energy cannot dissipate quickly, and the increase in heat will accelerate the expansion of fatigue cracks. The different hysteresis energy density (HED) values of the composites are shown in Figure 5-24. As a typical example, Table 5-3 lists the HED and H (%) values at 50% strain. The results show that both the HED and H (%) of the composites significantly increase with the graphene content. Compared to Graphene-0, the Graphene-5 composites show approximately 3.5 and 1.9 times increases in HED and H (%), respectively, at 50% strain. A significantly increase in hysteresis loss will have an adverse effect on dynamic fatigue performance.

Table 5-3 Hysteresis energy density and hysteresis loss

Samples	Graphene-0	Graphene-0.5	Graphene-1	Graphene-3	Graphene-5	Graphene-7	Graphene-9
HED (MPa)	0.006	0.007	0.008	0.016	0.018	0.020	0.021
H (%)	4.53	4.91	5.32	8.02	8.41	8.62	8.71

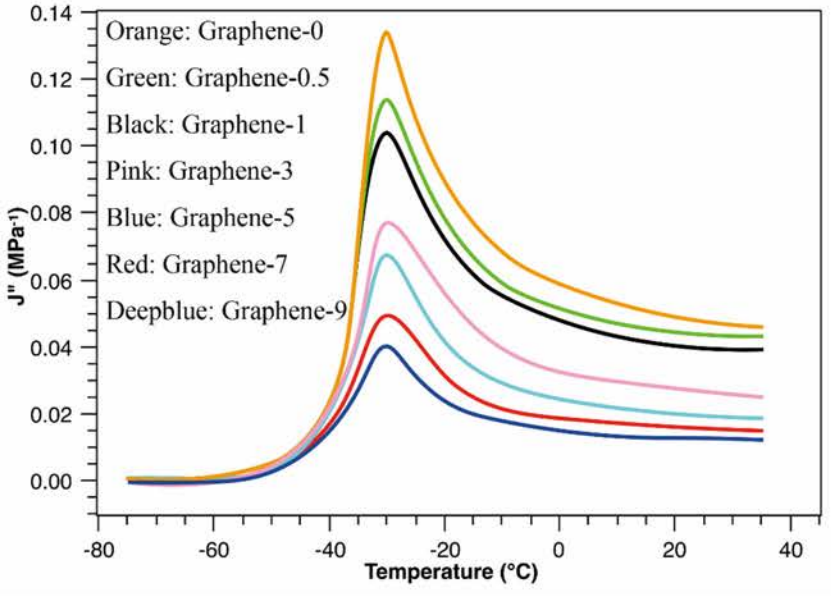

Figure 5-25 Loss compliance/temperature of graphene/natural rubber composites

HED and H (%) reflect the viscoelastic hysteresis loss of rubber composites. In contrast, the loss compliance J" indicates the hysteresis behavior at the crack tip under

dynamic conditions. The J" values of the rubber composites at different temperatures were measured by a dynamic mechanical thermal analyzer (DMTA).

$$G(v) = G_0\left[1+\frac{2}{\pi}E_0\int_0^{2\pi v/a} d\omega \frac{F(\omega)}{\omega}J''\right]^{-1}$$

Equation 5-4

In the above Equation 5-4, F(ω) is a function of frequency ω. Thus, at the same crack propagation rate, more energy dissipation is required at the crack tip. The relationship between the J" value of the rubber composites and the temperature is shown in Figure 5-25. At room temperature, the J" value gradually decreases as the graphene content increases. We can see that the Graphene-7 and Graphene-9 composites have significantly lower J" values than the other composites. Therefore, the hysteresis energy near the crack tip increases significantly with the graphene content. In addition, the significantly increased hysteresis energy is mainly attributed to the interfacial frictional slippage between the graphene sheet and natural rubber molecular chains, which adversely affects the dynamic fatigue performance.

5.2.2.3. Dynamic fatigue properties

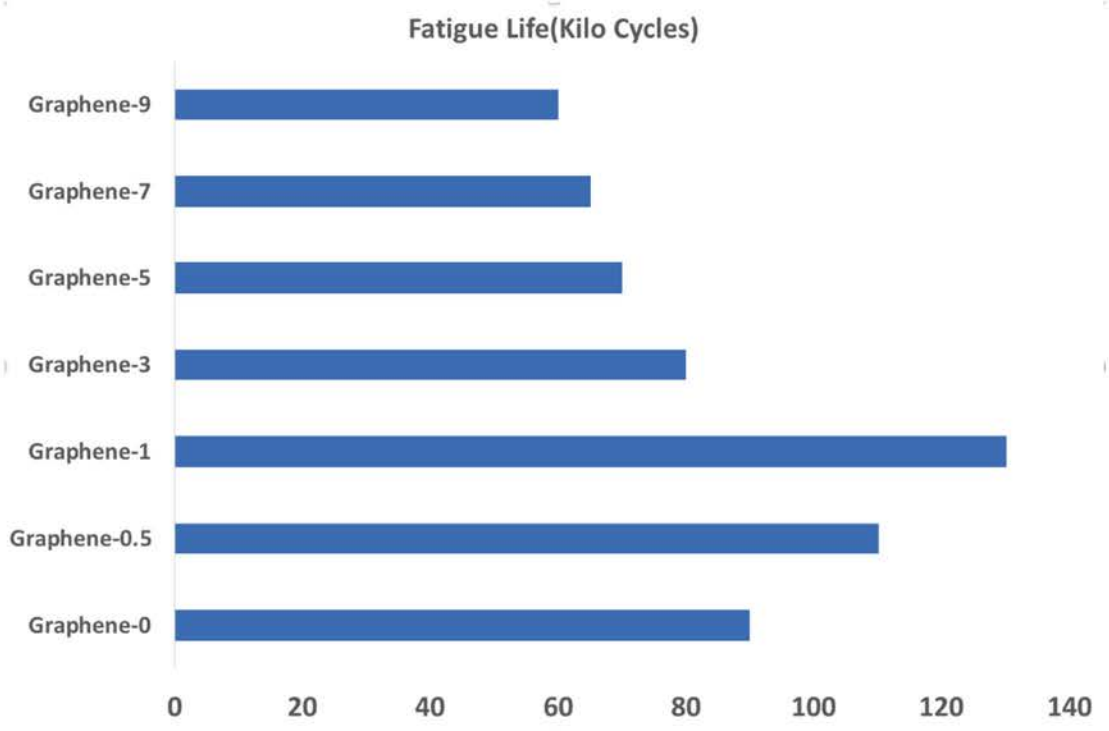

Figure 5-26 Fatigue lifetime of graphene/natural rubber composites

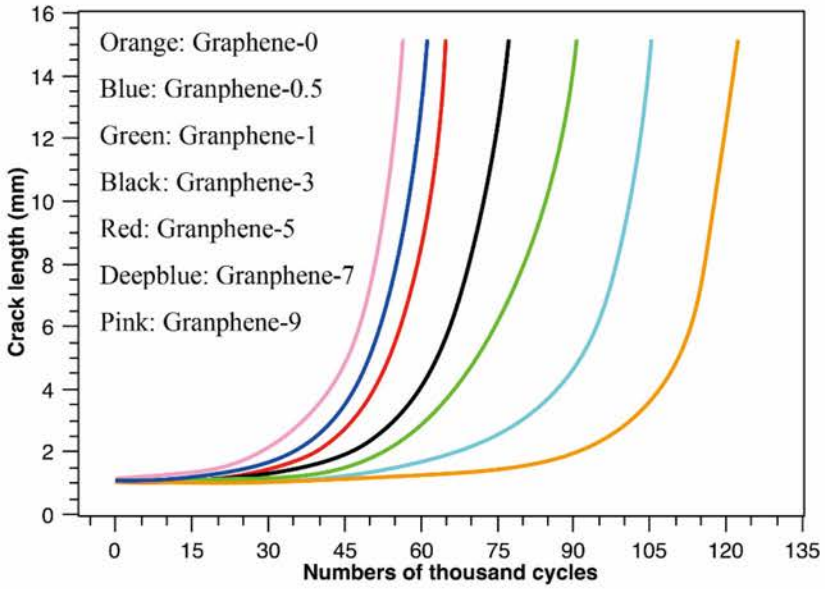

Figure 5-27 Crack length/fatigue cycles

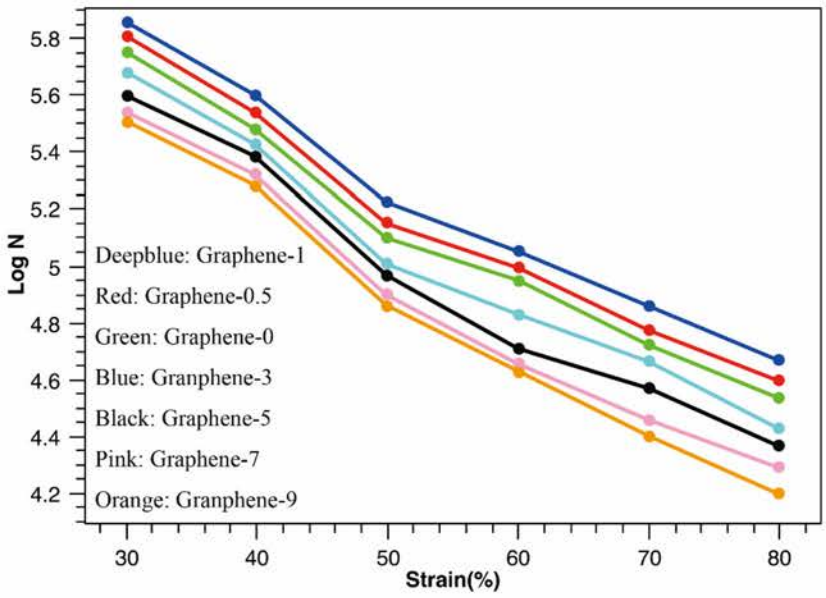

Figure 5-28 Fatigue lifetimes N of graphene/natural rubber composites under different strains

The dynamic fatigue behavior of rubber composites in the strain range of 30% ~ 80% is studied, and the results are shown in Figure 5-26 and Figure 5-27. We observed in Figure 5-28 and Figure 5-29 that the Graphene-1 composites exhibited the best fatigue performance and the lowest da/dN values under all strain conditions. This result indicates that the Graphene-1 composite has the best fatigue resistance.

For example, compared to pure natural rubber, the natural rubber composite filled with 1 part modified graphene shows a 38% increase in the fatigue life at 50% strain and a 40% decrease in the da/dN value. It is unusual for such a low filler loading (1 part) to achieve such a significant improvement in fatigue resistance. Under constant strain conditions, the Graphene-3, Graphene-5, Graphene-7, and Graphene-9 composites exhibit better fatigue resistance than natural rubber, which is consistent with the previous crack propagation test results. If we want to obtain the best fatigue crack propagation resistance, we should determine the optimal composite formula. If the filler loading exceeds the optimum formula, the fatigue resistance will rapidly decrease. Based on the above results, we consider the tearing energy and hysteresis loss to explore the failure mechanism of the rubber composites.

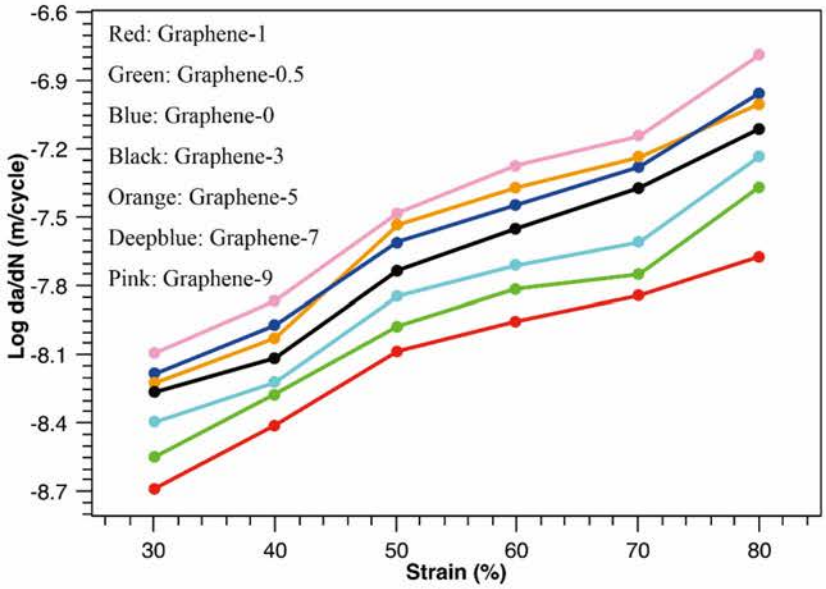

Figure 5-29 Crack growth rates of graphene/natural rubber composites

We find that the fatigue crack propagation resistance can be controlled by the input tearing energy. As an example, the tearing energy at 50% strain is shown in Table 5-4. The results shows that when the graphene content increases, the tearing energy input also significantly increases. Under 50% strain, compared to pure natural rubber, the Graphene-3 composite had a 55% increase in tearing energy. The crack growth rates for different tearing energies are shown in Figure 5-30. Under constant tearing energy conditions, pure rubber exhibited the weakest antifatigue properties, and the Graphene-1 composite showed the strongest antifatigue properties. We can also compare the fatigue properties of the composites from an energy point of view.

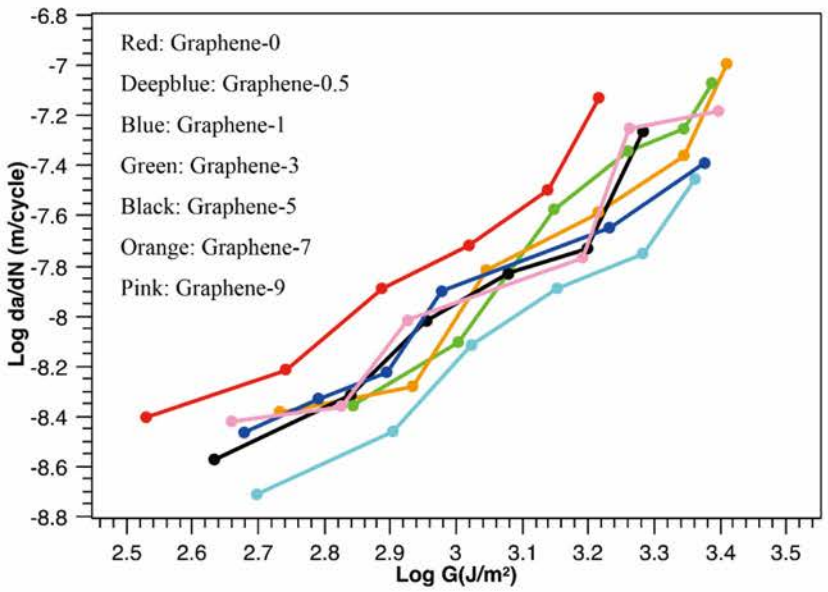

Figure 5-30 Fatigue crack growth

Table 5-4 Tearing energy of rubber composites under a strain of 50%

Samples	Graphene-0	Graphene-0.5	Graphene-1	Graphene-3	Graphene-5	Graphene-7	Graphene-9
Tearing Energy G(J • m^{-2})	812	953	1112	1254	1405	1503	1543

5.2.2.4. J-integral test

The anti-crack properties of the graphene/natural rubber composites are characterized by the J-integral test. In addition, the J-integral curve is shown in Figure 5-31. The corresponding J_{IC} and T_R values are given in Table 5-5. We can see that under the same crack-tip opening displacement (CTOD) value, the corresponding J-integral value will increase with the loading of graphene. The significant increases in J_{IC} and T_R indicate that graphene can significantly improve the anti-crack performance of composites. We can recognize that the improvement in crack propagation resistance is mainly due to the passivation of the crack tip, which is because of tensile orientation and tensile crystallization.

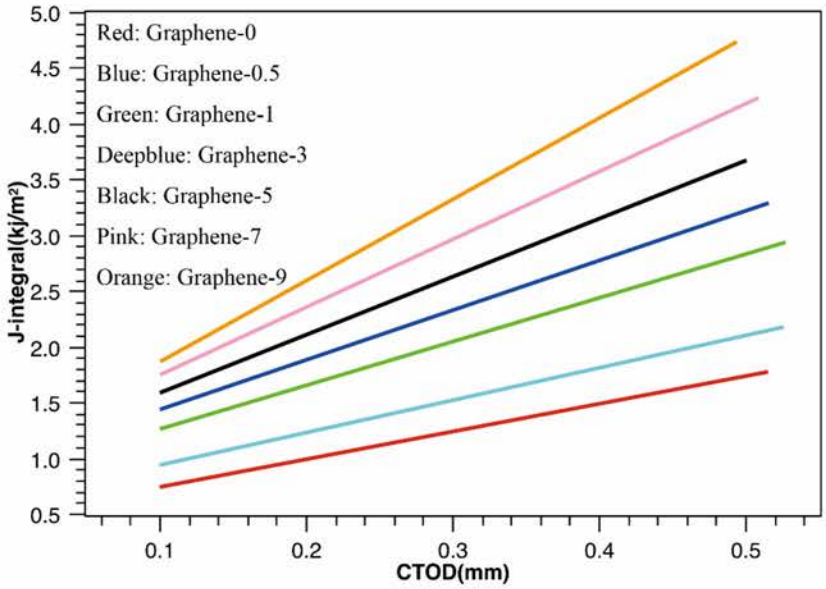

Figure 5-31 J-value versus crack-tip opening displacement

Table 5-5 Critical value J_{IC} and tearing modulus T_R of graphene/natural rubber composites

Samples	Graphene-0	Graphene-0.5	Graphene-1	Graphene-3	Graphene-5	Graphene-7	Graphene-9
J_{IC}(kJ •m^{-2})	0.77	0.92	1.22	1.57	1.97	2.03	2.11
T_R(MPa)	2.94	3.27	4.73	6.14	7.73	7.83	8.03

5.3. Summary

This chapter focuses on the covalent modification of graphene and GO to improve their surface activity and solvent dispersion.

(1) Using the carboxyl groups on graphene, performing an amidation reaction with the amino group on ODA, and then grafting ODA onto graphene. The resulting Modified-Graphene-1 can be uniformly and stably dispersed in nonpolar solvents such as xylene.

(2) In this chapter, polymers were also grafted onto GO. First, we connect an alkynyl group to graphene, Then, we obtain Modified-GO-1 grafted with an azido-modified polymer by a cycloaddition reaction. This method can graft polymers with certain structures onto GO, and the reaction has very high efficiency. We also prepared different modified GO derivatives by grafting GO with PP, PS, SEBS and MAPP.

In this chapter, a rubber composite material was then prepared by using modified

graphene. Modified graphene is uniformly dispersed in the natural rubber matrix. Compared to pure natural rubber, the rubber composites have significantly improved in mechanical properties, crack initiation resistance and crack propagation resistance. In this chapter, we also studied the dynamic fatigue performance of the composites. The Graphene-1 composite shows the strongest crack propagation resistance, indicating that there is an optimal graphene filling amount for the composite in terms of its dynamic fatigue. Graphene-3, Graphene-5, Graphene-7 and Graphene-9 have very weak dynamic fatigue performance due to the increased graphene loading, which causes a rapid increase in hysteresis loss.

Chapter 6. Synergistic Reinforcing Effect Between Carbon Nanomaterials

6.1. Introduction

The distribution of the local strain field is closely related to the crack propagation behavior of composites. High-modulus filler particles will lead to local stress concentration and strain amplification effects, which will significant affect the properties of composites. Therefore, studying the distribution of the local strain field is necessary [192-194].

Many factors have been proven to affect the fatigue properties of rubber composites. Some of the most important factors that significant affect the fatigue properties of composites include force loading, viscoelasticity and composites formulations. Different fillers have different particle sizes, specific surface areas, shape factors, and surface activities. These factors will have different effects on the failure behavior of rubber composites. Recently, due to their excellent reinforcing efficiency, carbon nanotubes (CNTs) and graphene have attracted extensive interest from academic. Fillers with a high shape factor have been found to tend to orient along the tensile direction, which will increase the passivation, deflection, and branching at the crack tip. Such behavior will improve the crack growth resistance of composites [195-197].

In this chapter, we prepared natural rubber composites with same hardness and different carbon nanofillers. The formulas and components are shown in Table 6-1

The J-integral was used for characterizing fatigue performance. In addition, the dynamic fatigue test is used to study the dynamic fatigue resistance of the composites. The energy input and hysteresis losses of the rubber composites were analyzed. The purpose of this chapter is to explore the effect of carbon nanofillers with different shape factors on the mechanical properties and fatigue resistance of rubber composites and to determine whether there is synergistic behavior between different fillers.

Table 6-1 Formulas of natural rubber composites

Samples	NR-0	Graphene-3	CNT-3	G-C-1	G-C-3
Graphene	0	3	0	1	3
MWCNTs	0	0	3	1	3
Natural rubber	100	100	100	100	100
Stearic Acid	2.1	2.1	2.1	2.1	2.1
Solid Wax	1	1	1	1	1
Zinc Oxide	6	6	6	6	6
Sulfur	2	2	2	2	2

6.2. Results and discussion

6.2.1. Carbon nanofiller network

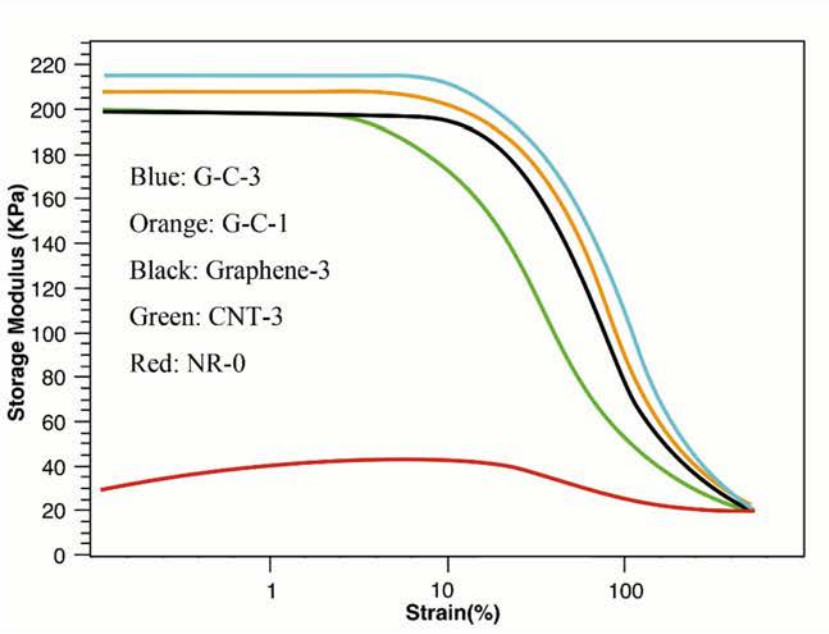

Figure 6-1 Shear storage modulus of different composites

The shear storage modulus of different composites made with different carbon nanofillers is shown in Figure 6-1. It can be seen that all of composites, namely, G-C-3, G-C-1, CNT-3, and Graphene-3, exhibit a similar Payne effect, indicating that all the composites have same filler network strength.

6.2.2. Vulcanization and mechanical properties

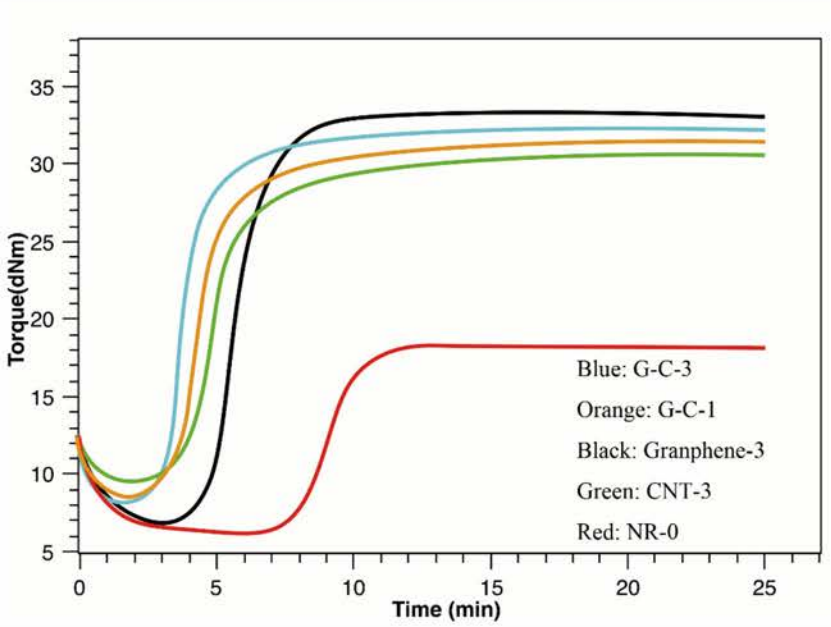

Figure 6-2 Vulcanization curves of NR composites

The vulcanization curves and vulcanization properties of the five natural rubber composites are shown Figure 6-2 and Table 6-2. We can see that as the amount of carbon nanofiller increases, the scorch time and optimum vulcanization time are significantly reduced, and the vulcanization of natural rubber is promoted. The lowest torque and highest torque for the G-C-1, G-C-3, CNT-3, and Graphene-3 composites are approximately same, which means that the four composites have the same modulus and crosslink density.

Table 6-2 Vulcanization properties of NR composites

Samples	NR-0	G-C-1	G-C-3	CNT-3	Graphene-3
Scorch time t_{10} (min)	8.1	2.4	2.6	3.5	4.9
Optimum cure time t_{90} (min)	11.4	6.1	6.3	7.4	8.4
M_L (dNm)	6.7	7.4	7.8	8.6	7.4
M_H (dNm)	20.9	31.1	32.5	31.2	33.2
$\triangle M$ (dNm)	14.2	24.6	24.7	22.6	25.8

We note that the natural rubber composites filled with two types of carbon nanomaterials have the same hardness (both 52, Table 6-3). The reason for the rubber composites having the same hardness is that the improvement in the performance of the

commercial rubber product is based on the same hardness. Compared with pure natural rubber, the natural rubber composites to which carbon nanomaterials are added have significantly improved mechanical properties (Table 6-3).

Table 6-3 Mechanical properties of natural rubber composites

Samples	NR-0	G-C-1	G-C-3	CNT-3	Graphene-3
100% Modulus /MPa	0.8	1.2	1.4	1.5	1.5
300% Modulus /MPa	1.7	5.6	5.9	3.7	5.4
Tensile strength/MPa	20.8	27.9	28.9	23.8	27.7
Tear strength/kN·m^{-1}	28.9	51.5	54.5	46.7	41.4
Elongation at break/%	715	663	656	662	651
Shore A hardness	42	52	52	52	52

Although the amount of fillers in the CNT-3 and Graphene-3 composites is far less than that in the G-C-3 composite, their 100% set stress and hardness are almost the same. This result shows the excellent enhancement efficiency of one-dimensional CNTs and two-dimensional graphene. Rubber products usually work in the 100% strain range. Therefore, the fact that the 100% set stress is the same shows that the energy input during crack propagation under constant strain is also the same. The G-C-3 composite has the highest tensile stress in the high-strain range and the best tensile and tear strength. The other rubber composites exhibit almost the same elongation at break.

6.2.3. Energy input and energy dissipation during crack propagation

The energy input can directly affect the crack propagation properties of rubber composites. We find that for pure shear specimens (PSSs) under a constant strain, the J-integral and tearing energy of all the composites are independent of the crack length. This result is different from the SNTS experiment. As shown in Figure 6-3 and Figure 6-4, compared to pure natural rubber, the other four rubber composites have almost the same J-integral value and tearing energy at any constant strain. For the fracture mechanics tests, we can observe that when the three filled specimens are pulled to the same strain, the input J-integral values are also the same. For the dynamic fatigue test under constant tearing energy conditions, such as 0.5 kJ/m^2, the four rubber composites circulate continuously under almost the same strain conditions.

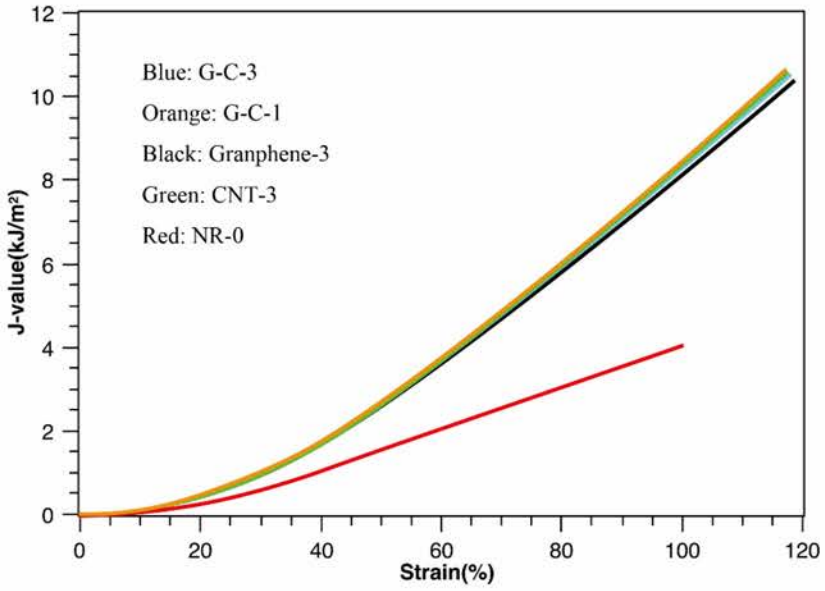

Figure 6-3 *J*-integral value of the natural rubber composites

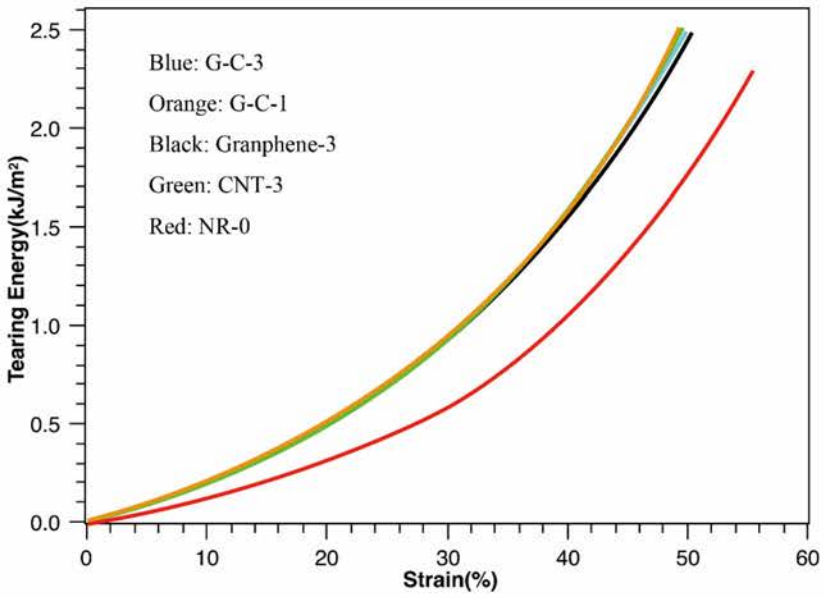

Figure 6-4 Tearing energy of the natural rubber composites

For rubber composites, we know that hysteresis loss is one of the most important factors, as it affects dynamic fatigue performance. In addition, all of the dynamic energy will turns into heat energy. As a result, heat energy will have an adverse effect on the dynamic fatigue properties of rubber composites. The hysteresis energy density (HED) is used to characterize the dynamic hysteresis loss of natural rubber composites. The cyclic stress-strain curve at a tearing energy of 1.5 kJ/m^2 is shown Figure 6-5.

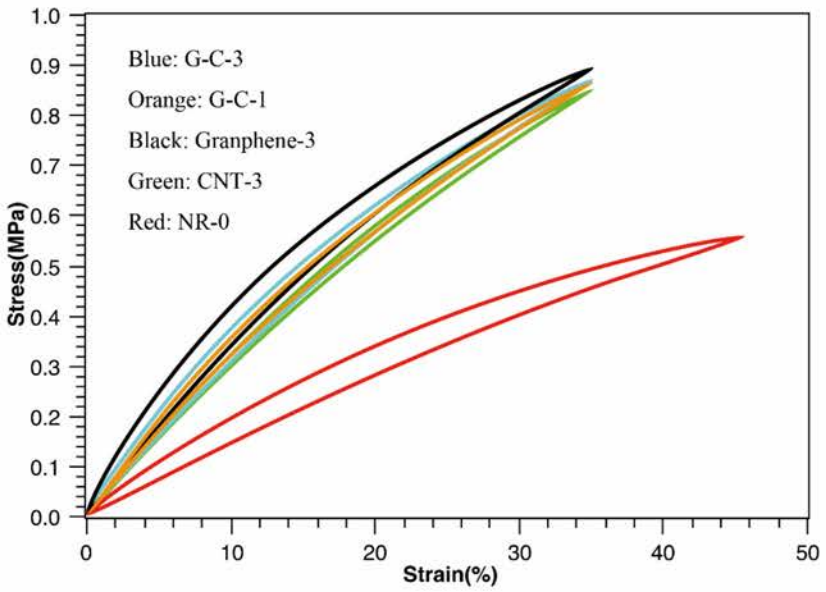

Figure 6-5 Cyclic stress-strain curves of natural rubber composites

The HEDs calculated for different tearing energies are listed in Table 6-4. It can be seen that at any tearing energy, the CNT-3 composite always shows a higher HED than the other composites. The significantly higher HED of the CNT-3 composite is mainly caused by the weaker interfacial interaction between the CNTs and natural rubber matrix. The slippage of CNTs increases the internal friction and hysteresis loss, resulting in significant heat production and accumulation and thereby reducing the dynamic fatigue properties of the CNT-3 composites.

Table 6-4 HED for different tearing energies

	0.6 kJ/m^2	1.2 kJ/m^2	1.8 kJ/m^2	2.4 kJ/m^2
Graphene-3	6.7	12.8	18.1	24.5
CNT-3	7.7	15.1	20.7	29.1
G-C-1	6.1	12.2	18.1	22.7
NR-0	3.2	6.3	8.7	10.9
G-C-3	7.9	13.3	20.6	25.6

6.2.4. Crack initiation/crack propagation resistance

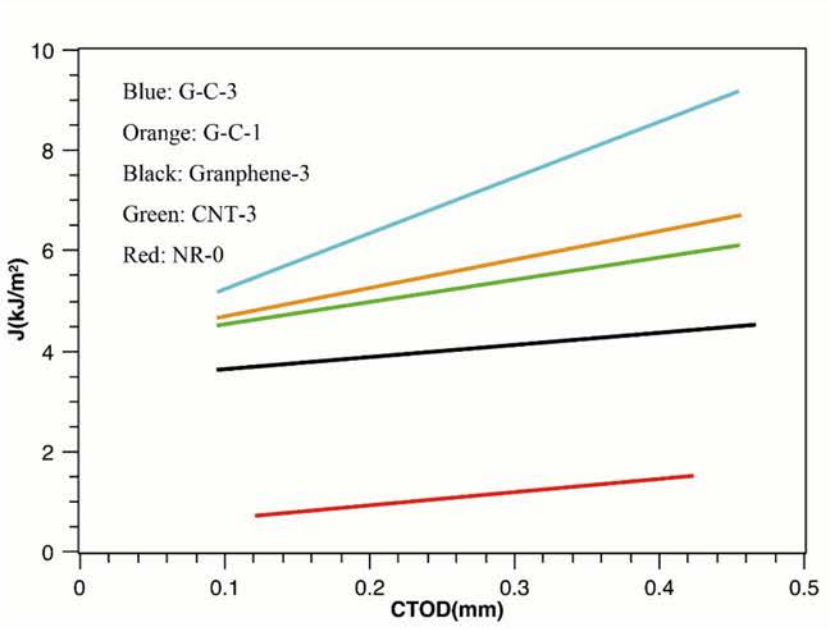

Figure 6-6 *J-CTOD* relationships of natural rubber composites

J-integral tests are used to investigate the crack initiation and crack propagation resistance of natural rubber composites. As previously described, the J-integral J_{IC} is used for characterizing the anti-crack performance and T_R. As shown in Figure 6-6, we noticed that when the crack-tip opening displacement (CTOD) is the same, the G-C-3 composite has the highest J-integral value, followed by the G-C-1, CNT-3 and Graphene-3 composites. In addition, when J-integral value is same, the G-C-3 composite has the lowest CTOD value.

Table 6-5 J_{IC} and T_R of natural rubber composites

Samples	NR-0	Graphene-3	CNTs-3	G-C-1	G-C-3
J_{IC}/kJm^{-2}	0.84	3.80	4.47	4.78	5.18
T_R/MPa	2.40	3.08	5.17	8.42	10.42
R^2	0.97	0.99	0.99	0.99	0.99

At the same time, the critical J-integral J_{IC} values (Table 6-5) show that the G-C-3 composite exhibits the best crack initiation performance, followed by the G-C-1, CNT-3 and Graphene-3 composites. We can also find that pure natural rubber has the lowest crack initiation resistance. We can see the J-integral value and CTOD show a linear correlation. The tear modulus T_R is listed in Table 6-5. We know that composites with

higher T_R value have better crack propagation resistance. We also note that the law of crack propagation resistance is consistent with crack initiation. The J-integral test showed that the G-C-3 composite exhibited the best crack initiation and crack propagation resistance

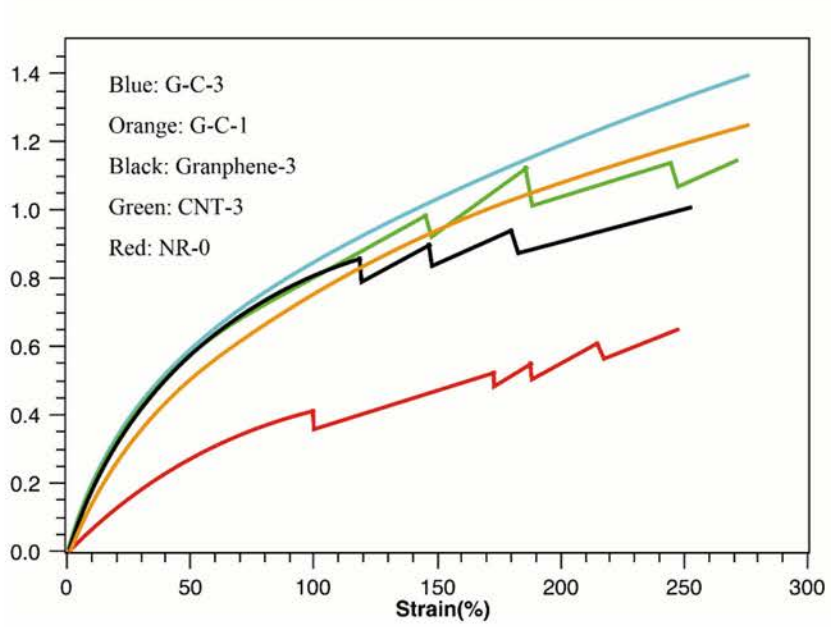

Figure 6-7 Typical stress-strain curves for PSSs

The stress-strain curve of precut specimens is used to indirectly characterize the anti-crack-propagation properties. Typical curves are shown in Figure 6-7. In the process of uniaxial stretching, rapid crack propagation will occur under a critical strain, which will result in a sudden decrease in stress, as shown in Figure 6-7. It is easy to understand that a higher critical strain indicates better crack propagation resistance. The critical strains of NR-0, Graphene-3, and CNT-3 are 100%, 125%, and 150%, respectively. However, there is no rapid stress reduction in the stress-strain curve of the G-C-3 and G-C-1 composites. This results indicates that the G-C-3 and G-C-1 composites are much superior to the other composites in anti-crack-propagation performance.

6.2.5. Strain distribution and amplification

The maximum strain at the crack tip of the sample is shown in Figure 6-8. It can be seen that there is a linear relationship between the maximum strain and overall strain. The G-C-3 composite exhibits higher crack-tip strain amplification levels than the other composites. At the same time, nonfilled pure natural rubber (NR-0) also exhibits

relatively weak strain amplification effects due to the crystallization effect. The G-C-3 composite has strongest strain amplification effect, which is mainly attributed to it having the highest filler loading. In addition, the results for the G-C-3 composite indicate that there will be more polymer chains that can withstand the input energy, which will help improve the crack propagation resistance.

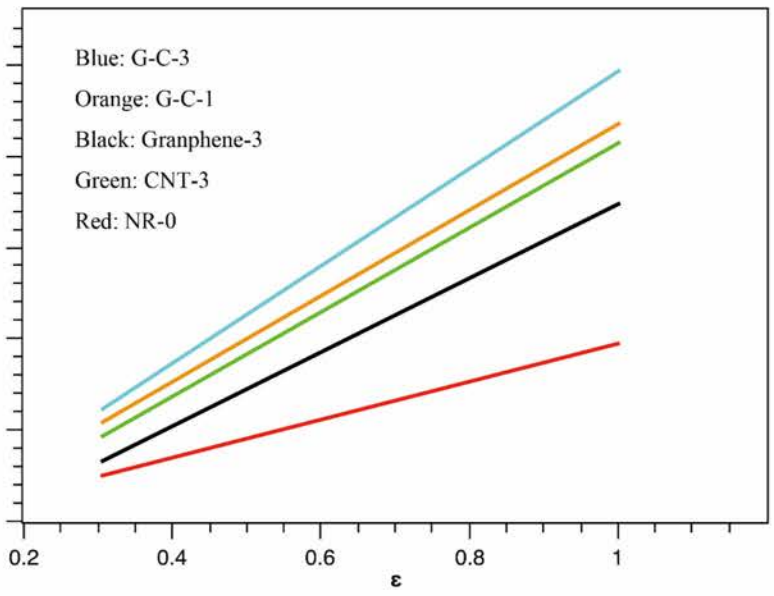

Figure 6-8 Different strains of NR composites

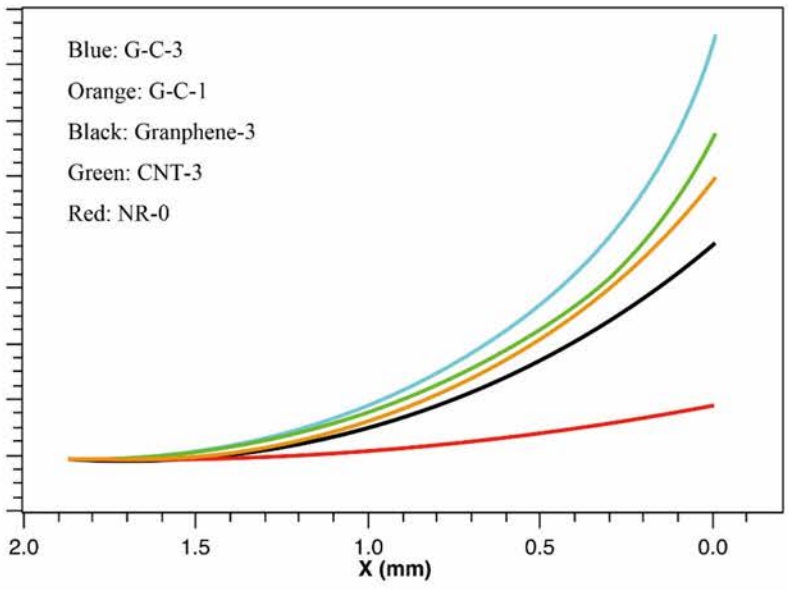

Figure 6-9 Crack direction for natural rubber composites

The distribution of strain for the natural rubber composites is shown in Figure 6-9.

The figure shows that the presence of singular strain regions. We note that the G-C-3 composite shows higher strain amplification and has a higher amplification effect than the other composites. The length of the region affected by the strain amplification effect of the G-C-3 composite is approximately 1.6 mm. As shown above, all three rubber composites exhibit almost the same energy input during crack propagation. However, the strain amplification area of the G-C-3 composite, which is the largest, dissipates the most energy, resulting in a reduction in energy for molecular chain breakage and crack propagation. As a result, we can see the excellent crack propagation resistance of G-C-3 composites.

6.2.6. Dynamic fatigue properties

Table 6-6 Fatigue crack growth rate

	0.6 kJ/m^2	1.2 kJ/m^2	1.8 kJ/m^2	2.4 kJ/m^2
NR-0	28.8	43.8	59.9	82.6
Graphene-3	17.6	29.3	44.6	56.8
CNT-3	13.4	21.6	37.9	48.6
G-C-1	8.2	18.2	20.6	27.6
G-C-3	9.2	15.2	26.6	34.6

The dynamic fatigue properties were also studied. In addition, the fatigue crack propagation rate at tearing energies of 0.5, 1.0, 1.5, and 2.0 kJ/m^2 is shown in Table 6-6. We note that the da/dN value also increased with increasing tearing energy. The G-C-3 composite exhibited the lowest da/dN value under any tearing energy condition, indicating that it has the best dynamic crack propagation resistance, followed by G-C-1, CNT-3 and Graphene-3. We can also see pure natural rubber NR-0 has the weakest dynamic crack propagation resistance. The dynamic fatigue result is consistent with the crack propagation result.

6.3. Summary

In this chapter, the effects of different carbon nanomaterials used as a filler for natural rubber composites were studied. All composites have the same hardness. In addition, mechanical blending ensures uniform dispersion of the filler in the natural rubber matrix. The results showed that the G-C-3 composite, which contains of mixture of CNTs and graphene, shows the best fatigue resistance performance, followed by G-C-

1, CNT-3 and Graphene-3. In addition, we found that the energy input is not the cause of the difference in crack propagation resistance. The CNT-3 composite has the highest hysteresis loss and the lowest dynamic fatigue performance. In addition, the crack distribution shows that the G-C-3 composite exhibits the best strain amplification effect, which will greatly enhance the dissipation of the local input tearing energy and improve the crack propagation resistance.

Chapter 7. Conclusions

In this study, we improve the antifatigue performance of natural rubber as a shock absorbing material. Different kinds of natural rubber composites are prepared by a mechanical blending method. We also prepare different surface-modified CNTs and graphene to improve their dispersion in a rubber matrix. We search for the best way to modify the carbon nanomaterials and confirm the best formula for rubber composites. By testing the crystallization and mechanical properties of the rubber composites, we determine the influence of the loading amount on the fatigue resistance. The findings are as follows:

1) Surface modification of MWCNTs was achieved by grafting them with carboxyl, hydroxyl, carbonyl and amide groups by acidification and amination. The acidification conditions were as follows: 1 g of MWCNTs were dissolved in 80 mL of nitro-sulfuric acid (volume ratio of 3:1) at 50°C, and oxygen-containing functional groups were grafted onto the MWCNTs after 2 h of ultrasonication. The carboxyl content was characterized by acid-base titration. The amination conditions were as follows: 0.3 g of Modified-MWCNTs-2 were reacted with 72 mL of ethylenediamine for 48 h; this process enabled the grafting of amide groups. Then, the MWCNTs will disperse uniformly.

2) The amidation reaction can add carboxyl groups to graphene. In addition, alkyl groups improve the lipophilicity of graphene. GO was modified by propargyl alcohol, and these alkyne groups were used to graft polymers onto graphene or GO. This study grafted different polymers onto graphene or GO, such as PS, SEBS, and MAPP.

3) A series of carbon nanomaterial/natural rubber composites were prepared by using a two-roll miller. The results show that functional groups improve the compatibility between the filler (CNTs and graphene) and the natural rubber matrix. Thus, carbon nanomaterials can disperse uniformly in the rubber matrix. The results show that the addition of modified carbon nanomaterials does not change the chemical structure of natural rubber. However, due to the addition of carbon nanomaterials, the strength and fatigue resistance of natural rubber composites are improved greatly.

4) This research finds that combining CNTs or graphene with a conventional filler such as CB will greatly improve the mechanical properties and crack propagation resistance of natural rubber composites. This behavior is due to the synergistic effects

between different fillers. The result shows that CNT-3 has the strongest dynamic fatigue resistance. Carbon nanomaterials make the natural rubber more susceptible to SIC, which will promote the ability to deflect microcracks. CNT-9 shows the weakest dynamic fatigue performance because its hysteresis loss is much higher than that of the other composites. Therefore, finding the best amount of filler is essential for obtaining high-performance natural rubber composites.

5) This research also studies the effects of different shapes of carbon nanomaterials. We tested the crack propagation resistance and synergistic effects of the as-prepared composites. The results show that the G-C-3 composite has the best fatigue resistance performance, followed by G-C-1, CNT-3 and graphene-3. We also found that energy input is not the most important factor in crack growth. Our research shows that the G-C-3 composite has highest strain amplification effect and amplification area, which will help dissipate the local input tearing energy.

Chapter 8. References

[1] N. Saba, M. Jawaid, O. Y. Alothman, and M. T. Paridah, "A review on dynamic mechanical properties of natural fibre reinforced polymer composites," *Construction and Building Materials,* vol. 106, pp. 149-159, 2016.

[2] G. Sebald, Z. Xie, and D. Guyomar, "Fatigue effect of elastocaloric properties in natural rubber," *Philpsophical Transactions of the Royal Society A,* vol. 374, p. 20150302, 2016.

[3] K. S. Novoselov, V. I. Falko, L. Colombo, P. R. Gellert, M. G. Schwab, and K. Kim, "A roadmap for graphene," *Nature,* vol. 490, pp. 192-200, 2012.

[4] R. J. Young, I. A. Kinloch, L. Gong, and K. S. Novoselov, "The mechanics of graphene nanocomposites: A review," *Composites Science and Technology,* vol. 72, pp. 1459-1476, 2012.

[5] N. Suzuki, M. Ito, and F. Yatsuyanagi, "Effects of rubber/filler interactions on deformation behavior of silica filled SBR systems," *Polymer,* vol. 46, pp. 193-201, 2005.

[6] J. Leblanc, "Rubber–filler interactions and rheological properties in filled compounds," *Progress in Polymer Science,* vol. 27, pp. 627-687, 2002.

[7] R. Yang, Y. Song, and Q. Zheng, "Payne effect of silica-filled styrene-butadiene rubber," *Polymer,* vol. 116, pp. 304-313, 2017.

[8] K. Hu, D. D. Kulkarni, I. Choi, and V. V. Tsukruk, "Graphene-polymer nanocomposites for structural and functional applications," *Progress in Polymer Science,* vol. 39, pp. 1934-1972, 2014.

[9] A. Martone, C. Formicola, M. Giordano, and M. Zarrelli, "Reinforcement efficiency of multi-walled carbon nanotube/epoxy nano composites," *Composites Science and Technology,* vol. 70, pp. 1154-1160, 2010.

[10] S. Toki, B. S. Hsiao, S. Amnuaypornsri, and J. Sakdapipanich, "New insights into the relationship between network structure and strain-induced crystallization in un-vulcanized and vulcanized natural rubber by synchrotron X-ray diffraction," *Polymer,* vol. 50, pp. 2142-2148, 2009.

[11] A. Fakhru'l-Razi, M. A. Atieh, N. Girun, T. G. Chuah, M. El-Sadig, and D. R. A. Biak, "Effect of multi-wall carbon nanotubes on the mechanical properties of natural rubber," *Composite Structures,* vol. 75, pp. 496-500, 2006.

[12] S. Bhattacharyya, C. Sinturel, O. Bahloul, M.-L. Saboungi, S. Thomas, and J.-P. Salvetat, "Improving reinforcement of natural rubber by networking of activated carbon nanotubes," *Carbon,* vol. 46, pp. 1037-1045, 2008.

[13] M. Ameri, M. Reza Seif, M. Abbasi, and A. Khavandi Khiavi, "Viscoelastic fatigue resistance of asphalt binders modified with crumb rubber and styrene butadiene polymer," *Petroleum Science and Technology,* vol. 35, pp. 30-36, 2016.

[14] G. Ayoub, M. Naït-Abdelaziz, and F. Zaïri, "Multiaxial fatigue life predictors for rubbers: application of recent developments to a carbon-filled SBR," *International Journal of Fatigue,* vol. 66, pp. 168-176, 2014.

[15] A. K. Geim and K. S. Novoselov, "The rise of graphene," *Nature Materials,* vol. 6, pp. 183-191, 2007.

[16] E. T. Thostenson, Z. Ren, and T.-W. Chou, "Advances in the science and technology of carbon nanotubes and their composites: a review," *Composites Science and Technology,* vol. 61, pp. 1899-1912, 2001.

[17] H. Kim, A. A. Abdala, and C. W. Macosko, "Graphene/polymer nanocomposites," *Macromolecules,* vol. 43, pp. 6515-6530, 2010.

[18] C. S. Boland, U. Khan, G. Ryan, S. Barwich, R. Charifou, A. Harvey, *et al.*, "Sensitive electromechanical sensors using viscoelastic graphene-polymer nanocomposites," *Science,* vol. 354, p. 1257, 2016.

[19] M. Flamm, J. Spreckels, T. Steinweger, and U. Weltin, "Effects of very high loads on fatigue life of NR elastomer materials," *International Journal of Fatigue,* vol. 33, pp. 1189-1198, 2011.

[20] S. Chatterjee, F. A. Nüesch, and B. T. T. Chu, "Comparing carbon nanotubes and graphene nanoplatelets as reinforcements in polyamide 12 composites," *Nanotechnology,* vol. 22, p. 275714, 2011.

[21] K. S. Novoselov, A. K. Geim, S. V. Morozov, D. Jiang, Y. Zhang, S. V. Dubonos, *et al.*, "Electric field effect in atomically thin carbon films," *Science,* vol. 306, pp. 666-669, 2004.

[22] Y. Zhu, S. Murali, M. D. Stoller, K. J. Ganesh, W. Cai, P. J. Ferreira, *et al.*, "Carbon-based supercapacitors produced by activation of graphene," *Science,* vol. 332, pp. 1537-1541, 2011.

[23] T. Spratte, J. Plagge, M. Wunde, and M. Klüppel, "Investigation of strain-induced crystallization of carbon black and silica filled natural rubber composites based on mechanical and temperature measurements," *Polymer,* vol. 115, pp. 12-20, 2017.

[24] I. M. Ulfah, R. Fidyaningsih, S. Rahayu, D. A. Fitriani, D. A. Saputra, D. A. Winarto, *et al.*, "Influence of carbon black and silica filler on the rheological and mechanical properties of natural Rrubber compound," *Procedia Chemistry,* vol. 16, pp. 258-264, 2015.

[25] G. Mittal, V. Dhand, K. Y. Rhee, S.-J. Park, and W. R. Lee, "A review on carbon nanotubes and graphene as fillers in reinforced polymer nanocomposites," *Journal of Industrial and Engineering Chemistry,* vol. 21, pp. 11-25, 2015.

[26] T. Kuilla, S. Bhadra, D. Yao, N. H. Kim, S. Bose, and J. H. Lee, "Recent advances in graphene based polymer composites," *Progress in Polymer Science,* vol. 35, pp. 1350-1375, 2010.

[27] V. Singh, D. Joung, L. Zhai, S. Das, S. I. Khondaker, and S. Seal, "Graphene based materials: past, present and future," *Progress in Materials Science,* vol. 56, pp. 1178-1271, 2011.

[28] B. M. Yoo, H. J. Shin, H. W. Yoon, and H. B. Park, "Graphene and graphene oxide and their uses in barrier polymers," *Journal of Applied Polymer Science,* vol. 131, pp. n/a-n/a, 2014.

[29] D. G. Papageorgiou, I. A. Kinloch, and R. J. Young, "Graphene/elastomer nanocomposites," *Carbon,* vol. 95, pp. 460-484, 2015.

[30] P. Kueseng, P. Sae-oui, and N. Rattanasom, "Mechanical and electrical properties of natural rubber and nitrile rubber blends filled with multi-wall carbon nanotube: effect of preparation methods," *Polymer Testing,* vol. 32, pp. 731-738, 2013.

[31] K. M. Liew, Z. X. Lei, and L. W. Zhang, "Mechanical analysis of functionally graded carbon nanotube reinforced composites: A review," *Composite Structures,* vol. 120, pp. 90-97, 2015.

[32] M. Nadler, J. Werner, T. Mahrholz, U. Riedel, and W. Hufenbach, "Effect of CNT surface functionalisation on the mechanical properties of multi-walled carbon nanotube/epoxy-composites," *Composites Part A: Applied Science and Manufacturing,* vol. 40, pp. 932-937, 2009.

[33] D. Li, M. B. Muller, S. Gilje, R. B. Kaner, and G. G. Wallace, "Processable aqueous dispersions of graphene nanosheets," *Nat Nanotechnol,* vol. 3, pp. 101-

5, 2008.
[34] M. Lotya, P. J. King, U. Khan, S. De, and J. N. Coleman, "High-concentration, surfactant-stabilized graphene dispersions," *ACS Nano,* vol. 4, pp. 3155-3162, 2010.
[35] S. Stankovich, R. D. Piner, X. Chen, N. Wu, S. T. Nguyen, and R. S. Ruoff, "Stable aqueous dispersions of graphitic nanoplatelets via the reduction of exfoliated graphite oxide in the presence of poly(sodium 4-styrenesulfonate)," *J. Mater. Chem.,* vol. 16, pp. 155-158, 2006.
[36] A. K. Geim, "Graphene: status and prospects," *Science,* vol. 324, pp. 1530-1534, 2009.
[37] S. Stankovich, D. A. Dikin, G. H. B. Dommett, K. M. Kohlhaas, E. J. Zimney, E. A. Stach, *et al.*, "Graphene-based composite materials," *Nature,* vol. 442, pp. 282-286, 2006.
[38] Q. Su, S. Pang, V. Alijani, C. Li, X. Feng, and K. Müllen, "Composites of graphene with large aromatic molecules," *Advanced Materials,* vol. 21, pp. 3191-3195, 2009.
[39] R. Verdejo, M. M. Bernal, L. J. Romasanta, and M. A. Lopez-Manchado, "Graphene filled polymer nanocomposites," *J. Mater. Chem.,* vol. 21, pp. 3301-3310, 2011.
[40] M. Martin-Gallego, R. Verdejo, M. A. Lopez-Manchado, and M. Sangermano, "Epoxy-graphene UV-cured nanocomposites," *Polymer,* vol. 52, pp. 4664-4669, 2011.
[41] A. H. Castro Neto, F. Guinea, N. M. R. Peres, K. S. Novoselov, and A. K. Geim, "The electronic properties of graphene," *Reviews of Modern Physics,* vol. 81, pp. 109-162, 2009.
[42] M. Hernández, M. d. M. Bernal, R. Verdejo, T. A. Ezquerra, and M. A. López-Manchado, "Overall performance of natural rubber/graphene nanocomposites," *Composites Science and Technology,* vol. 73, pp. 40-46, 2012.
[43] Y. Song, J. Yu, L. Yu, F. E. Alam, W. Dai, C. Li, *et al.*, "Enhancing the thermal, electrical, and mechanical properties of silicone rubber by addition of graphene nanoplatelets," *Materials & Design,* vol. 88, pp. 950-957, 2015.
[44] S. N. Tripathi, P. Saini, D. Gupta, and V. Choudhary, "Electrical and mechanical properties of PMMA/reduced graphene oxide nanocomposites prepared via in situ polymerization," *Journal of Materials Science,* vol. 48, pp. 6223-6232, 2013.
[45] L. Gong, R. J. Young, I. A. Kinloch, I. Riaz, R. Jalil, and K. S. Novoselov, "Optimizing the reinforcement of polymer-based nanocomposites by graphene," *ACS Nano,* vol. 6, pp. 2086-2095, 2012.
[46] U. Khan, P. May, A. O'Neill, and J. N. Coleman, "Development of stiff, strong, yet tough composites by the addition of solvent exfoliated graphene to polyurethane," *Carbon,* vol. 48, pp. 4035-4041, 2010.
[47] B. Z. Jang and A. Zhamu, "Processing of nanographene platelets (NGPs) and NGP nanocomposites: a review," *Journal of Materials Science,* vol. 43, pp. 5092-5101, 2008.
[48] RamanathanT, A. A. Abdala, StankovichS, D. A. Dikin, M. Herrera Alonso, R. D. Piner, *et al.*, "Functionalized graphene sheets for polymer nanocomposites," *Nat Nano,* vol. 3, pp. 327-331, 2008.
[49] H. Kim and C. W. Macosko, "Processing-property relationships of polycarbonate/graphene composites," *Polymer,* vol. 50, pp. 3797-3809, 2009.
[50] A. Das, G. R. Kasaliwal, R. Jurk, R. Boldt, D. Fischer, K. W. Stöckelhuber, *et*

al., "Rubber composites based on graphene nanoplatelets, expanded graphite, carbon nanotubes and their combination: A comparative study," *Composites Science and Technology,* vol. 72, pp. 1961-1967, 2012.

[51] H. Kim, S. Kobayashi, M. A. AbdurRahim, M. J. Zhang, A. Khusainova, M. A. Hillmyer, *et al.*, "Graphene/polyethylene nanocomposites: effect of polyethylene functionalization and blending methods," *Polymer,* vol. 52, pp. 1837-1846, 2011.

[52] J. R. Potts, D. R. Dreyer, C. W. Bielawski, and R. S. Ruoff, "Graphene-based polymer nanocomposites," *Polymer,* vol. 52, pp. 5-25, 2011.

[53] S. Stankovich, D. A. Dikin, G. H. Dommett, K. M. Kohlhaas, E. J. Zimney, E. A. Stach, *et al.*, "Graphene-based composite materials," *Nature,* vol. 442, pp. 282-6, 2006.

[54] A. A. Balandin, S. Ghosh, W. Bao, I. Calizo, D. Teweldebrhan, F. Miao, *et al.*, "Superior thermal conductivity of single-layer graphene," *Nano Letters,* vol. 8, pp. 902-907, 2008.

[55] T. Kuila, S. Bose, P. Khanra, N. H. Kim, K. Y. Rhee, and J. H. Lee, "Characterization and properties of in situ emulsion polymerized poly(methyl methacrylate)/graphene nanocomposites," *Composites Part A: Applied Science and Manufacturing,* vol. 42, pp. 1856-1861, 2011.

[56] G. Gonçalves, P. A. A. P. Marques, A. Barros-Timmons, I. Bdkin, M. K. Singh, N. Emami, *et al.*, "Graphene oxide modified with PMMA via ATRP as a reinforcement filler," *Journal of Materials Chemistry,* vol. 20, p. 9927, 2010.

[57] V. Biju, "Chemical modifications and bioconjugate reactions of nanomaterials for sensing, imaging, drug delivery and therapy," *Chem Soc Rev,* vol. 43, pp. 744-64, 2014.

[58] T. Ramanathan, A. A. Abdala, S. Stankovich, D. A. Dikin, M. Herrera-Alonso, R. D. Piner, *et al.*, "Functionalized graphene sheets for polymer nanocomposites," *Nat Nanotechnol,* vol. 3, pp. 327-31, 2008.

[59] S. B. Bon, L. Valentini, R. Verdejo, J. L. Garcia Fierro, L. Peponi, M. A. Lopez-Manchado, *et al.*, "Plasma fluorination of chemically derived graphene sheets and subsequent modification with butylamine," *Chemistry of Materials,* vol. 21, pp. 3433-3438, 2009.

[60] S. Iijima, "Helical microtubules of graphitic carbon," *Nature,* vol. 354, p. 56, 1991.

[61] S. Iijima and T. Ichihashi, "Single-shell carbon nanotubes of 1-nm diameter," *Nature,* vol. 363, pp. 603-605, 1993.

[62] A. M. Shanmugharaj, J. H. Bae, K. Y. Lee, W. H. Noh, S. H. Lee, and S. H. Ryu, "Physical and chemical characteristics of multiwalled carbon nanotubes functionalized with aminosilane and its influence on the properties of natural rubber composites," *Composites Science and Technology,* vol. 67, pp. 1813-1822, 2007.

[63] X.-L. Xie, Y.-W. Mai, and X.-P. Zhou, "Dispersion and alignment of carbon nanotubes in polymer matrix: A review," *Materials Science and Engineering: R: Reports,* vol. 49, pp. 89-112, 2005.

[64] L. Bokobza, "Multiwall carbon nanotube elastomeric composites: A review," *Polymer,* vol. 48, pp. 4907-4920, 2007.

[65] V. D. Punetha, S. Rana, H. J. Yoo, A. Chaurasia, J. T. McLeskey, M. S. Ramasamy, *et al.*, "Functionalization of carbon nanomaterials for advanced polymer nanocomposites: a comparison study between CNT and graphene," *Progress in Polymer Science,* vol. 67, pp. 1-47, 2017.

[66] B. Arash, H. S. Park, and T. Rabczuk, "Mechanical properties of carbon nanotube reinforced polymer nanocomposites: a coarse-grained model," *Composites Part B: Engineering,* vol. 80, pp. 92-100, 2015.

[67] W.-W. Liu, S.-P. Chai, A. R. Mohamed, and U. Hashim, "Synthesis and characterization of graphene and carbon nanotubes: a review on the past and recent developments," *Journal of Industrial and Engineering Chemistry,* vol. 20, pp. 1171-1185, 2014.

[68] A. Godara, L. Mezzo, F. Luizi, A. Warrier, S. V. Lomov, A. W. van Vuure, *et al.*, "Influence of carbon nanotube reinforcement on the processing and the mechanical behaviour of carbon fiber/epoxy composites," *Carbon,* vol. 47, pp. 2914-2923, 2009.

[69] X. Wu, C. Lu, Y. Han, Z. Zhou, G. Yuan, and X. Zhang, "Cellulose nanowhisker modulated 3D hierarchical conductive structure of carbon black/natural rubber nanocomposites for liquid and strain sensing application," *Composites Science and Technology,* vol. 124, pp. 44-51, 2016.

[70] M. Kaempgen, C. K. Chan, J. Ma, Y. Cui, and G. Gruner, "Printable thin film supercapacitors using single-walled carbon nanotubes," *Nano Lett,* vol. 9, pp. 1872-6, 2009.

[71] R. H. Baughman, A. A. Zakhidov, and W. A. de Heer, "Carbon nanotubes--the route toward applications," *Science,* vol. 297, pp. 787-92, 2002.

[72] M. Terrones, "Science and technology of the twenty-first century: synthesis, properties, and applications of carbon nanotubes," *Annual Review of Materials Research,* vol. 33, pp. 419-501, 2003.

[73] R. Krupke, F. Hennrich, H. Lohneysen, and M. M. Kappes, "Separation of metallic from semiconducting single-walled carbon nanotubes," *Science,* vol. 301, pp. 344-7, 2003.

[74] H. Kataura, Y. Kumazawa, Y. Maniwa, I. Umezu, S. Suzuki, Y. Ohtsuka, *et al.*, "Optical properties of single-wall carbon nanotubes," *Synthetic Metals,* vol. 103, pp. 2555-2558, 1999.

[75] V. Sazonova, Y. Yaish, H. Ustunel, D. Roundy, T. A. Arias, and P. L. McEuen, "A tunable carbon nanotube electromechanical oscillator," *Nature,* vol. 431, pp. 284-7, 2004.

[76] P. L. McEuen, M. S. Fuhrer, and P. Hongkun, "Single-walled carbon nanotube electronics," *IEEE Transactions On Nanotechnology,* vol. 1, pp. 78-85, 2002.

[77] A. Eatemadi, H. Daraee, H. Karimkhanloo, M. Kouhi, N. Zarghami, A. Akbarzadeh, *et al.*, "Carbon nanotubes: properties, synthesis, purification, and medical applications," *Nanoscale Res Lett,* vol. 9, p. 393, 2014.

[78] L. Guadagno, B. De Vivo, A. Di Bartolomeo, P. Lamberti, A. Sorrentino, V. Tucci, *et al.*, "Effect of functionalization on the thermo-mechanical and electrical behavior of multi-wall carbon nanotube/epoxy composites," *Carbon,* vol. 49, pp. 1919-1930, 2011.

[79] Z. Spitalsky, D. Tasis, K. Papagelis, and C. Galiotis, "Carbon nanotube–polymer composites: chemistry, processing, mechanical and electrical properties," *Progress in Polymer Science,* vol. 35, pp. 357-401, 2010.

[80] F. H. Gojny, M. H. G. Wichmann, U. Köpke, B. Fiedler, and K. Schulte, "Carbon nanotube-reinforced epoxy-composites: enhanced stiffness and fracture toughness at low nanotube content," *Composites Science and Technology,* vol. 64, pp. 2363-2371, 2004.

[81] J. Phiri, P. Gane, and T. C. Maloney, "General overview of graphene: production, properties and application in polymer composites," *Materials Science and*

Engineering: B, vol. 215, pp. 9-28, 2017.

[82] J. Wu, W. Xing, G. Huang, H. Li, M. Tang, S. Wu, *et al.*, "Vulcanization kinetics of graphene/natural rubber nanocomposites," *Polymer,* vol. 54, pp. 3314-3323, 2013.

[83] Y. Mao, S. Wen, Y. Chen, F. Zhang, P. Panine, T. W. Chan, *et al.*, "High performance graphene oxide based rubber composites," *Sci Rep,* vol. 3, p. 2508, 2013.

[84] S. Yaragalla, M. A.P, N. Kalarikkal, and S. Thomas, "Chemistry associated with natural rubber–graphene nanocomposites and its effect on physical and structural properties," *Industrial Crops and Products,* vol. 74, pp. 792-802, 2015.

[85] C. S. Boland, U. Khan, C. Backes, A. O'Neill, J. McCauley, S. Duane, *et al.*, "Sensitive, high-strain, high-rate bodily motion sensors based on graphene-rubber composites," *ACS Nano,* vol. 8, pp. 8819-30, 2014.

[86] X. Xue, Q. Yin, H. Jia, X. Zhang, Y. Wen, Q. Ji, *et al.*, "Enhancing mechanical and thermal properties of styrene-butadiene rubber/carboxylated acrylonitrile butadiene rubber blend by the usage of graphene oxide with diverse oxidation degrees," *Applied Surface Science,* vol. 423, pp. 584-591, 2017.

[87] C. Leopold, W. V. Liebig, H. Wittich, and B. Fiedler, "Size effect of graphene nanoparticle modified epoxy matrix," *Composites Science and Technology,* vol. 134, pp. 217-225, 2016.

[88] K. K. Sadasivuni, D. Ponnamma, S. Thomas, and Y. Grohens, "Evolution from graphite to graphene elastomer composites," *Progress in Polymer Science,* vol. 39, pp. 749-780, 2014.

[89] B. Mensah, S. Kim, S. Arepalli, and C. Nah, "A study of graphene oxide-reinforced rubber nanocomposite," *Journal of Applied Polymer Science,* vol. 131, pp. n/a-n/a, 2014.

[90] A. A. Azira, M. M. Kamal, and M. Rusop, "Reinforcement of graphene in natural rubber nanocomposite," 2016.

[91] A. Shaygan Nia and W. H. Binder, "Graphene as initiator/catalyst in polymerization chemistry," *Progress in Polymer Science,* vol. 67, pp. 48-76, 2017.

[92] S. Chandrasekaran, N. Sato, F. Tölle, R. Mülhaupt, B. Fiedler, and K. Schulte, "Fracture toughness and failure mechanism of graphene based epoxy composites," *Composites Science and Technology,* vol. 97, pp. 90-99, 2014.

[93] L.-C. Tang, Y.-J. Wan, D. Yan, Y.-B. Pei, L. Zhao, Y.-B. Li, *et al.*, "The effect of graphene dispersion on the mechanical properties of graphene/epoxy composites," *Carbon,* vol. 60, pp. 16-27, 2013.

[94] R. Surudžić, A. Janković, M. Mitrić, I. Matić, Z. D. Juranić, L. Živković, *et al.*, "The effect of graphene loading on mechanical, thermal and biological properties of poly(vinyl alcohol)/graphene nanocomposites," *Journal of Industrial and Engineering Chemistry,* vol. 34, pp. 250-257, 2016.

[95] H. Yang, F. Li, C. Shan, D. Han, Q. Zhang, L. Niu, *et al.*, "Covalent functionalization of chemically converted graphene sheets via silane and its reinforcement," *Journal of Materials Chemistry,* vol. 19, p. 4632, 2009.

[96] J. Tsai and C. T. Sun, "Effect of platelet dispersion on the load transfer efficiency in nanoclay composites," *Journal of Composite Materials,* vol. 38, pp. 567-579, 2004.

[97] C. Su Woo and H. S. Park, "Fatigue life evaluation of rubber-clay nanocomposites," *Procedia Structural Integrity,* vol. 2, pp. 2173-2181, 2016.

[98] D. W. Johnson, B. P. Dobson, and K. S. Coleman, "A manufacturing perspective on graphene dispersions," *Current Opinion in Colloid & Interface Science,* vol. 20, pp. 367-382, 2015.

[99] X. Ji, Y. Xu, W. Zhang, L. Cui, and J. Liu, "Review of functionalization, structure and properties of graphene/polymer composite fibers," *Composites Part A: Applied Science and Manufacturing,* vol. 87, pp. 29-45, 2016.

[100] A. O'Neill, U. Khan, P. N. Nirmalraj, J. Boland, and J. N. Coleman, "Graphene dispersion and exfoliation in low boiling point solvents," *The Journal of Physical Chemistry C,* vol. 115, pp. 5422-5428, 2011.

[101] N. Hayeemasae, W. G. I. U. Rathnayake, and H. Ismail, "Nano-sized TiO2-reinforced natural rubber composites prepared by latex compounding method," *Journal of Vinyl and Additive Technology,* vol. 23, pp. 200-209, 2017.

[102] P. Berki, K. László, N. T. Tung, and J. Karger-Kocsis, "Natural rubber/graphene oxide nanocomposites via melt and latex compounding: comparison at very low graphene oxide content," *Journal of Reinforced Plastics and Composites,* vol. 36, pp. 808-817, 2017.

[103] W. Xing, M. Tang, J. Wu, G. Huang, H. Li, Z. Lei, *et al.*, "Multifunctional properties of graphene/rubber nanocomposites fabricated by a modified latex compounding method," *Composites Science and Technology,* vol. 99, pp. 67-74, 2014.

[104] Y. Zhan, J. Wu, H. Xia, N. Yan, G. Fei, and G. Yuan, "Dispersion and exfoliation of graphene in rubber by an ultrasonically-assisted latex mixing and in situ reduction process," *Macromolecular Materials and Engineering,* vol. 296, pp. 590-602, 2011.

[105] Y. Zhan, M. Lavorgna, G. Buonocore, and H. Xia, "Enhancing electrical conductivity of rubber composites by constructing interconnected network of self-assembled graphene with latex mixing," *Journal of Materials Chemistry,* vol. 22, p. 10464, 2012.

[106] E. Tkalya, M. Ghislandi, A. Alekseev, C. Koning, and J. Loos, "Latex-based concept for the preparation of graphene-based polymer nanocomposites," *Journal of Materials Chemistry,* vol. 20, p. 3035, 2010.

[107] G. Scherillo, M. Lavorgna, G. G. Buonocore, Y. H. Zhan, H. S. Xia, G. Mensitieri, *et al.*, "Tailoring assembly of reduced graphene oxide nanosheets to control gas barrier properties of natural rubber nanocomposites," *ACS Appl Mater Interfaces,* vol. 6, pp. 2230-4, 2014.

[108] Y. Lin, Y. Chen, Z. Zeng, J. Zhu, Y. Wei, F. Li, *et al.*, "Effect of ZnO nanoparticles doped graphene on static and dynamic mechanical properties of natural rubber composites," *Composites Part A: Applied Science and Manufacturing,* vol. 70, pp. 35-44, 2015.

[109] Y. Lin, Y. Z. Chen, Y. Zhang, D. M. Jia, Y. F. Luo, and L. Liu, "The use of zinc dimethacrylate functionalized graphene as a reinforcement in rubber composites," *Polymers for Advanced Technologies,* vol. 26, pp. 423-431, 2015.

[110] P. M. Ajayan, O. Stephan, C. Colliex, and D. Trauth, "Aligned carbon nanotube arrays formed by cutting a polymer resin--nanotube composite," *Science,* vol. 265, pp. 1212-4, 1994.

[111] P.-C. Ma, N. A. Siddiqui, G. Marom, and J.-K. Kim, "Dispersion and functionalization of carbon nanotubes for polymer-based nanocomposites: A review," *Composites Part A: Applied Science and Manufacturing,* vol. 41, pp. 1345-1367, 2010.

[112] D. Qian, E. C. Dickey, R. Andrews, and T. Rantell, "Load transfer and

deformation mechanisms in carbon nanotube-polystyrene composites," *Applied Physics Letters,* vol. 76, pp. 2868-2870, 2000.
[113] P. J. F. Harris, "Carbon nanotube composites," *International Materials Reviews,* vol. 49, pp. 31-43, 2013.
[114] F. H. Gojny, J. Nastalczyk, Z. Roslaniec, and K. Schulte, "Surface modified multi-walled carbon nanotubes in CNT/epoxy-composites," *Chemical Physics Letters,* vol. 370, pp. 820-824, 2003.
[115] Y. Geng, M. Y. Liu, J. Li, X. M. Shi, and J. K. Kim, "Effects of surfactant treatment on mechanical and electrical properties of CNT/epoxy nanocomposites," *Composites Part A: Applied Science and Manufacturing,* vol. 39, pp. 1876-1883, 2008.
[116] T. Jose, G. Moni, S. S, A. J. Raju, J. J. George, and S. C. George, "Multifunctional multi-walled carbon nanotube reinforced natural rubber nanocomposites," *Industrial Crops and Products,* vol. 105, pp. 63-73, 2017.
[117] L. Bokobza, "Enhanced electrical and mechanical properties of multiwall carbon nanotube rubber composites," *Polymers for Advanced Technologies,* vol. 23, pp. 1543-1549, 2012.
[118] A. Behroozikhah, S. H. Morafa, and S. Aflaki, "Investigation of fatigue cracks on RAP mixtures containing sasobit and crumb rubber based on fracture energy," *Construction and Building Materials,* vol. 141, pp. 526-532, 2017.
[119] Y. Nakaramontri, C. Kummerlöwe, C. Nakason, and N. Vennemann, "The effect of surface functionalization of carbon nanotubes on properties of natural rubber/carbon nanotube composites," *Polymer Composites,* vol. 36, pp. 2113-2122, 2015.
[120] S. Ata, K. Kobashi, M. Yumura, and K. Hata, "Mechanically durable and highly conductive elastomeric composites from long single-walled carbon nanotubes mimicking the chain structure of polymers," *Nano Letters,* vol. 12, pp. 2710-2716, 2012.
[121] F. Gardea and D. C. Lagoudas, "Characterization of electrical and thermal properties of carbon nanotube/epoxy composites," *Composites Part B: Engineering,* vol. 56, pp. 611-620, 2014.
[122] C. Ma, H.-Y. Liu, X. Du, L. Mach, F. Xu, and Y.-W. Mai, "Fracture resistance, thermal and electrical properties of epoxy composites containing aligned carbon nanotubes by low magnetic field," *Composites Science and Technology,* vol. 114, pp. 126-135, 2015.
[123] M. J. Biercuk, M. C. Llaguno, M. Radosavljevic, J. K. Hyun, A. T. Johnson, and J. E. Fischer, "Carbon nanotube composites for thermal management," *Applied Physics Letters,* vol. 80, pp. 2767-2769, 2002.
[124] S. Shenogin, L. Xue, R. Ozisik, P. Keblinski, and D. G. Cahill, "Role of thermal boundary resistance on the heat flow in carbon-nanotube composites," *Journal of Applied Physics,* vol. 95, pp. 8136-8144, 2004.
[125] W.-J. Chou, C.-C. Wang, and C.-Y. Chen, "Thermal behaviors of polyimide with plasma-modified carbon nanotubes," *Polymer Degradation and Stability,* vol. 93, pp. 745-752, 2008.
[126] S. Shenogin, A. Bodapati, L. Xue, R. Ozisik, and P. Keblinski, "Effect of chemical functionalization on thermal transport of carbon nanotube composites," *Applied Physics Letters,* vol. 85, pp. 2229-2231, 2004.
[127] C.-W. Nan, G. Liu, Y. Lin, and M. Li, "Interface effect on thermal conductivity of carbon nanotube composites," *Applied Physics Letters,* vol. 85, pp. 3549-3551, 2004.

[128] Y.-j. Xiao, W.-y. Wang, X.-j. Chen, T. Lin, Y.-t. Zhang, J.-h. Yang, *et al.*, "Hybrid network structure and thermal conductive properties in poly(vinylidene fluoride) composites based on carbon nanotubes and graphene nanoplatelets," *Composites Part A: Applied Science and Manufacturing,* vol. 90, pp. 614-625, 2016.

[129] I. Kholmanov, J. Kim, E. Ou, R. S. Ruoff, and L. Shi, "Continuous carbon nanotube-ultrathin graphite hybrid foams for increased thermal conductivity and suppressed subcooling in composite phase change materials," *ACS Nano,* vol. 9, pp. 11699-707, 2015.

[130] W.-b. Zhang, Z.-x. Zhang, J.-h. Yang, T. Huang, N. Zhang, X.-t. Zheng, *et al.*, "Largely enhanced thermal conductivity of poly(vinylidene fluoride)/carbon nanotube composites achieved by adding graphene oxide," *Carbon,* vol. 90, pp. 242-254, 2015.

[131] C. W. Nan, Z. Shi, and Y. Lin, "A simple model for thermal conductivity of carbon nanotube-based composites," *Chemical Physics Letters,* vol. 375, pp. 666-669, 2003.

[132] Z. Han and A. Fina, "Thermal conductivity of carbon nanotubes and their polymer nanocomposites: A review," *Progress in Polymer Science,* vol. 36, pp. 914-944, 2011.

[133] K. Chu, Q. Wu, C. Jia, X. Liang, J. Nie, W. Tian, *et al.*, "Fabrication and effective thermal conductivity of multi-walled carbon nanotubes reinforced Cu matrix composites for heat sink applications," *Composites Science and Technology,* vol. 70, pp. 298-304, 2010.

[134] Y. Lin, S. Liu, J. Peng, and L. Liu, "The filler–rubber interface and reinforcement in styrene butadiene rubber composites with graphene/silica hybrids: A quantitative correlation with the constrained region," *Composites Part A: Applied Science and Manufacturing,* vol. 86, pp. 19-30, 2016.

[135] D. Shia, C. Y. Hui, S. D. Burnside, and E. P. Giannelis, "An interface model for the prediction of Young's modulus of layered silicate-elastomer nanocomposites," *Polymer Composites,* vol. 19, pp. 608-617, 1998.

[136] K. P. Pramoda, H. Hussain, H. M. Koh, H. R. Tan, and C. B. He, "Covalent bonded polymer–graphene nanocomposites," *Journal of Polymer Science Part A: Polymer Chemistry,* vol. 48, pp. 4262-4267, 2010.

[137] S. Park and R. S. Ruoff, "Chemical methods for the production of graphenes," *Nat Nano,* vol. 4, pp. 217-224, 2009.

[138] S. Ganguli, A. K. Roy, and D. P. Anderson, "Improved thermal conductivity for chemically functionalized exfoliated graphite/epoxy composites," *Carbon,* vol. 46, pp. 806-817, 2008.

[139] L. Valentini, I. Armentano, F. Mengoni, D. Puglia, G. Pennelli, and J. M. Kenny, "Chemical gating and photoconductivity of CF4 plasma-functionalized single-walled carbon nanotubes with adsorbed butylamine," *Journal of Applied Physics,* vol. 97, p. 114320, 2005.

[140] J. R. Potts, S. H. Lee, T. M. Alam, J. An, M. D. Stoller, R. D. Piner, *et al.*, "Thermomechanical properties of chemically modified graphene/poly(methyl methacrylate) composites made by in situ polymerization," *Carbon,* vol. 49, pp. 2615-2623, 2011.

[141] Y. Lin, J. Jin, and M. Song, "Preparation and characterisation of covalent polymer functionalized graphene oxide," *J. Mater. Chem.,* vol. 21, pp. 3455-3461, 2011.

[142] R. Y. Hong, H. P. Fu, Y. J. Zhang, L. Liu, J. Wang, H. Z. Li, *et al.*, "Surface-

modified silica nanoparticles for reinforcement of PMMA," *Journal of Applied Polymer Science,* vol. 105, pp. 2176-2184, 2007.
[143] E.-Y. Choi, T. H. Han, J. Hong, J. E. Kim, S. H. Lee, H. W. Kim, *et al.*, "Noncovalent functionalization of graphene with end-functional polymers," *Journal of Materials Chemistry,* vol. 20, p. 1907, 2010.
[144] V. Georgakilas, M. Otyepka, A. B. Bourlinos, V. Chandra, N. Kim, K. C. Kemp, *et al.*, "Functionalization of graphene: covalent and non-covalent approaches, derivatives and applications," *Chem Rev,* vol. 112, pp. 6156-214, 2012.
[145] R. J. Chen, S. Bangsaruntip, K. A. Drouvalakis, N. W. Kam, M. Shim, Y. Li, *et al.*, "Noncovalent functionalization of carbon nanotubes for highly specific electronic biosensors," *Proc Natl Acad Sci U S A,* vol. 100, pp. 4984-9, 2003.
[146] K. Preetha Nair, P. Thomas, and R. Joseph, "Latex stage blending of multiwalled carbon nanotube in carboxylated acrylonitrile butadiene rubber: Mechanical and electrical properties," *Materials & Design,* vol. 41, pp. 23-30, 2012.
[147] R. J. Chen, S. Bangsaruntip, K. A. Drouvalakis, K. Nadine Wong Shi, M. Shim, Y. Li, *et al.*, "Noncovalent functionalization of carbon nanotubes for highly specific electronic biosensors," *Proceedings of the National Academy of Sciences of the United States of America,* vol. 100, pp. 4984-4989, 2003.
[148] K. Qu, Y. Zheng, S. Dai, and S. Z. Qiao, "Polydopamine-graphene oxide derived mesoporous carbon nanosheets for enhanced oxygen reduction," *Nanoscale,* vol. 7, pp. 12598-12605, 2015.
[149] Y.-P. Sun, K. Fu, Y. Lin, and W. Huang, "Functionalized carbon nanotubes: properties and applications," *Accounts of Chemical Research,* vol. 35, pp. 1096-1104, 2002.
[150] Y. L. Zhao and J. F. Stoddart, "Noncovalent functionalization of single-walled carbon nanotubes," *Acc Chem Res,* vol. 42, pp. 1161-71, 2009.
[151] R. J. Chen, Y. Zhang, D. Wang, and H. Dai, "Noncovalent sidewall functionalization of single-walled carbon nanotubes for protein immobilization," *Journal of the American Chemical Society,* vol. 123, pp. 3838-3839, 2001.
[152] E. E. Tkalya, M. Ghislandi, G. de With, and C. E. Koning, "The use of surfactants for dispersing carbon nanotubes and graphene to make conductive nanocomposites," *Current Opinion in Colloid & Interface Science,* vol. 17, pp. 225-232, 2012.
[153] Y.-J. Wan, W.-H. Yang, S.-H. Yu, R. Sun, C.-P. Wong, and W.-H. Liao, "Covalent polymer functionalization of graphene for improved dielectric properties and thermal stability of epoxy composites," *Composites Science and Technology,* vol. 122, pp. 27-35, 2016.
[154] X. Wang, W. Xing, P. Zhang, L. Song, H. Yang, and Y. Hu, "Covalent functionalization of graphene with organosilane and its use as a reinforcement in epoxy composites," *Composites Science and Technology,* vol. 72, pp. 737-743, 2012.
[155] J. Park and M. Yan, "Covalent functionalization of graphene with reactive intermediates," *Accounts of Chemical Research,* vol. 46, pp. 181-189, 2013.
[156] J. L. Bahr and J. M. Tour, "Covalent chemistry of single-wall carbon nanotubes," *Journal of Materials Chemistry,* vol. 12, pp. 1952-1958, 2002.
[157] C.-H. Tseng, C.-C. Wang, and C.-Y. Chen, "Functionalizing carbon nanotubes by plasma modification for the preparation of covalent-Integrated epoxy composites," *Chemistry of Materials,* vol. 19, pp. 308-315, 2007.
[158] C. A. Dyke and J. M. Tour, "Covalent functionalization of single-walled carbon

nanotubes for materials applications," *The Journal of Physical Chemistry A,* vol. 108, pp. 11151-11159, 2004.

[159] P. Potschke, N. P. Zschoerper, B. P. Moller, and U. Vohrer, "Plasma functionalization of multiwalled carbon nanotube bucky papers and the effect on properties of melt-mixed composites with polycarbonate," *Macromol Rapid Commun,* vol. 30, pp. 1828-33, 2009.

[160] U. Vohrer, N. P. Zschoerper, Y. Koehne, S. Langowski, and C. Oehr, "Plasma modification of carbon nanotubes and bucky papers," *Plasma Processes and Polymers,* vol. 4, pp. S871-S877, 2007.

[161] J. L. Bahr, J. Yang, D. V. Kosynkin, M. J. Bronikowski, R. E. Smalley, and J. M. Tour, "Functionalization of carbon nanotubes by electrochemical reduction of aryl diazonium salts: a bucky paper electrode," *Journal of the American Chemical Society,* vol. 123, pp. 6536-6542, 2001.

[162] M. Vesali-Naseh, Y. Mortazavi, A. A. Khodadadi, P. Parsaeian, and A. A. Moosavi-Movahedi, "Plasma thiol-functionalized carbon nanotubes decorated with gold nanoparticles for glucose biosensor," *Sensors and Actuators B: Chemical,* vol. 188, pp. 488-495, 2013.

[163] B. Ruelle, S. Peeterbroeck, R. Gouttebaron, T. Godfroid, F. Monteverde, J.-P. Dauchot, *et al.*, "Functionalization of carbon nanotubes by atomic nitrogen formed in a microwave plasma Ar + N2 and subsequent poly(ε-caprolactone) grafting," *J. Mater. Chem.*, vol. 17, pp. 157-159, 2007.

[164] M. A. Ray, O. Shenderova, W. Hook, A. Martin, V. Grishko, T. Tyler, *et al.*, "Cold plasma functionalization of nanodiamond particles," *Diamond and Related Materials,* vol. 15, pp. 1809-1812, 2006.

[165] M. V. Naseh, A. A. Khodadadi, Y. Mortazavi, F. Pourfayaz, O. Alizadeh, and M. Maghrebi, "Fast and clean functionalization of carbon nanotubes by dielectric barrier discharge plasma in air compared to acid treatment," *Carbon,* vol. 48, pp. 1369-1379, 2010.

[166] M. Garzia Trulli, E. Sardella, F. Palumbo, G. Palazzo, L. C. Giannossa, A. Mangone, *et al.*, "Towards highly stable aqueous dispersions of multi-walled carbon nanotubes: the effect of oxygen plasma functionalization," *J Colloid Interface Sci,* vol. 491, pp. 255-264, 2017.

[167] C. A. Covarrubias-Gordillo, F. Soriano-Corral, C. A. Ávila-Orta, V. J. Cruz-Delgado, M. G. Neira-Velázquez, E. Hernández-Hernández, *et al.*, "Surface modification of carbon nanofibers and graphene platelets mixtures by plasma polymerization of propylene," *Journal of Nanomaterials,* vol. 2017, pp. 1-10, 2017.

[168] K.-P. Yoo, K.-H. Kwon, N.-K. Min, M. J. Lee, and C. J. Lee, "Effects of O2 plasma treatment on NH3 sensing characteristics of multiwall carbon nanotube/polyaniline composite films," *Sensors and Actuators B: Chemical,* vol. 143, pp. 333-340, 2009.

[169] A. Dey, A. Chroneos, N. S. J. Braithwaite, R. P. Gandhiraman, and S. Krishnamurthy, "Plasma engineering of graphene," *Applied Physics Reviews,* vol. 3, 2016.

[170] L. Valentini, "Formation of unzipped carbon nanotubes by CF4 plasma treatment," *Diamond and Related Materials,* vol. 20, pp. 445-448, 2011.

[171] Y.-C. Lin, C.-Y. Lin, and P.-W. Chiu, "Controllable graphene N-doping with ammonia plasma," *Applied Physics Letters,* vol. 96, 2010.

[172] D. Kolacyak, J. Ihde, C. Merten, A. Hartwig, and U. Lommatzsch, "Fast functionalization of multi-walled carbon nanotubes by an atmospheric pressure

plasma jet," *J Colloid Interface Sci,* vol. 359, pp. 311-7, 2011.
[173] G. Kalita, S. Adhikari, H. R. Aryal, R. Afre, T. Soga, M. Sharon, *et al.*, "Functionalization of multi-walled carbon nanotubes (MWCNTs) with nitrogen plasma for photovoltaic device application," *Current Applied Physics,* vol. 9, pp. 346-351, 2009.
[174] Q. Wang, X. Wang, Z. Chai, and W. Hu, "Low-temperature plasma synthesis of carbon nanotubes and graphene based materials and their fuel cell applications," *Chem Soc Rev,* vol. 42, pp. 8821-34, 2013.
[175] L. G. Nair, A. S. Mahapatra, N. Gomathi, K. Joseph, S. Neogi, and C. P. R. Nair, "Radio frequency plasma mediated dry functionalization of multiwall carbon nanotube," *Applied Surface Science,* vol. 340, pp. 64-71, 2015.
[176] Y. J. Kim, H. Ma, and Q. Yu, "Plasma nanocoated carbon nanotubes for heat transfer nanofluids," *Nanotechnology,* vol. 21, p. 295703, 2010.
[177] M.-S. Park, K. H. Kim, and Y.-S. Lee, "Fluorination of single-walled carbon nanotube: The effects of fluorine on structural and electrical properties," *Journal of Industrial and Engineering Chemistry,* vol. 37, pp. 22-26, 2016.
[178] V. K. Abdelkader-Fernández, F. Morales-Lara, M. Melguizo, C. García-Gallarín, R. López-Garzón, M. L. Godino-Salido, *et al.*, "Degree of functionalization and stability of fluorine groups fixed to carbon nanotubes and graphite nanoplates by CF 4 microwave plasma," *Applied Surface Science,* vol. 357, pp. 1410-1418, 2015.
[179] O.-K. Park, W. Young Kim, S. Min Kim, N.-H. You, Y. Jeong, H. Su Lee, *et al.*, "Effect of oxygen plasma treatment on the mechanical properties of carbon nanotube fibers," *Materials Letters,* vol. 156, pp. 17-20, 2015.
[180] A. Felten, J. Ghijsen, J. J. Pireaux, R. L. Johnson, C. M. Whelan, D. Liang, *et al.*, "Photoemission study of CF4 rf-Plasma treated multi-wall carbon nanotubes," *Carbon,* vol. 46, pp. 1271-1275, 2008.
[181] J. Y. Yook, J. Jun, and S. Kwak, "Amino functionalization of carbon nanotube surfaces with NH3 plasma treatment," *Applied Surface Science,* vol. 256, pp. 6941-6944, 2010.
[182] D. Kolacyak, J. Ihde, and U. Lommatzsch, "Carbon nanotube functionalization by atmospheric pressure plasma and post-plasma reactions," *Surface and Coatings Technology,* vol. 205, pp. S605-S608, 2011.
[183] C. Chen, B. Liang, D. Lu, A. Ogino, X. Wang, and M. Nagatsu, "Amino group introduction onto multiwall carbon nanotubes by NH3/Ar plasma treatment," *Carbon,* vol. 48, pp. 939-948, 2010.
[184] R. Scaffaro, A. Maio, S. Agnello, and A. Glisenti, "Plasma functionalization of multiwalled carbon nanotubes and their use in the preparation of nylon 6-based nanohybrids," *Plasma Processes and Polymers,* vol. 9, pp. 503-512, 2012.
[185] A. O. Lobo, S. C. Ramos, E. F. Antunes, F. R. Marciano, V. J. Trava-Airoldi, and E. J. Corat, "Fast functionalization of vertically aligned multiwalled carbon nanotubes using oxygen plasma," *Materials Letters,* vol. 70, pp. 89-93, 2012.
[186] F. Pourfayaz, Y. Mortazavi, A.-a. Khodadadi, S. H. Jafari, S. Boroun, and M. V. Naseh, "A comparison of effects of plasma and acid functionalizations on structure and electrical property of multi-wall carbon nanotubes," *Applied Surface Science,* vol. 295, pp. 66-70, 2014.
[187] X. Liu, S. Zhao, X. Zhang, X. Li, and Y. Bai, "Preparation, structure, and properties of solution-polymerized styrene-butadiene rubber with functionalized end-groups and its silica-filled composites," *Polymer,* vol. 55, pp. 1964-1976, 2014.

[188] H. Kang, Y. Tang, L. Yao, F. Yang, Q. Fang, and D. Hui, "Fabrication of graphene/natural rubber nanocomposites with high dynamic properties through convenient mechanical mixing," *Composites Part B: Engineering,* vol. 112, pp. 1-7, 2017.

[189] S. N. Tripathi, R. S. Malik, and V. Choudhary, "Melt rheology and thermomechanical behavior of poly(methyl methacrylate)/reduced graphene oxide nanocomposites," *Polymers for Advanced Technologies,* vol. 26, pp. 1558-1566, 2015.

[190] S. Araby, Q. Meng, L. Zhang, I. Zaman, P. Majewski, and J. Ma, "Elastomeric composites based on carbon nanomaterials," *Nanotechnology,* vol. 26, p. 112001, 2015.

[191] T. Zarrin-Ghalami and A. Fatemi, "Multiaxial fatigue and life prediction of elastomeric components," *International Journal of Fatigue,* vol. 55, pp. 92-101, 2013.

[192] P. Behroozinia, R. Mirzaeifar, and S. Taheri, "A review of fatigue and fracture mechanics with a focus on rubber-based materials," *Proceedings of the Institution of Mechanical Engineers, Part L: Journal of Materials: Design and Applications,* 2017.

[193] Y. Marco, B. Huneau, I. Masquelier, V. Le Saux, and P. Charrier, "Prediction of fatigue properties of natural rubber based on the descriptions of the cracks population and of the dissipated energy," *Polymer Testing,* vol. 59, pp. 67-74, 2017.

[194] S. Seichter, V.-M. Archodoulaki, T. Koch, A. Holzner, and A. Wondracek, "Investigation of different influences on the fatigue behaviour of industrial rubbers," *Polymer Testing,* vol. 59, pp. 99-106, 2017.

[195] C. Cruanes, F. Lacroix, G. Berton, S. Méo, and N. Ranganathan, "Study of the fatigue behavior of a synthetic rubber undergoing cumulative damage tests," *International Journal of Fatigue,* vol. 91, pp. 322-327, 2016.

[196] J. R. Cho, Y. H. Yoon, C. W. Seo, and Y. G. Kim, "Fatigue life assessment of fabric braided composite rubber hose in complicated large deformation cyclic motion," *Finite Elements in Analysis and Design,* vol. 100, pp. 65-76, 2015.

[197] A. Zine, N. Benseddiq, and M. Naït Abdelaziz, "Rubber fatigue life under multiaxial loading: numerical and experimental investigations," *International Journal of Fatigue,* vol. 33, pp. 1360-1368, 2011.